REPORT DOCUMENTATION PAGE

AFRL-SR-BL-TR-01-

0454

Public reporting burden for this collection of information is estimated to average 1 hour per response, including the time for reviewing instru
needed, and completing and reviewing this collection of information. Send comments regarding this burden estimate or any other aspect o
burden to Washington Headquarters Services, Directorate for Information Operations and Reports, 1215 Jefferson Davis Highway, Suite 1
Budget, Paperwork Reduction Project (0704-0188), Washington, DC 20503

1. AGENCY USE ONLY (Leave blank)	2. REPORT DATE	3. REPORT TYPE AN
	25 Jul 01	Final Technical Report, 01 Jun 97–31 Dec 00

4. TITLE AND SUBTITLE
(AASERT97) DEVELOPMENT OF A FIELD EMITTER CATHODE FOR LOW-POWER HALL THRUSTERS

5. FUNDING NUMBERS
F49620-97-1-0380

6. AUTHOR(S)
A. D. Gallimore, C. M. Marrese

7. PERFORMING ORGANIZATION NAME(S) AND ADDRESS(ES)
University of Michigan Attn:
Kathryn DeWitt
DRDA, 3003 South State St.
Wolverine Towers, Room 1053
Ann Arbor, MI 48109-1274

8. PERFORMING ORGANIZATION REPORT NUMBER

20010905 076

9. SPONSORING / MONITORING AGENCY NAME(S) AND ADDRESS(ES)
AFOSR/NA
801 North Randolph Road,
Room 732
Arlington VA 22203-1977

11. SUPPLEMENTARY NOTES

12a. DISTRIBUTION / AVAILABILITY STATEMENT
Approved for Public Release; Distribution Unlimited

12b. DISTRIBUTION CODE

AIR FORCE OFFICE OF SCIENTIFIC RESEARCH (AFOSR)
NOTICE OF TRANSMITTAL TO DTIC. THIS TECHNICAL REPORT
HAS BEEN REVIEWED AND IS APPROVED FOR PUBLIC RELEASE
LAW AFR 190-12. DISTRIBUTION IS UNLIMITED.

13. ABSTRACT *(Maximum 200 Words)*

Fuel-efficient electric propulsion (EP) systems such as the Closed-Drift Hall thruster (CDT) can greatly enhance the capability of small satellites by reducing spacecraft propellant mass while increasing sensor payload and ΔV. However, a major stumbling block to the development of low-power ($\leq$100 W) CDTs is the absence of a suitable cathode. Conventional 6.4-mm hollow cathodes consume 20 W of power and 5 sccm of propellant, which is more than the total propellant flow rate of a 100-W CDT. Smaller hollow cathodes (e.g., 3.2-mm) are in development with the challenging goal of consuming 5 W of power. However, the minimum propellant flow rate of these cathodes is unlikely to dip much below 1 sccm. Our approach for providing electron emission for low-power CDTs is to use field emitter array cathodes (FEACs) as a replacement for hollow cathodes. AASERT funds were secured to support one student in a three-year program to investigate the use of FEAC technology with CDTs. The current-voltage characteristics and lifetime of several baseline cathode designs were evaluated over a wide range of pressures (10^{-10} to 10^{-6} Torr range in an ultra high vacuum FEAC test facility. FEAC performance models were also developed and compared with experimental results.

14. SUBJECT TERMS
Hall thruster; (Electric) Propulsion; Plasma physics; Field Emission

15. NUMBER OF PAGES
162

16. PRICE CODE

17. SECURITY CLASSIFICATION OF REPORT	18. SECURITY CLASSIFICATION OF THIS PAGE	19. SECURITY CLASSIFICATION OF ABSTRACT	20. LIMITATION OF ABSTRACT
UNCLASSIFIED	UNCLASSIFIED	UNCLASSIFIED	NONE

FINAL TECHNICAL REPORT

For research supported by
AFOSR Contract No. F49620-97-1-0380
for period 01 Jun 1997 to 31 Dec 2000

DEVELOPMENT OF A FIELD EMITTER CATHODE FOR LOW-POWER HALL THRUSTERS

Prepared by

Alec D. Gallimore[1] and Colleen M. Marrese[2]

Department of Aerospace Engineering
University of Michigan
Ann Arbor, MI 48109

Work Supported by

Air Force Office of Scientific Research
Program Monitor: Dr. Mitat Birkan

[1] Associate Professor, Principal Investigator, Department of Aerospace Engineering
[2] Graduate Student Research Assistant, Currently, Research Scientist at the Jet Propulsion Laboratory, Pasadena, CA

APPROVED FOR PUBLIC RELEASE; DISTRIBUTION UNLIMITED

July 2001

© Colleen Marie Marrese 1999
All Rights Reserved

To my mom and dad

ACKNOWLEDGMENTS

This thesis would not be a reality without contributions from an incredible number of people. I apologize for not individually recognizing all of them. I truly appreciate all of the advice and support that I have received from my peers, advisors, and collaborators. I am very grateful for their generosity with their time, expertise, and patience. First, I would like to individually thank my advisor, Professor Gallimore. He has cultivated a laboratory environment with talented students and fantastic facilities that is both a motivational and exciting place to work. He encouraged me and supported opportunities to grow, improve, and learn from the experts wherever they were. His advice and support were essential components of my success. I would also like to thank the talented students working at PEPL with whom I have collaborated on various projects, Matt Domonkos, James Haas, Dr. Brad King, Dr. John Foster, Frank Gulzinski, George Williams, Sang Wook Kim, Dr. Shawn Ohler, and Dr. Sven Bilen, Shane Malone. Matt and James made extraordinarily long hours in the lab or office tolerable, and their friendship made me a much happier and healthier person during the graduate years. I would also like to thank many other people in the Aerospace Dept. including Tom Griffin, Terry Larrow, Dave McLean, and Gary Gould for their technical support and Margaret Fillion, Caroline Rehberg, Bonnie Willey, and Debbie Laird for administrative support.

I also had the privilege of working with many people outside of the University of Michigan. I would like to thank the great people at JPL who advised me, supplied me with equipment and facilities, imaged the parts I destroyed, and made me new ones. I truly enjoyed every summer, spring, fall, and especially winter I worked there. Dr. Polk

has been a fantastic mentor whose enthusiasm has fueled mine. I am also indebted to Dr. Keith Goodfellow, Dr. Joe Wang, John Blandino, Dr. John Brophy, Dr. John Anderson, Dr. Stephanie Leifer, Dr. Juergen Mueller, Muriel Nocca, Oliver Duchemin, Bill Thogmartin, Al Owens, Bob Toomath, Chuck Garner, Russell Lawton, Jim Okuno, Bob, Indrani Chakraborty, Dr. Don Strayer, Dr. Elizabeth Kolowa, Dr. Pierre Giaque, and Dr. Peter Mueller. I am very grateful for the opportunity to work with Drs. Bill Mackie and Tianbao Xie at the Linfield Research Institute. I truly enjoyed the experiences I had in their laboratory studying field emission from carbide cathodes, and appreciate their help, advice, and patience during the process. I would like to thank other people in the field emission cathode community who introduced me to field emission cathode technology, provided me with cathodes, and advised me while I was testing them: Capp Spindt, Dr. Kevin Jensen, and Dr. Richard Fink. I would especially like to thank Dr. Sergei Khartov and Dr. Sasha Korolyov at the Moscow Aviation Institute for introducing me to electric propulsion and having an extraordinary amount of patience while teaching me plasma physics and electric propulsion in Russian. My thesis work is a result of their initial direction and guidance.

I would also like to thank my committee members, Prof. Gallimore, Prof. Washabaugh, Prof. Gilchrist, Dr. Polk, and Dr. Jensen for their support, help, and advice while documenting and completing my thesis work; any errors which remain are my own. Dr. Jensen's help in acquiring cathodes and modeling their performance was greatly appreciated.

I would also like to gratefully acknowledge the sponsors of this research and my graduate education, BMDO (contract monitored by Dr. James Polk at JPL), AFOSR (Dr. Mitat Birkan), JPL (Dr. James Polk), and ZONTA. Initial funding for my graduate studies came from Dr. Len Caveny (formerly at BMDO). I am truly grateful for his support. I would also like to thank Misison Research Inc. for free access to MAGIC.

Most importantly, I thank my family for their love, support, encouragement, prayers, and inspiration, every step of the way. I also thank my best friend Chris for his support and for giving me the incentive to finish this thesis now.

I hope that everyone who has this same opportunity to pursue a Ph.D. truly realizes how incredibly lucky we all are.

C. M. M

June 9, 1999

PREFACE

This thesis represents the first investigation into the compatibility of Field Emission (FE) cathodes and Electric Propulsion (EP) systems. FE cathodes have demonstrated 1000s of hours of operation in Ultra High Vacuum (UHV) environments. Hall thrusters have demonstrated 1000s of hours of operation in 10^{-6}-10^{-5} Torr with hollow cathodes. FE cathodes are being considered to replace hollow cathodes in Hall and ion thrusters because they do not require propellant, operate cold, and operate at much lower power levels. These features are especially important as EP systems are shrinking in size and power levels to meso- and microscales. The effects of hostile thruster environments on the performance of FE cathodes was investigated in this thesis work. Issues of contamination, lifetime, and space-charge limited electron emission were addressed. Experiments were performed to determine if silicon and molybdenum Field Emission Array (FEA) cathodes could operate in xenon environments without performance degradation, what caused the performance degradation, and how the degradation rate could be controlled. Models were developed to predict performance degradation rates of Si and Mo FEA cathodes in xenon environments. They were used to determine cathode lifetimes and suggest cathode configurations that will satisfy lifetime and current requirements. A sheath model was also developed to predict space-charge current limits in operating configurations where a plasma provides a virtual anode to collect the emitted current. This model was also used to investigate the space-charge limits on FE cathodes in Low Earth Orbit (LEO) on a tether system. The sheath and performance models were used to optimize cathode configurations for thruster and tether applications.

TABLE OF CONTENTS

ACKNOWLEDGMENTS IV

PREFACE VII

LIST OF FIGURES XI

LIST OF TABLES XVI

LIST OF APPENDICES XVIII

CHAPTERS 1

1 INTRODUCTION 1

1.1 Electric Propulsion 1
1.1.1 Role of Electric Propulsion 1
1.1.2 Hall Thrusters 3
1.1.3 Ion Thrusters 5
1.1.4 Oxygen Thrusters 6
1.1.5 Meso- and Microscale Thrusters 7
1.1.6 Conventional Electric Propulsion Cathode Technology 8
1.1.7 Advanced Cathode Requirements 9
1.2 Space Tethers 9
1.2.1 Electrodynamic Tethers 10
1.1.2 Cathode Requirements 10
1.3 Field Emission(FE) Cathodes 11
1.1.1 Field Electron Emission 12
1.1.2 State-of-the-Art FE Cathode Technology 13
1.4 Challenges 15
1.4.1 Cathode Lifetime 15
1.1.2 Space-Charge Limited Emission 18
1.5 Role of this Thesis 21

2 CATHODE ENVIRONMENT CHARACTERIZATION 25

2.1 Experimental Apparatus 25
2.1.1 Test Facility 25
2.1.2 Hall Thruster-PEPL-70 27
2.1.3 Diagnostics 28

2.2 Experimental Methods and Results 29
2.2.1 Thruster Performance 29
2.2.2 Xenon Pressure and Ion Current Density in Cathode Region 32

3 FIELD EMISSION CATHODE EXPERIMENTS 34

3.1 Carbide Single Tip Cathode Experiments 35
3.1.1 Cathodes 35
3.1.2 Experimental Apparatus 36
3.1.3 Experimental Methods and Results 37
3.2 Mo and Si Field Emission Array Cathode Experiments 42
3.2.1 Cathodes 43
3.2.2 Experimental Apparatus 46
3.2.3 Si FEA Cathode Experimental Methods and Results 48
3.2.4 Mo FEA Cathode Experimental Methods and Results 53
3.3 Carbon Film FE Cathode Experiments 59
3.3.1 Carbon Film FE Cathode 60
3.3.2 Experimental Apparatus 61
3.3.3 Experimental Methods and Results 62

4 MICROTIP CATHODE PERFORMANCE MODELING 67

4.1 FEA Cathode Performance Degradation Model 67
4.1.1 Field Electron Emission Model 68
4.1.2 Tip Sputtering Model 72
4.1.3 Sputter Yield Model 76
4.2 Modeling Results 80
4.2.1 Mo SRI International Cathode 81
4.2.2 Si MCNC FE Cathodes 87
4.3 Application of Modeling and Experimental Results 90

5 SPACE-CHARGE LIMITED ELECTRON EMISSION FROM FIELD EMISSION CATHODES INTO A PLASMA 96

5.1 Sheath Model 99
5.1.1 Planar Sheath Geometry 99
5.1.2 Cylindrical Geometry 104
5.1.3 Spherical Geometry 107
5.2 Modeling Results 108

6 CONCLUSIONS 122

6.1 Summary of Major Results 122
6.2 Recommended Cathode Designs 126

6.3 Recommendations for Future Research 128
6.4 Other Applications 129

APPENDICES **131**

APPENDIX A **132**

APPENDIX B **137**

APPENDIX C **141**

APPENDIX D **149**

BIBLIOGRAPHY **155**

LIST OF FIGURES

Figure 1.1 Cross-section of a Hall thruster with a hollow cathode. 5

Figure 1.2 Cross-section of an ion thruster (courtesy of Matt Domonkos). 6

Figure 1.3 A Hall thruster shown with hollow and field emission cathodes. 11

Figure 1.4 Potential energy diagram for electrons at a metal surface, without (left) and with (right) an applied electric field, F. 12

Figure 1.5 Field emission tip and gate electrode configuration (courtesy of Dr. Kevin Jensen). 13

Figure 1.6 Potential diagram of the cathode, thruster, and plasma configuration. Anode, plasma ion beam, sheath boundary, gate electrode, and cathode potentials are shown relative to ground. 19

Figure 1.7 Flow diagram for the field emission array cathode performance degradation model. 23

Figure 2.1 Thrust stand calibration data. 27

Figure 2.2 The PEPL-70 Hall thruster with a hollow cathode, neutral particle flux (NPF) probe, and Faraday Probe. 28

Figure 2.3 Faraday probe schematic (courtesy of James Haas). 29

Figure 2.4 I-V curves from the PEPL-70 at different xenon volumetric flow rates. 31

Figure 2.5 Thruster performance data with varying propellant flow rate and a constant discharge voltage, 300V. The numbers on the markers on the graph correspond to the total propellant flow rate (sccm). The table above the graph shows the discharge current also. 31

Figure 3.1 A scanning electron microscope (SEM) micrograph of a single carbide cathode in a Vogel-type mount. 36

Figure 3.2 An illustration of how the field emission microscope (FEM) was used to determine the emitting area of the tip from the angle, σ, which can be calculated from the size of the emission pattern, d, on the screen at a distance x from the emitter. 37

Figure 3.3 Electrical schematic of the FEM. 37

Figure 3.4 Emission patterns observed with the FEM from fairly clean carbide cathodes. 39

Figure 3.5 Emission patterns observed with the FEM from damaged or contaminated carbide. 39

Figure 3.6 Evolution of the tip emission pattern observed with the FEM a,b) during and c) after the exposure to argon. 41

Figure 3.7 Fowler-Nordheim (F-N) (left) and I-V curves (right) obtained from the ZrC cathode before and after exposure to argon. 42

Figure 3.8 A MCNC Si field emission array single tip configuration (courtesy of MCNC). 44

Figure 3.9 A SRI International Mo field emission array cathode single tip and array. ... 45

Figure 3.10 The ultra-high vacuum (UHV) facility at the Jet Propulsion Laboratory..... 47

Figure 3.11 The field emission cathode test flange in UHV facility. 47

Figure 3.12 Electrical schematic for field emission cathode testing..... 48

Figure 3.13 I-V curves taken before and after the Si cathode was exposed to Xe. 49

Figure 3.14 Si cathode current response to an increase in Xe pressure with V_g at 86 V and V_a at 400 V. 50

Figure 3.15 Si cathode current response to $2x10^{-5}$ Torr of Xe with V_g at 70 V and the V_a at 70 V. 51

Figure 3.16 MCNC Si cathode current response to a 1 hour Xe exposure with V_g at 50 V and V_a at 70 V. 52

Figure 3.17 I-V data taken before and after the Mo cathode was exposed to xenon. 53

Figure 3.18 Mo cathode current response to $2x10^{-6}$ Torr of xenon with V_g at 65.6 V and V_a at 80 V. 54

Figure 3.19 The Mo cathode current response to increasing gate electrode voltage with V_a at 100 V, $2x10^{-5}$ Torr of Xe. 55

Figure 3.20 A comparison of the Mo cathode current response to increasing gate electrode voltage in $2x10^{-9}$ Torr and $2x10^{-5}$ Torr of Xe. 56

Figure 3.21 Mo cathode current response to a Xe pressure increase up to $2x10^{-5}$ Torr of xenon for 5 hours with V_g at 50 V and V_a at 60 V. 57

Figure 3.22 Mo cathode current response to a Xe pressure increase up to $2x10^{-5}$ Torr with varying V_a and V_g at 50 V. 57

Figure 3.23 Mo cathode current response to a Xe pressure increase up to $2x10^{-5}$ Torr for 2 hours with V_g at 50 V and V_a at 100 V. 58

Figure 3.24 A FEPET carbon film cathode on a glass stem. 61

Figure 3.25 I-V traces showing the performance of a FEPET carbon film cathode in a UHV environment. 62

Figure 3.26 The cathode current response to increasing the Xe pressure up to $2x10^{-6}$ Torr for 4 hours. The anode potential was 900 V above the potential of the carbon film. 64

Figure 3.27 I-V curves taken in UHV before and after the carbon film cathode was exposed to xenon. 64

Figure 3.28 Carbon film cathode turn-on and turn-off I-V curves with an anode voltage of 900 V in $2x10^{-6}$ Torr of xenon compared to turn-on I-V data in UHV. 65

Figure 4.1 The actual cathode configuration, and the configuration used in the microtip sputtering model to predict the potential field near the microtip and electric field at the microtip. 74

Figure 4.2 Significant radial positions used in the model of microtip sputtering..... 75

Figure 4.3 Xe ionization cross-sections, Q_i, from Brown.[74] 76

Figure 4.4 Sputter yields for a Mo target being bombarded by Xe ions. Shown on the graph are theoretical curves for two values of E_{th}, and experimental values measured by Rosenberg and Wehner. 79

Figure 4.5 Sputter yields for a Si target being bombarded by Xe ions. Shown on the graph are theoretical curves for three values of E_{th}, and experimental values measured by Rosenberg and Wehner. 80

Figure 4.6 Experimental and theoretical Mo cathode current response to a Xe pressure increase up to $2x10^{-6}$ Torr with V_g at 65.6 V and V_a at 80 V with E_{th} of 39 eV..... 82

Figure 4.7 Mo cathode I-V data measured experimentally before the Xe exposure and predicted by Jensen's performance model. 83

Figure 4.8 Performance decay rate predicted by the performance degradation model for a Mo cathode operating in a Xe environment with a pressure of $2x10^{-5}$ Torr for a cathode with parameters (I) shown in Table 4.3. 85

Figure 4.9 Field emission array cathode performance decay predicted by the performance degradation model for a Mo cathode operating in $2x10^{-5}$ Torr of Xe for 100 hours at various gate electrode voltages with initial cathode parameters (I) shown in Table 4.3. 86

Figure 4.10 Measured and predicted Si cathode current response to an increase in Xe pressure up to $2x10^{-5}$ Torr with V_g and V_a at 70 V. 88

Figure 4.11 Measured and calculated Si cathode performance degradation as the Xe pressure increases up to $7x10^{-6}$ Torr with V_g at 86 V and V_a at 400 V..... 89

Figure 5.1 Cathode sheath configuration which was modeled. The boundary between the sheath and pre-sheath is shown at r_{sh}. 97

Figure 5.2 A planar cathode sheath scenario (left) with $r_c > r_{sh}$ and a spherical cathode sheath scenario (right) with $r_c < r_{sh}$. 98

Figure 5.3 Results of the cathode sheath model compared to the Prewett and Allen sheath model results. 104

Figure 5.4 The effect of V_g on J_{eemax} for the planar sheath geometry. The numeric markers represent the value of η_o for each solution. 111

Figure 5.5 The effect of ϕ_c on J_{eemax} for the planar sheath geometry. The numeric markers represent the value of η_o for each solution. 111

Figure 5.6 a, b Potential (a) and electric field (b) profiles for different emission currents in the cathode sheath 112

Figure 5.7 Charge density profiles in a planar cathode sheath with η_c=4 and η_g=6. 113

Figure B.1 Cathode Lens and Ion Repeller (CLAIR) configuration 138

Figure B.2 Equipotentials predicted by MAGIC for the CLAIR configuration described in Figure B.1 and Table B.1 139

Figure B.3 Electron trajectories predicted by MAGIC for the CLAIR configuration described in Figure B.1 and Table B.1 139

LIST OF TABLES

Table 2.1 Ion current densities measured by the Faraday probe flush with the exit plane of the thruster. Discharge voltage and current, electromagnet inner, I_{MI}, and outer, I_{MO}, currents, and Xe pressures are also given. 32

Table 2.2 Neutral Xe particle pressures and ion current densities measured by the probes 3 mm behind the physical exit plane of the thruster 32

Table 4.1 Ion and target material parameters used in the sputter yield model. 78

Table 4.2 Cathode parameters before (I) and after (II) Xe exposure obtained from I-V data and predicted (III) by the performance degradation model. 83

Table 4.3 Cathode parameters before (I) and after (II) xenon exposure which are used in the performance decay model for V_a at 100 V in $2x10^{-5}$ Torr of xenon. 85

Table 4.4 MCNC Si cathode parameters before the exposure to xenon during operation. 90

Table 4.5 SRI International #52M Mo cathode parameters (in bold) and predicted performance using different parameters, with and without a CEX ion bombardment during 100 hours 93

Table 4.6 Performance limitations of Si and HfC cathodes with and without a charge-exchange (CEX) ion population. 94

Table 5.1 Characteristics of the thruster and tether plasma environments investigated using the cathode sheath model 99

Table 5.2 Space-charge limited currents estimated by the planar sheath model for thruster and tether environments. 109

Table 5.3 Space-charge limited currents predicted by the planar, cylindrical, and spherical sheath models in normalized units. 114

Table 5.4 Field emission current limitations predicted by the sheath model in dimensional parameters for planar, cylindrical, and spherical geometries for the Hall thruster environment with an external cathode. V_g is at 30 V and V_c is at 20 V. .. 115

Table 5.5 Field emission current limitations predicted by the sheath model in normalized parameters for a spherical sheath in a tether environment where T_e is 0.1 eV. 116

Table 5.6 Field emission current limitations predicted by the spherical sheath model for the tether environment. 116

Table 5.7 Current limitations and virtual cathode potentials predicted by the Wang simulation model for a field emission cathode in a Hall thruster environment with $r_c = 4\ \lambda_D$, V_g at 30 V, ϕ_c at –20 V, T_e at 5 eV, and n_{eo} at $8 \times 10^8/cm^3$. 119

Table 5.8 Current limitations and virtual cathode potentials predicted by the Wang simulation model for a field emission cathode operating in a tether environment with $r_c = \lambda_D$, V_g at 30 V, ϕ_c at –20 V, T_e at 0.1 eV, and n_{eo} at $5 \times 10^5/cm^3$. 120

Table 6.1 Recommended number of cathodes, operating voltage, cathode material, and emitting area required in different applications if packing density is $10^8/cm^2$, $\Delta s = 2$, $r_g = 1000$, and $r_t = 40$. 127

Table 6.2 Recommended number of cathodes, operating voltage, cathode material, and emitting area required in different applications if packing density is $10^8/cm^2$, $\Delta s = 2$, $r_g = 1000$, $r_t = 40$, and CLAIR is used. 127

Table B.1 Electrode potentials, thicknesses, and spacing for the CLAIR configurgation simulated by MAGIC..... 138

LIST OF APPENDICES

Appendix

A. Nonemclature 132

B. Cathode Lens and Ion Repeller (CLAIR) 137

C. Fea Cathode Performance Degradation Model Macro 141

D. Cathode Sheath Model Macro 149

INTRODUCTION

The compatibility of Field Emission (FE) cathodes in Electric Propulsion (EP) systems is explored in this dissertation. Some of the results of this thesis work were also used to address compatibility issues between electrodynamic space tethers and FE cathodes. The plasma environments of these systems place challenging demands on cathode performance. Field emission cathode performance in simulated environments of interest is theoretically and experimentally evaluated. This chapter provides an introduction to the configurations, operation, and applications of Hall and ion thrusters, electrodynamic tethers and FE cathodes. The motivation for using FE cathodes with thrusters and tethers and the associated challenges are presented. Previously obtained experimental results which motivated the experimental performance evaluations employed in this thesis work is discussed.

1.1 Electric Propulsion

EP systems have been under investigation since the 1950s as alternatives to chemical propulsion systems on spacecraft. They offer advantages including higher specific impulse, and, therefore, lower wet system mass for the same mission, resulting in significantly reduced launch costs. EP systems fall into three categories: electrothermal, electrostatic, and electromagnetic. These systems have been optimized for different thrust, specific impulse, and power regimes.

1.1.1 Role of Electric Propulsion

The primary advantage of EP systems over chemical propulsion systems is their higher effective exhaust velocity, u_e. The amount of propellant required by the rocket

engine to impart the necessary change in velocity, ΔV, to a payload is determined by the rocket equation,

$$\frac{M_i}{M_f} = \exp\left(\frac{\Delta V}{u_e}\right).$$

M_i is the initial mass of the spacecraft including fuel, and M_f is the final mass of the spacecraft after the fuel has been spent. The amount of fuel required to attain the desired ΔV exponentially increases with ΔV. Chemical rockets are limited to u_e below ~5000 m/s. Particle exhaust velocities can be an order of magnitude higher in EP systems than in chemical systems because electrical energy is added to the system to heat or ionize and accelerate the propellant instead of relying on chemical energy of the propellant. The rocket equation shows how much less propellant is needed for the same mission ΔV when u_e is significantly increased with the use of electric propulsion.

EP systems have been used for North-South Station-Keeping (NSSK) on satellites and primary propulsion for interplanetary probes. They could also be used for orbit raising, comet sample return, and piloted missions to Mars. Interplanetary probes require significant periods of continuous thrusting during a mission while satellites require short duration thrusting periodically during the satellite lifetime. Lifetimes in excess of 1000s of hours are required of EP systems for satellites or interplanetary probes, and piloted spacecraft. Power is supplied to EP systems with solar (<100 kW) or nuclear sources, depending on the amount of power required.

There are several types of EP systems, each with unique capabilities and roles. Currently, the most widely used and simplest EP system is the resistojet, an electrothermal device. It is used on communication satellites for NSSK, attitude control, on-orbit maneuvering, and is capable of running on waste water. The MR501 hydrazine resistojet operates at 350-500 W to generate 0.18-0.36 N of thrust at 280-300 s.[1] The electrothermal arcjet is also commonly used on communication satellites, operating at 1.8 kW using hydrazine propellant. Spacecraft equipped with megawatts of power could

employ magnetoplasmadynamic (MPD) thrusters, electromagnetic devices, for sample return missions and piloted missions to Mars. This system can operate at 60% efficiency on lithium propellant. Field Emission Electric Propulsion Systems (FEEP) are being considered for drag compensation for precise spacecraft positioning.[2] These systems operate at 10 kV, ~1 mA, with maximum thrust approximately 1 mN. FEEPs have been built to operated at only 30 μN. Hall thrusters have been used on communication satellites that employ solar power. These 1.35 kW systems have been optimized to operate at ~53% efficiency on xenon to generate ~83 mN of thrust at 1600 s specific impulse.[3] Ion thrusters have been used on communications satellites and interplanetary probes. A 30 cm ion thruster is currently being used for primary propulsion on DS-1, a mission to fly-by an asteroid and comet. A 30 cm ion thruster can generate 91 mN of thrust at a specific impulse of 3380s and 66% efficiency with xenon propellant.[4] Hall and ion thrusters are both electrostatic propulsion systems. Constellations of hundreds of satellites for global telecommunication systems, are being developed which will employ these systems.

1.1.2 Hall Thrusters

Development of the Hall thruster was initiated independently in both the USSR and the U.S. in the early 1960s. Research efforts in the U.S. were more heavily focused on the ion thruster by 1970, while development of the Hall thruster flourished in the former USSR.[5] Following the first flight of a Hall thruster, the SPT-60, in Feb. 1972 on the Meteor satellite, approximately 100 Hall thrusters have been used on Russian satellites. Engineers in the U.S. have been working on integrating Russian Hall thrusters and U.S. satellites since 1992. Thrusters developed for 11kW communication satellites operate at 1.35 kW to generate 83 mN of thrust and 1600 s specific impulse. Recent discussions about deploying constellations of ~300 satellites have included scenarios with

5-6 kW of on-board power that could support 4.5 kW propulsion systems with 2-6 systems on-board. Since 1993, there has been a flurry of research activity in the U.S. focusing on characterizing their performance, modeling their performance, and understanding the issues associated with integrating Hall thruster and satellite systems. High energy ions emitted by the propulsion systems can damage a spacecraft and plasma noise can interfere with communication systems. Hall thruster design development has been on-going for more than 20 years to improve performance and minimize interference with communication systems and damage to spacecraft surfaces. These thrusters operate most efficiently on xenon, however, they have also used Ar, Kr, Air, O_2, N_2, Bi, and Cs propellants.

A Hall thruster developed at PEPL is shown in Figure 1.1. The PEPL-70, based on Russian designs, was developed as a laboratory model and used only to generate a plasma environment to characterize. Hall thrusters employ an anode as the positive electrode and gas distributor in the annular ceramic discharge chamber. Multiple chambers are typically used in the anode to improve the azimuthal uniformity of the propellant injection. The discharge chambers are usually composites of BN, Si, and AlO2. Hall thrusters employ inner and outer electromagnets with poles at the thruster exit plane to support a radial magnetic field (~300 Gauss in the center of the discharge chamber) with large gradients. The cathode is commonly positioned external to the thruster. When the discharge voltage is applied, the anode and cathode support an axial electric field. The cathode emits electrons to ionize the propellant and to neutralize the ion beam emitted from the thruster. These thrusters require 0.2-10 A of current, depending on the size of the thruster. Electrons emitted by the cathode become trapped in the crossing electric and magnetic fields in a closed azimuthal drift. Xenon atoms are injected into the drifting electron cloud from the anode, and are then ionized by electron bombardment. The axial electric field accelerates ions axially out of the discharge chamber to produce thrust. In the Hall thruster, the ionization and acceleration occur in

the same region; therefore plasma quasineutrality is maintained everywhere in the thruster.

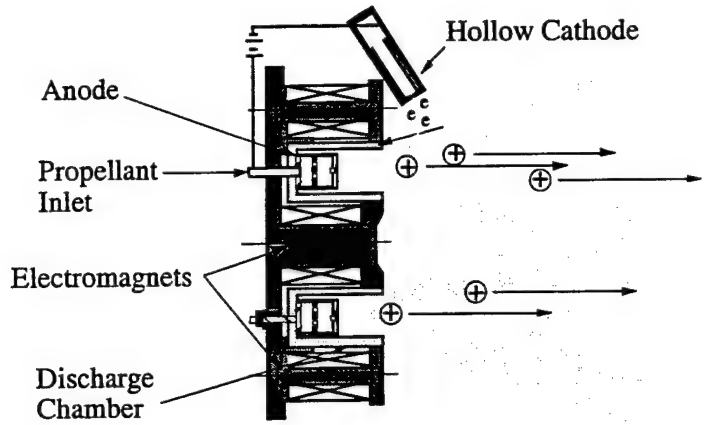

Figure 1.1 Cross-section of a Hall thruster with a hollow cathode.

1.1.3 Ion Thrusters

An ion thruster is another form of an electrostatic EP system with performance similar to Hall thrusters. They typically operate at a higher specific impulse and higher efficiency than do Hall thrusters. This thruster also ionizes the propellant by electron bombardment. It employs permanent bar magnets which run along the discharge chamber, as shown in Figure 1.2. The electrons become trapped in the magnetic field between the cathode and anode. This thruster has separate regions for ionization and acceleration. The thruster configuration is shown in Figure 1.2. This thruster requires a cathode inside of the discharge chamber for propellant ionization and another cathode outside of the thruster for ion beam neutralization. The propellant is ionized in the discharge chamber and then extracted by the screen grid. Ion beam acceleration occurs between the acceleration and screen grids. Ion thrusters operate at lower current densities than Hall thrusters because space-charge effects between the grids limit the ion current

density; however, an ion thruster can accelerate ions through much higher voltages than the single stage Hall thruster discussed in this thesis. A typical 30 cm ion engine is capable of generating 92 mN of thrust at 62% efficiency with a specific impulse of 3100 s. Specific impulses above 10,000 s have been achieved by ion thrusters.

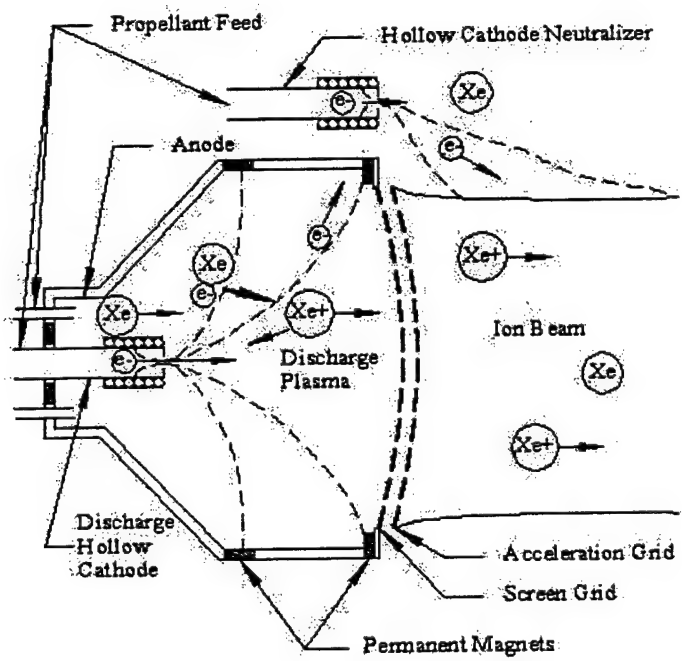

Figure 1.2 Cross-section of an ion thruster (courtesy of Matt Domonkos).

1.1.4 Oxygen Thrusters

Hall thrusters that use oxygen as the propellant are being developed for missions in which *in-situ* resource utilization is a necessity. Lunar surface material is 50 % oxygen by weight,[6] and 95 % of the Martian atmosphere is CO_2. If oxygen is extracted from these environments, it can be used as propellant for lunar cargo vehicles or Mars sample return missions when necessary. Acquiring propellant at the mission target for the return trip could significantly reduce the launch costs of a mission. In the future, if

and when these missions occur regularly, using this propulsion system could prove to be rewarding.

Before oxygen Hall thrusters can be utilized, their efficiency must be improved[7] and the hollow cathodes typically used with Hall thrusters must be replaced with cold cathodes. Hollow cathodes employ thermionic electron emitters, which are very sensitive to the operating environment. In an oxygen environment, these electron emitting cathode inserts quickly oxidize and their work function increases. To overcome the increase in work function and maintain a constant current, higher power levels are required for the heaters to attain higher operating temperatures for the insert. At high enough temperatures surface oxidation rates significantly decrease; however, the lifetime of the emitters will also significantly decrease. If Hall thrusters are to successfully operate on oxygen propellant, cold cathodes must replace hollow cathodes in these systems.

1.1.5 Meso- and Microscale Thrusters

Meso0 and microscale thrusters are being developed for spacecraft in the 1-200 kg wet mass range and for fine attitude control of larger spacecraft. The interest in such small spacecraft is motivated by the reduction of launch costs and mission risk. It has been proposed that particular missions, like exploring the rings of Saturn, be accomplished by fleets of microcraft possibly in communication with a larger mother spacecraft.[8] Such spacecraft configurations provide a high degree of mission flexibility.[9] Larger spacecraft could use microscale electric propulsion systems for continuous disturbance torque compensation and drag make-up. Such missions include laser interferometer space antenna (LISA)[10] for the detection of gravitational waves, Gravity Recovery and Climate Experiment (GRACE) follow-on mission, and Terrestrial Planet Finder. Incredibly precise position maintenance is required for both of these missions. Microscale propulsion systems are a necessity for the success of this type of mission.

While microscale propulsion system technology is still very immature, a mesoscale 50 W Hall thruster has been developed.[11] The primary technological hurtle for this propulsion system is now finding a compatible cathode. The cathodes commonly used with larger scale Hall thrusters are not presently compatible with this thruster. A 1/4" cathode operates at 25 W, and a 1/8" hollow cathode operates at 7-10 W. These cathodes consume power that can be as high as 50 % of the total power of a mesoscale system. Some mesoscale thrusters at 50 W will require ~1.5 sccm of propellant, and an 1/8" cathode will require 0.5-1.0 sccm. Therefore, hollow cathodes can also consume 50% of the propulsion system propellant. This problem will be even more severe with microscale propulsion systems requiring an electron source.

1.1.6 Conventional Electric Propulsion Cathode Technology

Cathodes conventionally used with Hall and ion thrusters are too inefficient to be used with meso- and microscale propulsion systems and are easily contaminated in oxygen environments. Hollow and filament cathodes are most commonly used with Hall and ion thrusters. Hollow cathodes employ lanthanum hexaboride, LaB_6, or barium oxide, BaO_2, impregnated tungsten inserts which require heaters to increase their temperature up to ~1000 °C for sufficient electron emission before thruster start-up. They also require propellant to create plasma which 'contacts' the electron beam to the ion beam. Ions created in this plasma supply thermal energy to the insert by collisional energy transfer, and neutralize the negative space-charge of the electron beam. This local plasma increases the electron transmission from the cathode to the thruster discharge chamber and ion beam at voltages ~20 V. State-of-the-art 1/8" hollow cathodes under development at NASA Glenn Research Center (GRC) and the Plasmadynamics and Electric Propulsion Laboratory (PEPL) at the University of Michigan consume ~7 W and 0.1 mg/s of xenon for ~0.1 A.[12] Filament cathodes can also be used with Hall and ion

thrusters, and field emission electric propulsion systems (FEEP); however, they also consume significant power. An oxide thermionic cathode is being developed for FEEP systems at ESTEC with an anticipated performance of 5 mA/W.[13]

1.1.7 Advanced Cathode Requirements

The development of small, meso-, and microscale propulsion systems, and oxygen thrusters for spacecraft will be enabled by the development of cold cathodes, which do not require propellant. Such cathodes should be easily scalable in size to less than 1 cm^2 and power to less than 1 W/A to be used by small, meso-, and microscale thrusters. These cathodes must survive for 1000s of hours eventually; however, initial performance objectives are only 100 mA/cm^2, for 100 hr. in simulated thruster environments.

1.2 Space Tethers

Space tethers are conducting or non-conducting cables which are used to couple spacecraft together for energy transfer or for propulsive maneuvers. They typically consist of a center conducting wire surrounded by several layers of thin strands of high strength fibers. It has been proposed to use tethers for orbit transfer and for orbit insertion from the Earth's or Moon's surface using rotating tethers.[14,15] The action of tethers depends on orbital mechanics. A tether dropped down from a spacecraft is pulled down to the Earth while a tether extended up from the spacecraft in orbit is pulled up by centrifugal forces. Electrodynamic tethers use interactions between Earth's magnetic field and current in the tether for power or propulsion.[16] SEDS-2 mission demonstrated that a 20 km long tether could successfully de-orbited at payload from LEO. The TSS-1R mission demonstrated that tethers can be used to boost satellites into higher orbits. The

terminator tether is one type of electrodynamic tether that can be used to de-orbit satellites.

1.2.1 Electrodynamic Tethers

It has been proposed to use the electrodynamic (ED) space tethers to de-orbit satellites at the end-of-life.[17] One concept for using ED tethers to de-orbit spacecraft is the Terminator Tether™.[17] These ED tethers use passive electrodynamic tether drag to de-orbit a satellite from LEO. As the vertical tether is pulled through the mostly horizontal Earth magnetic field by the spacecraft, a voltage is induced in the tether wire. Wire ends make contact with the space plasma with one end emitting electrons. The current is conducted through the space plasma to the other end of the tether where electron collection occurs. The Earth's magnetic field induces a JxB force on the wire which opposes the host spacecraft motion. Electrodynamic drag is many orders of magnitude greater than aerodynamic drag for orbits above 500 km.[17] A 700 kg satellite at 1475 km could be de-orbited in 6 months by a 10-km-long tether.[17] The mass of the tether system is less than a third of the propellant mass required by a resistojet if the electron emitter on the tether system does not require a heater or consumable gas supply.[17]

1.2.2 Cathode Requirements

Electron emitters used with an ED tether de-orbiting system must operate cold and without propellant, and be capable of as much as 2 A to make it competitive with other satellite de-orbiting options. It is also important that cathode materials are resistant to oxidation in Low Earth Orbit (LEO). The cathode current requirement could be satisfied by using several cathodes. The tether system could use a single hollow cathode as the electron source, however, the mass penalty of this cathode system may negate the advantage of the ED over the resistojet to de-orbit satellites. The use of cold cathodes

that do not require a consumable gas could return the competitive edge to the ED tether concept.

1.3 Field Emission(FE) Cathodes

A FE cathode is a promising alternative to thermionic hollow cathodes because they are small, cold, efficient, chemically inert, and do not require an ionizable gas. Figure 1.3 shows a Hall thruster with FE cathodes in two possible positions: in the center of the thruster (internal) and on the periphery (external). FE cathodes employ strong electric fields instead of high temperatures to emit electrons. FE cathodes require much simpler and smaller systems to operate them than conventional cathodes. They can be easily scaled in size and power level to be compatible with microscale propulsion systems, and have demonstrated significantly higher efficiency than thermionic cathodes.[18] Two types of FE cathodes were investigated in this thesis: thin film carbon FE cathodes, and microcone field emission array (FEA) cathodes.

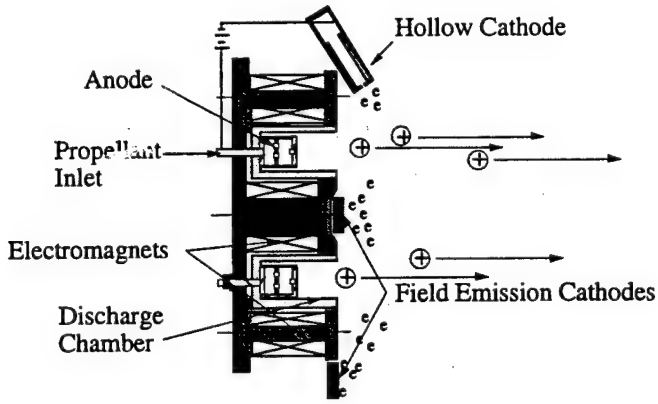

Figure 1.3 A Hall thruster shown with hollow and field emission cathodes.

1.3.1 Field Electron Emission

Field electron emission occurs when applied electric fields, F, at the cathode surface are high enough (0.3-0.6 V/Å) to deform the potential barrier, ϕ_w, between the cathode surface and vacuum to allow electrons to tunnel out of the cathode surface and through the deformed potential barrier.[19] Potential barrier deformation by an electric field is shown in Figure 1.4. The applied electric field is F, the work function is ϕ_w, the Fermi energy is E_F, and e is the electron charge. The Fermi energy is the maximum energy level occupied by electrons if all of the lower energy levels are filled in the quantum structure. The height of the potential barrier between the surface and vacuum is ϕ, and the width of the barrier is ϕ_w/F. The electrons emitted by field emission originate below the Fermi energy level, therefore these low energy electrons are considered cold. Field emission differs significantly from thermionic or photoemission where electrons in the solid must be given enough energy to go over the potential barrier. These electrons have energy considerably greater than the Fermi energy, and are considered hot.

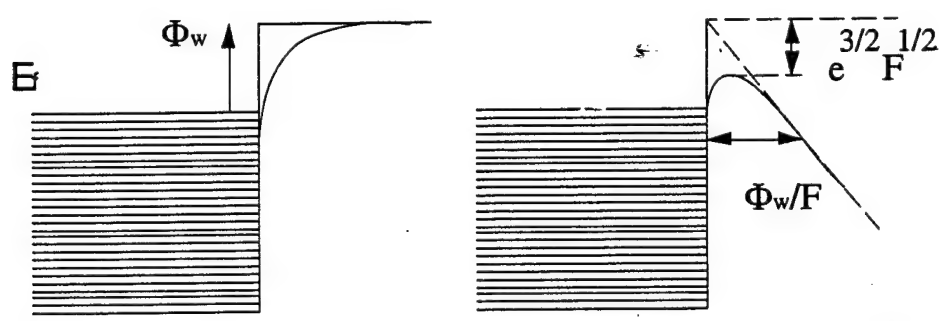

Figure 1.4 Potential energy diagram for electrons at a metal surface, without (left) and with (right) an applied electric field, F.

Spindt-type FEA cathodes with microtip structures require electric field enhancement by the sharp tip structure. Electric fields at the emitting tips in excess of 4×10^7 V/cm are required for field emission. The field emission tip configuration, which

is typically employed, is shown in Figure 1.5; dimensions and materials are processor dependent. The Fowler-Nordheim (F-N) equation for field emission current density at an emission site is Eqn. 1.1. The F-N coefficients are a_{fn} and b_{fn} are given in Eqn. 1.2 and Eqn. 1.3 where $t(y) \approx 1.05657$, $v_o \approx 0.93685$, m=511000 eV/c^2 , c=2998.79 Å/fs, $Q=\alpha \hbar c/4=3.6$eV-Å, $\alpha=1/137.04$, and $\hbar=0.655$eV-fs. A more detailed derivation of these relationships is given elsewhere.[20,21]

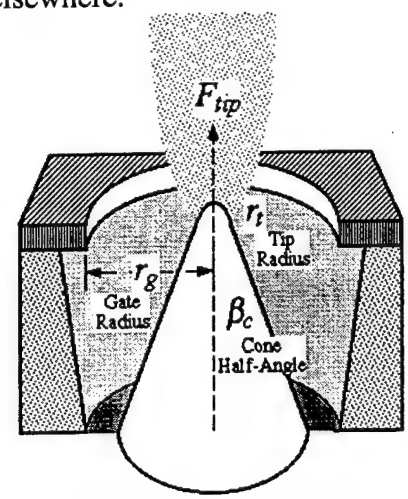

Figure 1.5 Field emission tip and gate electrode configuration (courtesy of Dr. Kevin Jensen).

Eqn. 1.1
$$J_{FN}(F) \approx a_{fn} F^2 \exp(-b_{fn}/F),$$

Eqn. 1.2
$$a_{fn} = \frac{1}{16\pi^2 \hbar t(y)^2 \Phi} \exp\left(\frac{16Q}{3\hbar}\sqrt{\frac{2m}{\Phi}}\right) \approx (116\phi)^{-1} \exp\left(\frac{14.3994 b_{fn}}{\phi^2}\right)$$

Eqn. 1.3
$$\text{and } b_{fn} = \frac{4}{3\hbar}\sqrt{2m\Phi^3}\, v_o \approx 0.642\phi^{3/2}.$$

1.3.2 State-of-the-Art FE Cathode Technology

The applications discussed in this thesis require state-of-the-art FE cathode technology for materials, cathode structure, and current limiting architectures. This technology is evolving as microfabrication techniques mature to deposit more robust

materials, and smaller and more complicated structures. Microfabrication techniques are applied to deposit and etch insulating and conducting films and arrays of microcones on silicon wafers. Electron beam and interferometric lithography techniques are used for patterning the cathodes. Tip and gate aperture radii are on the order of 1 and 100 nm, respectively.[22] Packing densities greater than 10^8 tips/cm^2 have been achieved.[23,24] Materials most commonly used are silicon and molybdenum, however, diamond-like carbon films and coatings on the microtips have been used to improve robustness of the tips, work functions, chemical inertness, and emission stability.[25,26,27,28] Molybdenum FEA cathodes fabricated at the Massachusetts Institute of Technology Lincoln Laboratory (MIT/LL) have attained 1 μA at 25 V with an array of 900 tips. The same cathodes with cesiated tips demonstrated 1 μA at 10 V.[24] Spindt at SRI International has reported dc field emission up to 100 μA/tip from a 100-tip array.[29] Emission current densities greater than 2000 A/cm^2 have been achieved.[30,31] The current collected by the gate electrodes is typically 1/1000 of the emitted current. For optimum cathode performance typical tip operating pressure is ~10^{-9} Torr after careful conditioning in hydrogen and neon environments.[32,33,34] Microtip FEA cathodes at SRI International have demonstrated performance of 100 mA with less than 1 mW consumed by the gate electrode.[35]

Alternatives to the micro-fabricated FEA cathodes are diamond, diamond-like carbon, or carbon thin film FE cathodes. The unique advantage to using doped carbon is its low electron affinity.[36] These cathodes can emit electrons at macroscopic vacuum electric field strengths that are two orders of magnitude lower than those fields required by silicon and molybdenum Spindt-type cathodes and performance is not as sensitive to sputtering by ion bombardment.[36,37,38] Diamond cathodes are very resistant to oxidation while some carbon films have demonstrated performance degradation in oxygen environments.[38]

Carbon FE cathodes are more robust than the Spindt-type FEA cathodes, however the Spindt-type cathodes have typically demonstrated higher current densities and

efficiency. Various types of carbon cathodes have been investigated. It is common for carbon film cathodes to operate with only 20% of the emitted current escaping through the gate electrode and being collected by the anode. A 40 mA current was measured at Field Emission Picture Element Technology (FEPET) Inc. from a 25 mm carbon film cathode with an extraction field of 6.7×10^4 V/cm.[37] An emission current density of 100 mA/cm^2 was achieved with an extraction field of less than 1.2×10^5 V/cm. Blyablin et al. demonstrated 500 mA/cm^2 from diamond film cathodes.[39] Cathodes with diamond grit in microfabricated gated structures have achieved 100 mA/cm^2 at 20 V.[36]

1.4 Challenges

State-of-the-art FE cathodes have demonstrated excellent performance in UHV environments with large anode voltages and promising results in some higher pressure environments. Thruster and tether environments could significantly limit the performance of these cathodes. FE cathodes have demonstrated lifetimes of 1000's of hours in UHV environments. In higher-pressure environments cathode lifetime can be shortened by arcing between the gate electrodes and tips, and by the cathode getting sputtered by ion bombardment. In low-pressure environments without a close-spaced anode, electron emission can be space-charge limited.

1.4.1 Cathode Lifetime

In UHV environments, the primary cathode failure mode has been arcing between the gate and tip, shorting out the cathode and ending its life. In higher pressure environments, this threat is even greater. Recent advances in microfabrication should eliminate this cathode failure mode. Catastrophic arcing events can be prevented by using current limiting structures such as resistive layers,[40] field effect transistors (FET),[41]

and vertical current limiting (VECTL)[42] architectures. Robust materials can be used to improve cathode sputter resistance and resistance to oxidation.[43,44,45]

Cathode performance will also be affected by ion bombardment. There are two populations of ions which will bombard the cathode tips in electric propulsion systems such as Hall thrusters. One population is created between the tips and gate electrode, and the other population originates near the thruster where charge exchange (CEX) collisions occur between beam ions and neutrals. The trajectories of beam ions will not intersect the cathode, however, they will create CEX ions that can be accelerated into the cathode region. Measurements of this CEX current are discussed in Chapter 2. The energy of these ions depends on the potential between the cathode and local plasma as shown in Figure 1.6.

The second population of ions is generated near the electron emitting surface between the tip and gate electrode where emitted electrons ionize neutrals by ion bombardment. If ions are accelerated into the microtips through large enough voltage differences, these ions will damage the cathode surface. The flux of these ions is directly dependent on the local pressure. FEA cathodes have demonstrated stable emission in elevated pressure environments when start-up occurs at ~10^{-9} Torr and the pressure is slowly increased.[18] Spindt et al.[18] showed that these cathodes could operate in ~10^{-5} Torr of O_2, Ar, He, H_2, and N_2 for hundreds of hours. During these exposure tests, the emission current dropped by about an order of magnitude, if at all. When the chamber returned to the original UHV environment, the cathodes demonstrated full recoveries. Similar experiments at the Microelectronics Center of North Carolina (MCNC) yielded similar results for silicon cathodes.[46,47] The results of these experiments showed that increases in pressure increased cathode work function temporarily. Exposure experiments performed with xenon at SRI International showed that cathodes were severely damaged in a xenon environment. Tests at Linfield Research Institute (LRI) of single ZrC and HfC tips with kilovolt gap voltages showed that emission continued for

several minutes at 10^{-4} Torr of Ar and O_2. Although a glow discharge operating mode was possibly attained, the tips were not destroyed during operation for a few minutes with ions bombarding the tips with several keV energies. The results of these experiments in elevated pressure environments are very promising, especially because some of the cathodes seemed to be undamaged during operation.

Carbon cathodes are more robust than the Spindt-type cathodes, however the Spindt-type cathodes have typically demonstrated higher current densities and efficiency. These cathodes can operate at 400 V at pressures greater than 750 mTorr of nitrogen without being damaged. While performance degradation has been observed for the diamond and carbon film cathodes while operating in oxygen-rich environments[38],it is anticipated that the cathode performance will be much more stable in the inert gas environment of a xenon plasma thruster.

The effect of higher pressure environments on the lifetime of FEA cathodes has only been investigated to determine the removal rate of material from FE microtips. This model was developed by Brodie.[48] His model is used to calculate the number of ions bombarding the tips and rate of material removed from the emitting area of the tips, and depends on the sputter yield of the ion-target combination, and ionization energy, pressure, and temperature of the ambient gas. He assumed an average ion energy and corresponding ionization cross-section, Q_i, and sputter yield, Y, and employed operating voltages around 100 V. He showed that a Mo tip with a 500 Å radius of curvature, operating at 100 V, at 10^{-10} Torr of hydrogen, emitting 1 μA, will lose 10 layers of material from ion bombardment in 2×10^7 hours. With a linear relationship with pressure, the cathode will lose 10 layers of material in 200 hours at 10^{-5} Torr. The material lost rate will increase significantly with increasing ion mass. This model was developed for single tip configurations; however, a similar model could also be used for microtip structures operating at much lower voltages. At lower operating voltages, average ion energies should not be assumed because of the exponential nature of the relationship

between Q and electron energy and S and ion energy. Many models have been developed to predict the performance of FEA cathodes as a function of tip radius. Performance models have never been coupled with Brodie's model to determine the effect of cathode sputtering in higher pressure environments on cathode performance.

1.4.2 Space-Charge Limited Emission

The second concern with integrating FE cathode with EP and tether technologies is space-charge limited electron emission when emitting into plasma. FE cathodes typically employ a close-spaced triode configuration with a physical anode only millimeters away from the gate electrode to collect the emitted current. Hall and ion thrusters employ anodes and cathodes separated by a plasma with pressures up to 10^{-4} Torr in the ionization regions. In this environment, a virtual anode will collect the emitted electron current at the cathode sheath boundary. The thickness of this sheath and potential drop through it depend on the environment, cathode potentials, and properties of the emitted current. Hall thrusters typically operate in a configuration where the cathode is floating. The cathode sheath voltage is approximately 20 V in a 1.35 kW Hall thruster system with a 300 V anode-cathode voltage difference. Hollow cathodes use propellant in addition to the primary supply to the anode to generate a plasma at the emitter surface to reduce space-charge effects and the cathode sheath voltage. A reduction in sheath voltage improves the efficiency of the thruster since less of the discharge voltage is tied up in the cathode fall and a higher voltage is available to accelerate the ions to produce thrust. It is more crucial that the cathode potential is low with respect to plasma potential when FE cathodes are used because of the lifetime limitations induced by ions sputtering the microtip structures and gate electrode. It is important that the gate electrode potential is lower than the plasma potential to retard the collection of plasma electrons while the cathode beam electrons escape to the plasma. It is anticipated that the field emitter gate

electrode will be set at approximately 20 V below plasma potential, ϕ_c. A potential diagram is shown in Figure 1.6. The thruster discharge voltage between the anode and cathode, V_d, and the gate voltage with respect to the cathode FE surface, ϕ_g, are shown. In a plasma environment with virtual anodes, space-charge effects will limit the electron current that escapes through the sheath to the plasma. This concern must be properly addressed and current limits must be determined using sheath modeling before FE cathodes can be designed and used in plasma environments.

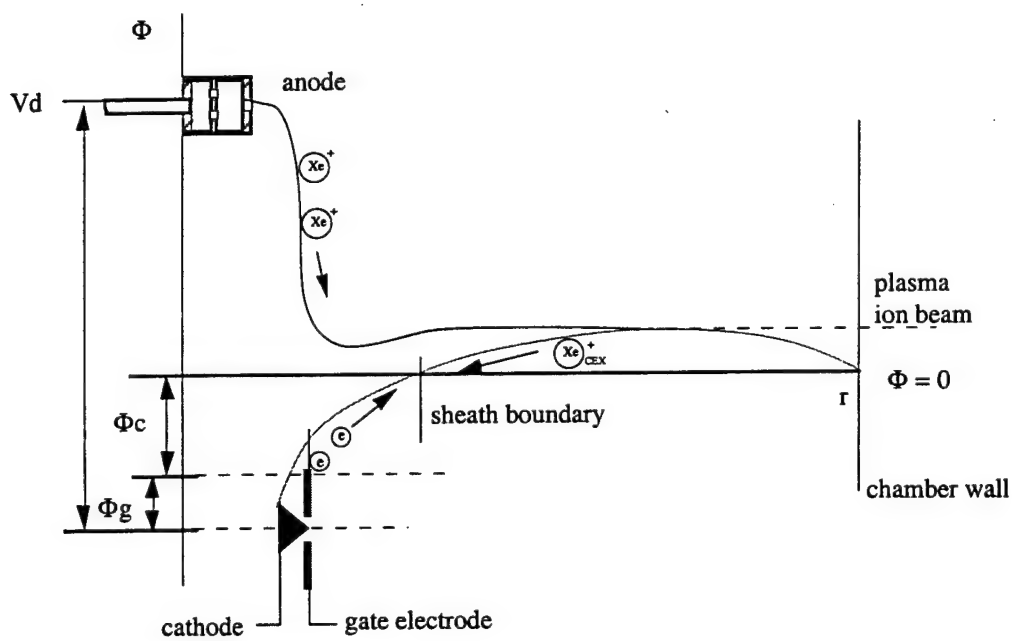

Figure 1.6 Potential diagram of the cathode, thruster, and plasma configuration. Anode, plasma ion beam, sheath boundary, gate electrode, and cathode potentials are shown relative to ground.

Space-charge limited current problems have been studied extensively. The Childs-Langmuir relationship describes space-charge current limitations in a vacuum diode. In the derivation, the current was limited by a zero electric field at the cathode surface because initial electron velocities were negligible.[49],[50] Fay et al. determined

emission current limitations in a parallel plate geometry when electrons are emitted with considerable velocities in a vacuum.[51] In that case, positive electric fields at the cathode surface are stable solutions to the Poisson equation, permitting larger currents to escape from the cathode. Virtual cathodes can eventually form between the cathode and anode to limit the emitted current. Langmuir considered space-charge limitations for parallel plates separated by a plasma, where ions contribute to negative space-charge neutralization to further increase space-charge limited current. He claimed that electron and ion currents were limited in proportion to ion and electron masses when ion and electron initial velocities are negligible, but showed that these currents can increase with non-zero velocities at the sheath boundary.[52] Bohm modeled the sheath near the cathode and determined that for a cathode sheath to be stable, the ions must enter it with non-zero initial velocity.[53] To ensure that potential minima occur only at sheath boundaries for a non-emitting cathode, it was determined that $v_i>(T_e/m_i)$^1/2 at the sheath boundary. Crawford and Cannara[54] considered the case for space-charge limited emission of a hot cathode into plasma. They determined a valid velocity range for ions entering the sheath, the velocity being limited by charge-exchange and momentum exchange collisions in pre-sheaths. Prewett and Allen[55] studied the same configuration, and included a criterion derived by Andrews and Allen[56] to construct an analytical expression for the initial energy of ions entering a sheath. Using that expression in the sheath model, they achieved excellent correlation between theory and experiment. Goodfellow augmented this model by considering the initial thermal velocities of the electrons emitted at the cathode. He used this sheath model combined with thermal models to predict cathode temperatures in a magnetoplasmadynamic thruster system. He also achieved good correlation between experiment and theory.[57]

1.5 Role of this Thesis

It is anticipated that the successful integration of FE cathodes with EP systems will require the modification of currently existing Hall thrusters, more advanced FE cathode technology, and an understanding of how these cathodes will operate in plasma environments. Thrusters will require different start-up sequences than commonly used, to protect the cathode. Lower work function materials, smaller cathode dimensions, and current limiting structures will significantly improve the performance and compatibility of these cathodes with electric propulsion systems. Testing of FE cathodes in Xe environments similar to Hall thruster environments is necessary to study the effect of higher pressure environments and operating voltages on cathode lifetime. This process should also be modeled to expedite the development and integration process, reduce costs, and to determine how to optimize cathode design for different applications. Also, space-charge limited emission should be modeled for the FE cathode and virtual anode configuration to develop and understanding of the performance and cathode current limitations due to space-charge effects in plasma environments. Some of the modeling results should be experimentally validated. This thesis tackles a few of these technological hurtles including performance assessment of available FE cathodes in simulated thruster environments, the development of a model of the performance degradation due to cathode sputtering by ion bombardment, and a model to predict space-charge limited emission from a FE cathode in a plasma environment.

The primary objectives of this work were to determine if field emission cathodes can operate in thruster environments and what limitations should be expected. Cathode lifetime and space-charge limited electron emission are focal points in this investigation. It is assumed that FE cathodes with current limiting configurations will soon be available to eliminate arcing between tips and gate electrodes as a cathode failure mode.

The first stage of this research focused on characterizing the cathode environment of a Hall thruster. A 70 mm Hall thruster, PEPL-70, was built and used in the cathode environment characterization. The performance of the thruster was evaluated to ensure nominal operating conditions were achieved. Ion current densities were measured in the cathode region of the thruster using a Faraday probe. A neutral particle flux (NPF) probe was used to measure the local pressure. These measurements were used to design experiments and model the effect of the thruster environment on FE cathode performance. The PEPL-70 thruster configuration represents only one of the possible applications of FE cathodes to electric propulsion. Initial FE cathode and thruster testing will be conducted with a thruster of this size and power level, therefore this thruster environment was simulated for initial FE cathode testing.

Experiments were conducted to evaluate the performance of FE cathodes in environments representative of Hall thruster environments. The performance of carbide cathodes was evaluated in argon and oxygen environments. The performance response of molybdenum, silicon, and carbon film cathodes to increases in xenon pressure was investigated at different operating voltages and pressures. The objectives of these experiments were to determine if xenon exposure during operation would change the cathode work function and if the cathodes could be operated at low enough voltages to avoid damaging them during ion bombardment.

A model was developed to predict performance degradation of microtip cathodes in xenon environments. This model uses a cathode performance model developed by Jensen to predict effective tip radius and spread in radii of an array of cathode tips from an I-V trace to predict the cathode performance. The performance degradation model also uses a model developed by Brodie to predict the rate of removal of material from the microtip emitting area. These models are combined with models which predict changes in effective tip radius and spread in tip radii in time to estimate the change in current emitted by a field emission array cathode during xenon ion bombardment. The model

flow diagram is shown in Figure 1.7. Experimental data and this performance degradation model were used together to estimate the energy thresholds for sputtering of Mo and Si by xenon ions. With this model the performance degradation can be predicted for any Mo or Si FEA cathode operating in a Xe environment. Good agreement was achieved between modeling and experimental results. This model can also be used as a tool to optimize the cathode configuration for various applications.

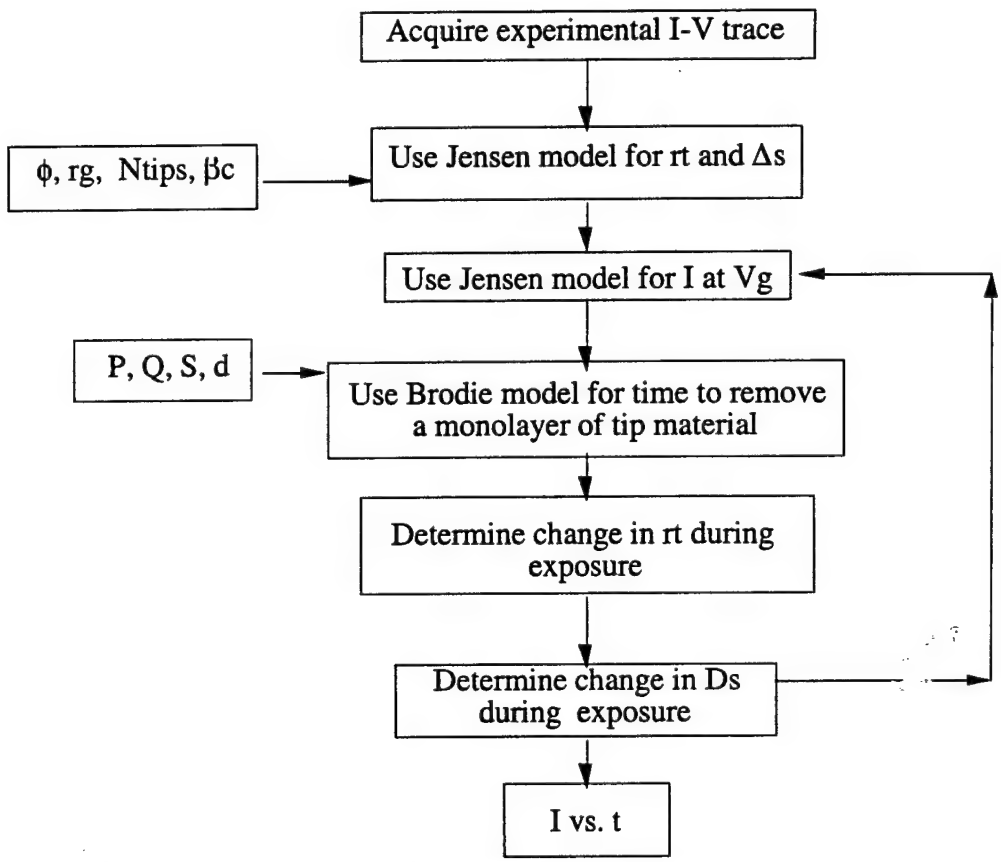

Figure 1.7 Flow diagram for the field emission array cathode performance degradation model.

A model was developed to predict space-charge current limitations of FE cathodes emitting into thruster and tether environments. This model is based on the planar sheath models developed by Goodfellow and Prewett and Allen. The criterion derived by Andrews and Allen was used to estimate the ion velocity at the boundary

between the sheath and pre-sheath. The model developed in this research considers electrons emitted with energies greater than 20 eV. This model also considers cylindrical and spherical sheath geometries to model situations in which electron beam expansion occurs in the sheath as $1/r$ and $1/r^2$, respectively. Beam expansion must be considered in the cases when the sheath dimensions are larger than the cathode dimensions. These models were used to investigate the effect of cathode environment and dimensions on the space-charge current limit.

Finally, the modeling and experimental results are applied to design cathodes for thruster and tether applications. Preliminary cathode design objectives are ~100 mA from an area smaller than 1 cm^2 for 100 hrs. Cathode lifetime and space-charge current limitations are considered in the designs. Cathode geometrical and operating configurations are suggested for the different applications.

CHAPTER 2

CATHODE ENVIRONMENT CHARACTERIZATION

The cathode environment of a Hall thruster must be understood to determine the compatibility of Hall thrusters and FE cathodes. A Hall thruster was built and operated with xenon propellant to provide a plasma environment which is similar to the plasma environment of a commercial system. The performance of the thruster was evaluated with I-V and thrust measurements. Faraday and Neutral Particle Flux (NPF) probes were used to measure ion current density and neutral particle pressure in the region of a Hall thruster where FE cathodes could be positioned. Electron number densities and temperatures on a similar Hall thruster system were measured elsewhere.[58] Parameters obtained from cathode environment characterization were used to design FE cathode experiments in xenon environments and model the effect of the thruster environment on cathode performance and lifetime. The thruster developed, diagnostics used to characterize the cathode environment, and the measurements obtained in the cathode environment characterization are discussed in this chapter.

2.1 Experimental Apparatus

2.1.1 Test Facility

These experiments were conducted at the Jet Propulsion Laboratory (JPL). The test facility consisted of a 2.3 x 4.6 m vacuum chamber with a xenon pumping speed of 30,000 l/s and base pressure of 4×10^{-6} Torr maintained by both diffusion and cryogenic

pumps. The pressure gauge was calibrated against a xenon calibrated ionization gauge. A JPL hollow cathode was used to supply electrons for propellant ionization and ion beam neutralization. Thruster performance was evaluated using a NASA GRC designed inverted pendulum thrust stand.[59] Calibration data are shown in Figure 2.1. The thrust stand is an inverted pendulum type with a Linear Voltage Digital Transducer (LVDT) that detects movement of the thrust stand. An inclinometer and motor are used to maintain a constant thrust stand inclination because changes in inclination can be detected by the LVDT as artificial thrust. A motor drives the deployment of a chain with calibration weights distributed at several positions. The weights are deployed periodically and the LVDT displays the voltage corresponding to the thrust stand displacement during calibrations. During the calibrations, the weights deployed shift the LVDT from its zero weight (thrust) position associated with a voltage output, V_{LVDTo}. A change in voltage from the zero position is then associated with each calibration weight to estimate thrust during thruster operation. This thrust stand was calibrated for much larger thrust levels than the PEPL-70 generated; therefore, the thrust estimates had to be extrapolated from the calibration curve. Thrust stand response has been shown to be linear to very low thrust levels.

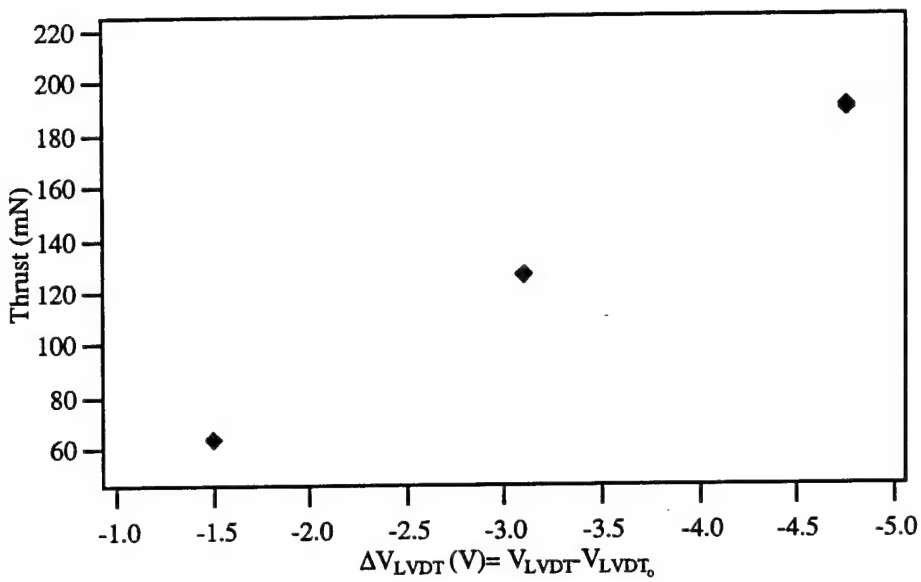

Figure 2.1 Thrust stand calibration data.

2.1.2 Hall Thruster-PEPL-70

Limited Hall thruster availability necessitated the fabrication of a laboratory model at the PEPL. Fabrication of this thruster was also necessary to investigate performance of Hall thrusters with oxygen propellant. Oxygen can be very destructive to the thruster. Different thruster designs and materials are optimal for operation on oxygen and xenon. The boron nitride discharge chamber has a 70 mm average diameter. The titanium anode has one propellant inlet into a gas distributor with 48 outlets in the first chamber and 24 outlets in the second chamber. Two chambers with different radial locations of the propellant outlets improve the azimuthal uniformity of xenon in the discharge chamber. The magnetic poles in this thruster are slightly thicker than the pole pieces commonly used in xenon thrusters to create a larger ionization region because ionization of oxygen requires a longer path length. The ionization region is confined by the magnetic field generated by the electromagnets. The thruster, shown in Figure 1.3 and Figure 2.2, employs outer and inner electromagnets to generate a radial magnetic

field. Hall thrusters commonly used 4 outer electromagnets; however, this thruster employs 8 outer electromagnets to improve azimuthal uniformity in the magnetic field. An axial electric field is maintained between the anode and cathode. The axial electric field and the radial magnetic field create a closed Hall current of electrons. Propellant atoms injected into this electron cloud through the anode-gas distributor are ionized by electron bombardment. The ions are then accelerated axially out of the discharge chamber by the electric field to generate thrust.

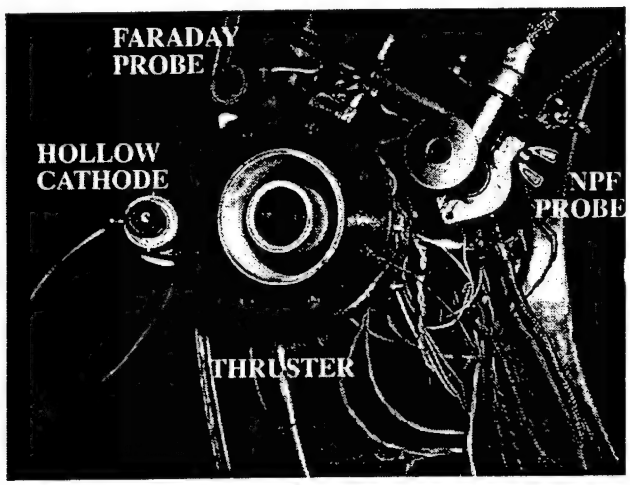

Figure 2.2 The PEPL-70 Hall thruster with a hollow cathode, neutral particle flux (NPF) probe, and Faraday Probe.

2.1.3 Diagnostics

Faraday and neutral particle flux (NPF) probes were used to characterize the cathode environment. A Faraday button probe which was developed at JPL, shown in Figure 2.3, was used to measure ion current densities in a region external to the thruster where a FE cathode could be used. A schematic for the Faraday probe is shown in Figure 2.3. A NPF[60] probe was used to measure neutral particle pressures in the cathode region. This probe measures neutral particle pressure by using a series of retarding grids to

deflect ions entering the ionization gauge. A thermocouple provides the probe wall temperature. It is assumed that the temperature of the gas is in equilibrium with the probe walls. The NPF probe is shown in Figure 2.3. The actual positions of the cathode and probes during the measurements presented in this chapter are different than the positions shown in Figure 2.3. The cathode was at a 3 o'clock position, the NPF at 10 o'clock, and the Faraday probe at 8 o'clock.

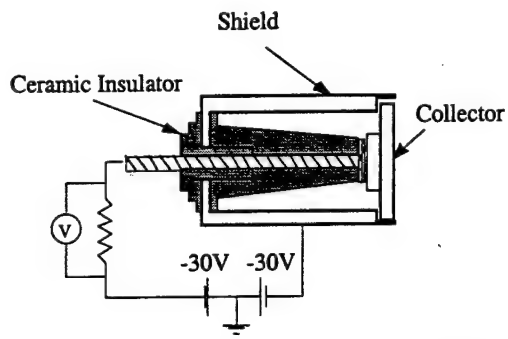

Figure 2.3 Faraday probe schematic (courtesy of James Haas).

2.2 Experimental Methods and Results

2.2.1 Thruster Performance

During several hours of testing, the thruster demonstrated I-V trends comparable to similar Hall thrusters used for satellite NSSK. Figure 2.4 shows I-V data at different propellant flow rates. A properly operating Hall thruster will demonstrate a steep I-V curve at low voltages, followed by a steep drop, and then a plateau in current with further increases in discharge voltage. The thruster is operating optimally in the plateau region of the I-V curve; increases in discharge voltage increase the ion exit velocities while the ionization fraction of the propellant does not change.

During several hours of testing, the thruster demonstrated short-term performance comparable to similar Hall thrusters used for satellite north-south station keeping. A 1.4 kW commercial Hall thruster system generates 4.5 A at 300 V and 53 sccm of xenon with 83 mN of thrust at 53 % efficiency.[3] The PEPL-70 generated 4.6 A and 65 mN of thrust at 36% efficiency, 300 V, and 43 sccm of xenon. Thrust efficiency, η_{eff}, is determined using Eqn. 2.1, where $\dot{m}$ is the mass flow rate of propellant (mg/s), T_N is thrust (N), I_d is the discharge current (A), and V_d is the discharge voltage (V). Performance data are shown in Figure 2.5. The error bars on these measurements are fairly large because the thrust stand was configured to measure thrust on much larger propulsion systems with much higher thrust levels, and the zero drift of the LVDT was significant during the experiments. During the experiments, the thrust is estimated by the thrust stand position with respect to the initial zero thrust position. A shift in the thrust stand zero position during the experiments can result in significant over- or underestimates in thrust. The most accurate method of determining thrust is to run the thruster at the operating point of interest for at least 0.5 hour and then turn it off to determine the zero point of the thrust stand and the thrust associated with the LVDT voltage reading before the thruster was turned off. Time limitations prevented the acquisition of such accurate thrust measurements in these experiments. Operating points were only explored for a few minutes. The thrust stand was calibrated before and after the experiments. The calibration taken after the experiments is shown in Figure 2.1. The thrust stand zero thrust point shifted significantly during the experiment. Therefore, the actual thrust can be bound using the initial and final zero points and the final calibration. The error bars on the measurements shown in Figure 2.5 reflect the spread in thrust values estimated, which is a result of the thrust stand zero position shift.

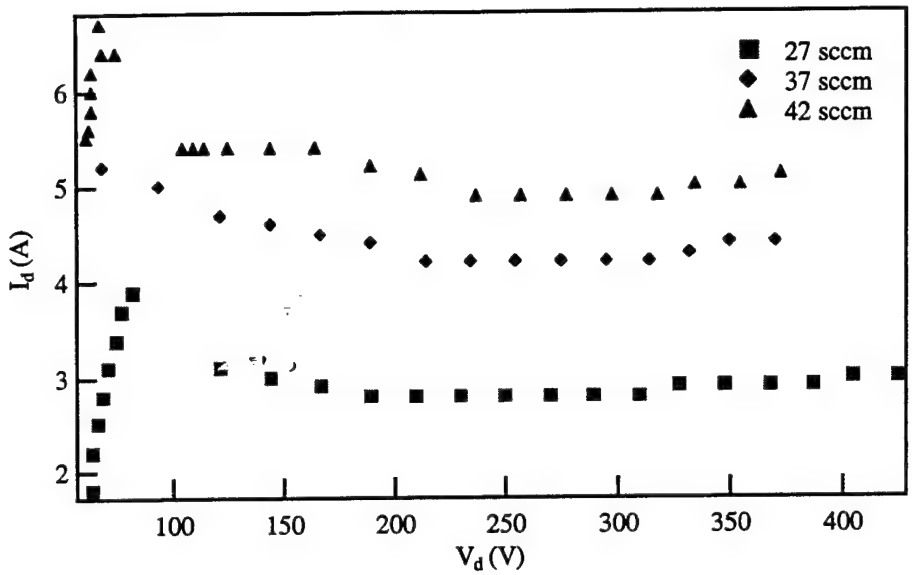

Figure 2.4 I-V curves from the PEPL-70 at different xenon volumetric flow rates.

V_d (V)	$\dot{V}$ (sccm)	I_d (A)	T (mN)	η_{eff}(%)
300	23.4	1.8	26.1	27
300	27.4	2.4	33.8	29
300	34.0	3.2	45.4	32
300	38.6	3.8	55.3	35
300	43.0	4.6	65.4	36

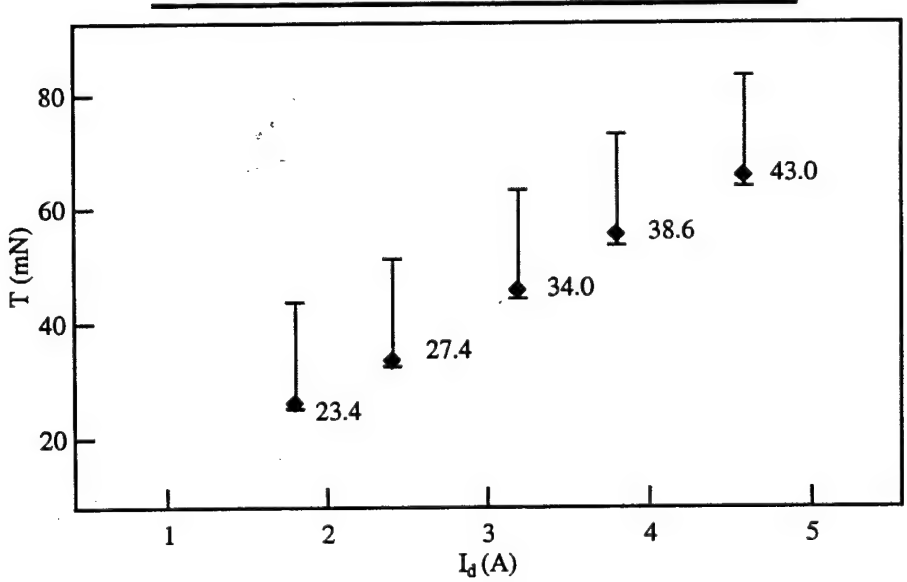

Figure 2.5 Thruster performance data with varying propellant flow rate and a constant discharge voltage, 300V. The numbers on the markers on the graph correspond to the total propellant flow rate (sccm). The table above the graph shows the discharge current also.

Eqn. 2.1 $$\eta_{eff} = \frac{T_N^2}{2\dot{m} I_d V_d}$$

2.2.2 Xenon Pressure and Ion Current Density in Cathode Region

Xenon pressure and ion current density were measured at several thruster operating points. The NPF probe showed that the pressure in the cathode region of a Hall thruster at each operating point is primarily attributed to the neutral particles; retarding the ions had virtually no effect on the measured pressures. Table 2.1 shows data acquired with the Faraday probe flush with the exit plane of the thruster. Corresponding NPF data are not available. Table 2.2 shows data taken with both probes positioned 3 mm behind the physical exit plane of the thruster.

Table 2.1 Ion current densities measured by the Faraday probe flush with the exit plane of the thruster. Discharge voltage and current, electromagnet inner, I_{MI}, and outer, I_{MO}, currents, and Xe pressures are also given.

$\dot{V}$ (sccm)	I_d (A)	V_d (V)	I_{MI}(A)	I_{MO}(A)	P_{tank} (Torr)	J (mA/cm^2)
23.8	1.9	259	19	8	1.1×10^{-5}	0.010
23.8	1.9	300	19	8	1.1×10^{-5}	0.010
28.6	2.7	298	18	5	1.3×10^{-5}	0.013
33.5	3.5	298	18	5	1.5×10^{-5}	0.018
38.0	3.5	300	28	15	1.7×10^{-5}	0.014
42.7	4.5	300	26	7	1.9×10^{-5}	0.019
43.1	4.9	300	27	0	1.9×10^{-5}	0.020

Table 2.2 Neutral Xe particle pressures and ion current densities measured by the probes 3 mm behind the physical exit plane of the thruster.

$\dot{V}$ (sccm)	I_d (A)	V_d (V)	I_{MI}(A)	I_{MO}(A)	P_{tank} (Torr)	P_{NPF} (Torr)	J (mA/cm^2)
18.7	1.3	260	25	12	8.0×10^{-6}	2.1×10^{-5}	0.001
19.1	1.3	280	25	12	8.3×10^{-6}	2.1×10^{-5}	0.001
19.4	1.3	302	25	12	8.3×10^{-6}	2.1×10^{-5}	0.001
23.5	2.0	200	27	7	9.8×10^{-6}	8.9×10^{-6}	0.003
23.4	1.8	300	27	7	1.0×10^{-5}	9.1×10^{-6}	0.002
27.4	2.4	300	27	7	1.2×10^{-5}	9.1×10^{-6}	0.003
34.0	3.1	300	27	8	1.4×10^{-5}	1.3×10^{-5}	0.005
38.6	3.8	300	27	8	1.9×10^{-5}	1.7×10^{-5}	0.006
43.0	4.6	300	26	8	1.9×10^{-5}	1.6×10^{-5}	0.008

Data in Table 2.1 and Table 2.2 show that xenon pressure measurements by the NPF probe near the thruster could be higher or lower than tank pressure. This relationship depends on the ionization fraction of the propellant exiting the thruster, and the ion optics of the thruster, which depend on the discharge voltage and currents in the electromagnets. The ion optics were typically optimized for this thruster at each propellant flow rate and discharge voltage by adjusting the currents in the electromagnets.

The measurements obtained in the experiments discussed in this chapter will be used in the following chapters of the thesis to determine the effect of this thruster environment on cathode performance and lifetime. The pressure measured by the NPF probe is strongly influenced by vacuum chamber pressure. Therefore, lower pressures are expected in the cathode region in lower pressure environments. Ion current densities of 0.02 mA/cm^2, and local pressures up to $2x10^{-5}$ Torr were used in the models and experimental performance evaluations to estimate lower limits on the cathode lifetime. These measurements must be conducted on any thruster that could use FE cathodes to assess their compatibility.

CHAPTER 3

FIELD EMISSION CATHODE EXPERIMENTS

FE cathodes are typically used in UHV environments where lifetimes of thousands of hours have been demonstrated. The experimental results discussed in the previous chapter show how hostile the thruster environment is, with pressures several orders of magnitude higher than the UHV environments preferred for these cathodes. In this environment, FE cathodes can become contaminated and can be sputtered by ions which are created by the electrons emitted from the cathode and CEX ions originating near the thruster. Cathode environment characterization was conducted only with xenon propellant; however, there is also interest in using these cathodes in oxygen environments, as discussed in Chapter 1. Preliminary experiments were conducted in hostile environments at the Linfield Research Institute (LRI) to determine if single FE cathode tips can operate in argon and oxygen environments with pressures as high as $\sim 10^{-5}$ Torr. The results of these preliminary experiments were promising; therefore, the investigation into the compatibility of these two technologies continues. FEA and carbon film FE cathodes were later obtained for performance characterization in UHV environments and performance degradation experiments in xenon environments. Experiments were conducted on single FE tip, FEA, and carbon film FE cathodes to study the emitting area of single tips, emission stability in higher pressure environments, changes in work function due to contamination by the environment, and the effects of gate and anode electrode voltages on cathode sputtering. The results of these experiments are discussed in this chapter.

3.1 Carbide Single Tip Cathode Experiments

Single carbide FE cathode testing conduced at LRI focused on determining if FE cathodes could operate in oxygen and argon environments at pressures as high as 10^{-5} Torr. This investigation also focused on gaining an understanding of the effect of argon and oxygen exposures on the performance of single carbide FE tips.

3.1.1 Cathodes

Single HfC and ZrC FE cathodes were fabricated and tested at the Linfield Research Institute (LRI). Carbide FE cathode work has been the primary focus at LRI for the past several years. FEA cathodes have been coated with carbides at LRI, however most of the cathode fabrication work at LRI focuses on single tips that are fabricated from commercially available sintered carbide rods. The rods are crystallized at LRI through a process of floating zone arc refinement[61] with carbon to metal ratios of the single crystal specimen typically less than one. The zone refined rods are ground to 0.75 mm diameters and then sandwiched between two 0.5 mm pyrolytic carbon blocks in a Vogel-type mount. The rod and blocks are in spring tension between two Mo-Re posts on a ceramic base. A single tip carbide cathode in the Vogel-type mount is shown in Figure 3.1. The FE cathode is then formed by electrochemical polishing of the rod into a sharp tip. This fabrication process produces cathodes of varying tip radii and cone angles. After fabrication, the cathodes are imaged in a scanning electron microscope (SEM) to determine the cathode structure. In UHV environments the cathodes are 'flashed' to temperatures greater than 1900 K by resistively heating the cathode base. This process removes oxygen and other impurities from the cathode surface. Field desorption is commonly used to smooth an uneven tip surface by positively biasing the tip to ~10 kV.

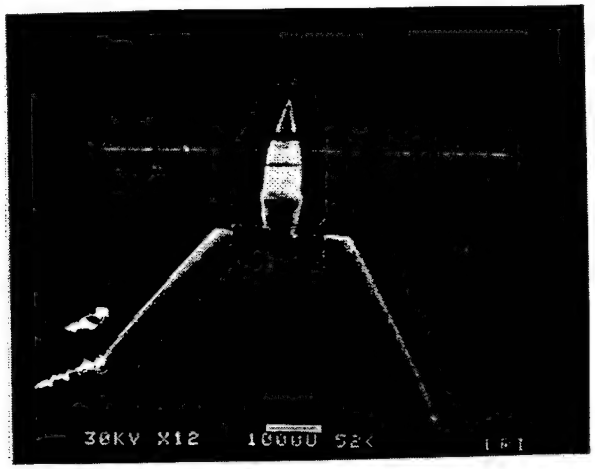

Figure 3.1 A scanning electron microscope (SEM) micrograph of a single carbide cathode in a Vogel-type mount.

3.1.2 Experimental Apparatus

Carbide cathode testing was performed at LRI in UHV facilities. Two vacuum chambers were primarily used in the experiments. They employed mechanical, turbo, and ionization pumps to attain pressures as low as 10^{-10} Torr. The vacuum chambers employ Field Emission Microscopes (FEM) which have phosphor coated glass with a tin oxide conductive coating that serves as the anode. The cathodes are positioned a few centimeters behind the anode; therefore, several kilovolts are required from the anode power supply to provide the electric fields at the cathode tips necessary for field emission. As the anode collects the current emitted by the cathode, the film phosphoresces from electron bombardment. The image observed on the phosphor coated glass is a highly magnified representation of the emission pattern on the cathode surface. The FEM configuration is illustrated in Figure 3.2 showing a pattern that has been observed. An electrical schematic for the FEM is shown in Figure 3.3. A Keithly 485 picoammeter was used to measure emission current. A 1-20 MΩ resistor was used to limit the cathode current to prevent cathode destruction as a result of arcing between the tip and anode.

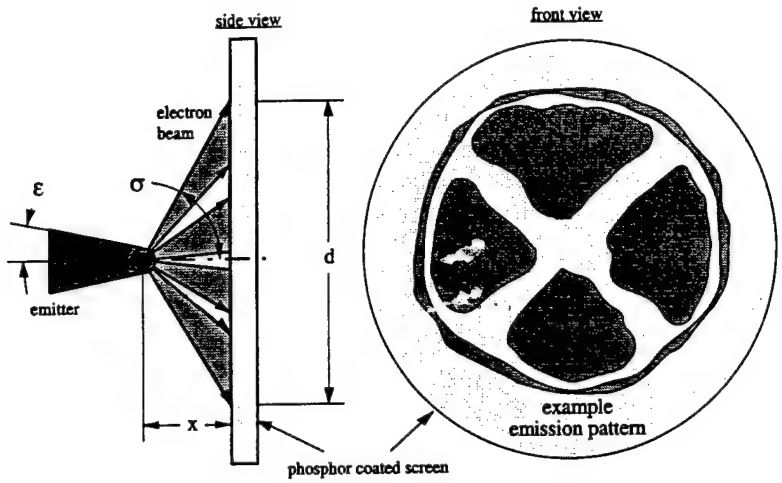

Figure 3.2 An illustration of how the field emission microscope (FEM) was used to determine the emitting area of the tip from the angle, σ, which can be calculated from the size of the emission pattern, d, on the screen at a distance x from the emitter.

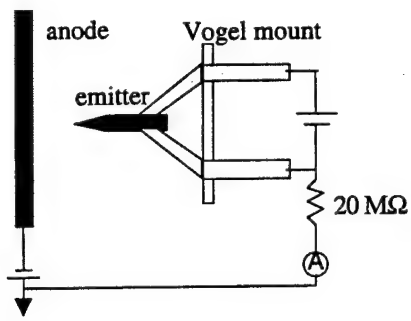

Figure 3.3 Electrical schematic of the FEM.

3.1.3 Experimental Methods and Results

Twenty-seven HfC and ZrC cathodes were fabricated and tested in FEMs at LRI. SEMs were used to image the cathodes after they were fabricated to determine the cone angles of the cathodes and radii of curvature of the tips. The tips were also imaged after the experiments to quantify changes in tip structure. The resolution of the SEM was approximately 10 nm. The radii of the tips fabricated and tested were typically much larger than 10 nm. The FEM was used to observe emission patterns from the cathodes.

Because different crystal planes in the carbides have different work functions, electron emission is not uniform from the cathode tip. Instead, the majority of the emission current originates from the low work function planes. The pattern observed on the FEM screen indicates where the tip is centered in the crystal structure and which planes are most strongly emitting. Organized patterns are only observed for clean cathodes. The size of the pattern is indicative of the area of the cathode that is emitting, which is a function of half-cone emission angle, σ, and the tip radius, r_t. FEMs were used to measure σ, with $\tan(\sigma)=d/2x$, as shown in Figure 3.2. Current-voltage (I-V) traces give insight into the emission stability, and changes in work function and tip radius.

The SEM and FEM were used to gain a better understanding of the cathode dimensions and characteristics required for performance modeling. SEM images of cathodes used in this investigation showed that the average half-cone angle of the emitting tip is 0.26 radians (16°). Tip radii, measured in the SEM, ranged from 40-270 nm. The half cone emission angle, σ, ranged from 8-44°, averaging 28° for eight cathodes tested. FEM images show that electron emission from the area, defined by the tip radius and half cone emitting angle, was not uniform. In fact, only a small fraction of that area is emitting. Figure 3.4 shows an emission pattern observed in the FEM. The patterns shown in Figure 3.4 are representative of a fairly clean tip, while the patterns shown in Figure 3.5 are representative of an emission pattern from a cathode before flashing it or performing field desorption. Organized patterns were never observed from some cathodes, even after flash cleaning and field desorption.

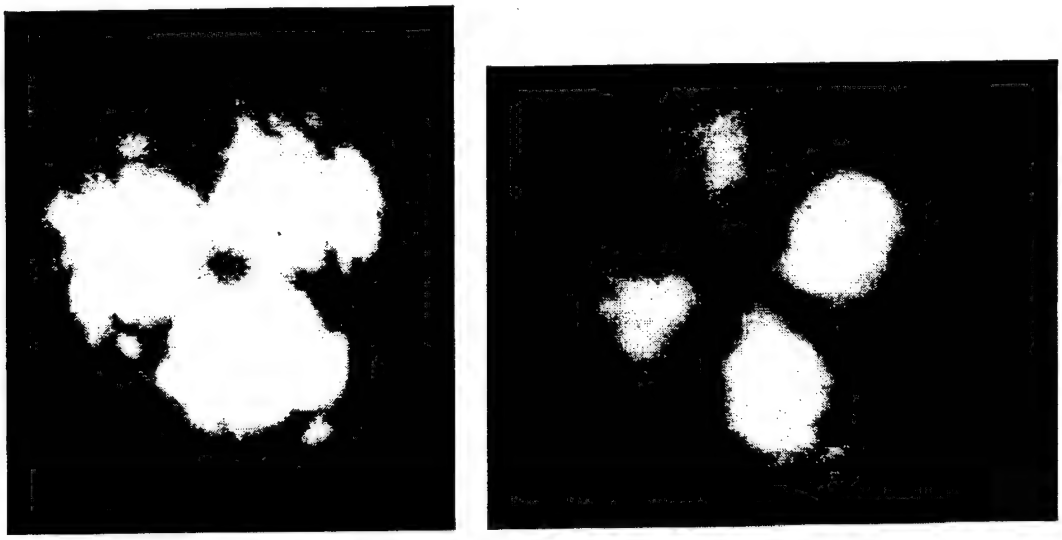

Figure 3.4 Emission patterns observed with the FEM from fairly clean carbide cathodes.

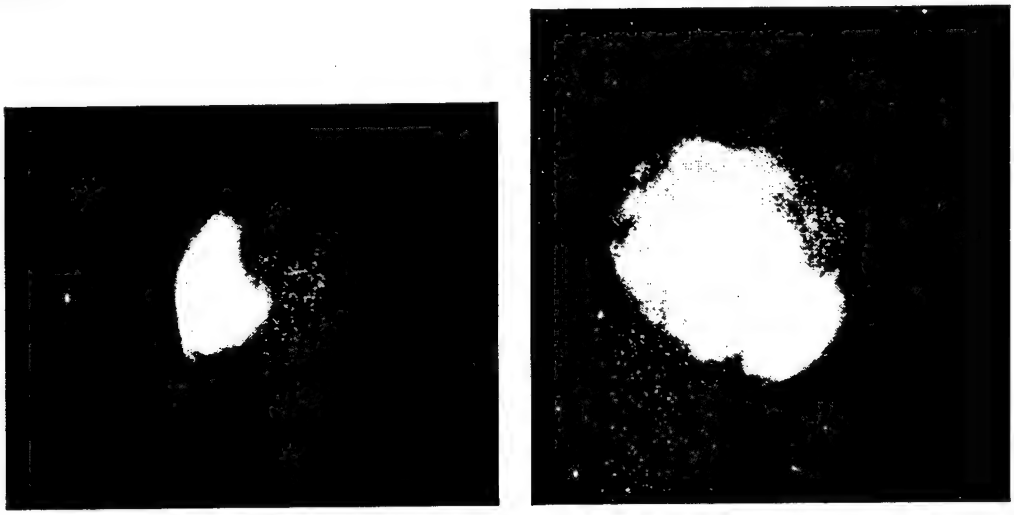

Figure 3.5 Emission patterns observed with the FEM from damaged or contaminated carbide.

The effect of contamination and ion bombardment on cathode performance was investigated in argon, oxygen, and air environments with promising results. These experiments were conducted in much more hostile environments than the cathode will be subjected to when used with propulsion systems. Operating voltages were several kilovolts in the FEM because the distances between the tips and anodes were ~1 cm; however, they will be only a few tens of volts in field emitter array configurations when

used with Hall thrusters. The cathodes demonstrated more stable performance in UHV environments than in higher pressure environments. Using a ~1MΩ resistor behind the tip did prevent catastrophic arcing between the tip and anode during unstable operation in argon and oxygen environments; however, it did not regulate the current enough in every experiment to prevent tip melting. Experimental results showed that cathodes operating at ~1 μA at $3x10^{-8}$ Torr were rarely stable; the current typically slowly degraded with time. However, in one experiment the cathode stability improved significantly when the current was increased up to 80 μA at 3 kV. Electron emission from this cathode was incredibly stable for more than one hour. In other experiments, the cathodes were exposed to oxygen to determine if oxygen radicals and ions would sputter and contaminate the cathodes to quickly destroy them. The HfC cathode was conditioned at $9x10^{-10}$ Torr by running it and flashing it. With the cathode emitting 1 μA, the oxygen pressure was increased up to ~10^{-6} Torr. Some current reduction was observed; however the emission pattern on the FEM screen improved, showing enhanced emission from sites not previously detected in the FEM. The cathode continued to operate when pressures reached 10 mTorr by accident. At this pressure the cathode was voluntarily turned off, but was not destroyed.

In another set of experiments, a ZrC cathode was exposed to $3x10^{-5}$ Torr of argon for ~0.5 hr. The cathode was turned on at $3x10^{-10}$ Torr. It was flashed several times; however, the pattern observed with the FEM was not representative of a clean emitter. After the argon pressure was increased up to $3x10^{-5}$ Torr with ~20 μA and ~6 kV, a pattern started to develop, as shown in Figure 3.6a. After several minutes, it is believed that a glow discharge developed. The emission pattern grew into a solid disk, as shown in Figure 3.6b, and the current jumped up to a few hundred microamperes. The argon gas was then evacuated from the vacuum chamber and the pressure returned to 10^{-9} Torr. After the exposure, returning to UHV, and flashing the cathode, the emission current was incredibly stable and the emission pattern was representative of a clean cathode. The

post-exposure FEM image is shown in Figure 3.6c. Post-exposure examination of the cathode with the SEM showed no measurable damage by ion bombardment from exposure to argon ~10^{-5} Torr and 6 kV. I-V curves taken before and after the cathode was exposed to argon while operating are shown in Figure 3.7. This figure also shows a Fowler-Nordheim (F-N) plot of the Current–Voltage (I-V) data, on which $\ln(I/V^2)$ is plotted vs. 1/V. The argon ion bombardment actually cleaned the cathode and improved the emission stability, as shown by the increased linearity of the F-N curves. The change in slope of the F-N curves shown in Figure 3.7 indicates a change in tip radius. Before the exposure, emission could have been originating from nanoprotrusions on the cathode tip. During the exposure the surface was smoothed and cleaned to increase the effective tip radius. The emission current was reduced at the low-voltage end of the I-V trace, and increased at the high-voltage end of the trace.

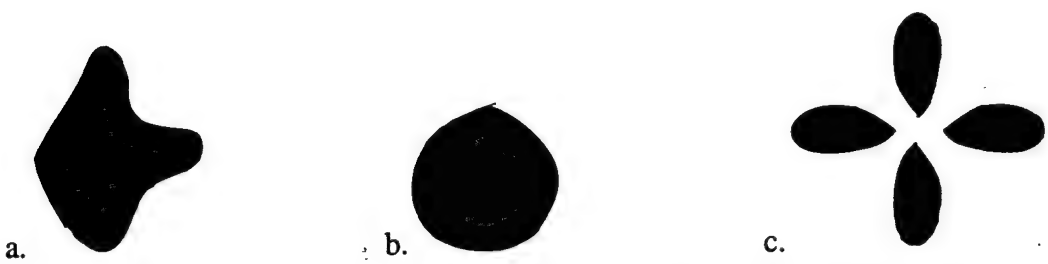

Figure 3.6 Evolution of the tip emission pattern observed with the FEM a,b) during and c) after the exposure to argon.

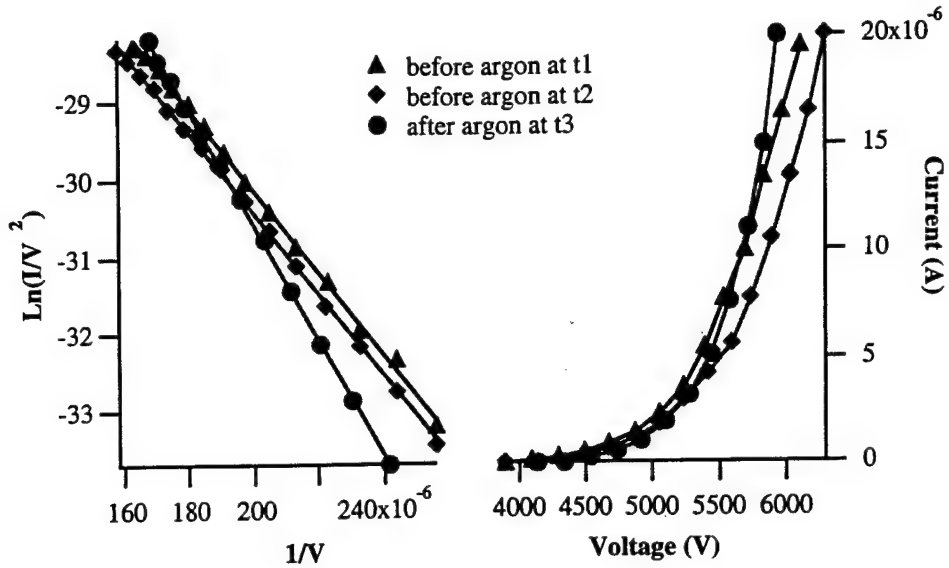

Figure 3.7 Fowler-Nordheim (F-N) (left) and I-V curves (right) obtained from the ZrC cathode before and after exposure to argon.

HfC and ZrC had already demonstrated superior performance over Mo and Si cathodes. Carbide cathodes can emit higher currents at the same voltage because of lower work functions.[62,63,64,65] In this investigation they demonstrated incredible robustness in oxygen and argon environments and resistance to oxygen poisoning.

Resistance to oxygen poisoning is critical to the successful integration of FE cathodes and oxygen fueled propulsion systems and tethered spacecraft. This cathode characteristic is also valuable when they are used with xenon thrusters because the cathodes could be frequently exposed to air during ground testing, and turn-on will occur in air partial pressures between 10^{-7} and 10^{-8} Torr. HfC and ZrC materials are preferred for thruster and tether applications; however, carbide FEA cathodes were not available for testing in this investigation.

3.2 Mo and Si Field Emission Array Cathode Experiments

Field emission array cathodes with arrays of more than 10,000 tips were used to determine the effect of xenon exposure on Mo and Si FEA cathode performance. The

advantage of these microtip cathode arrays is that the operating voltages can be less than 100 V to get 1 mA of current. The objective of these experiments is to determine if xenon adsorption will affect the work function of the cathodes and if the cathodes can be operated at low enough voltages to avoid sputter damaging the microtip structures. These experiments also resulted in estimates for energy threshold, E_{th}, for sputtering of Mo and Si targets by Xe ions which are better than those previously available. Experimental results discussed in the previous chapter showed that the xenon pressure in the cathode environment of a Hall thruster at 1.4 kW is around $2x10^{-5}$ Torr at 1.4 kW. Therefore, most of the performance evaluations were conducted at this pressure. The performance of these cathodes was not optimized in these experiments because of limited time and cathode availability. Much better performance is expected if the cathodes are tested in cleaner environments and operated at higher voltages. These experiments focused on low-voltage operation where emission currents were typically less than 1 μA.

3.2.1 Cathodes

Silicon cathodes from MCNC

The MCNC FEA cathodes used in these experiments employed 16,000 silicon tips with 2 μm aperture diameters on 10 μm centers. Four cathode arrays were fabricated on a single chip with four gate electrodes and a cathode base common to each of the arrays. The chip was mounted to a T0-5 head. Each tip in the arrays used in the experiments is similar to the tip shown in Figure 3.8.

The cathodes are fabricated at MCNC using a self-aligning tip-on-post and gate electrode process.[66] The process begins with deposition and then reactive ion etching (RIE) of a nitride film to leave circular caps on a silicon wafer. The caps are used as masks for etching silicon to form silicon posts and tips. Silicon posts are formed using an anisotropic RIE with a mixture of BCl_3, Cl_2, O_2, and He gases. The wafers are then

oxidized to sharpen the posts into tips, with the nitride caps in place. SiO_2 is then deposited onto the structure with a protective photoresist layer around the cone structures. Chromium, tantalum, and platinum gate electrode film is then deposited. The liftoff material is removed and a self-aligned gate electrode remains. The nitride caps are removed in a buffered oxide etch, and a hemispherical cavity remains around the post, as shown in Figure 3.8.

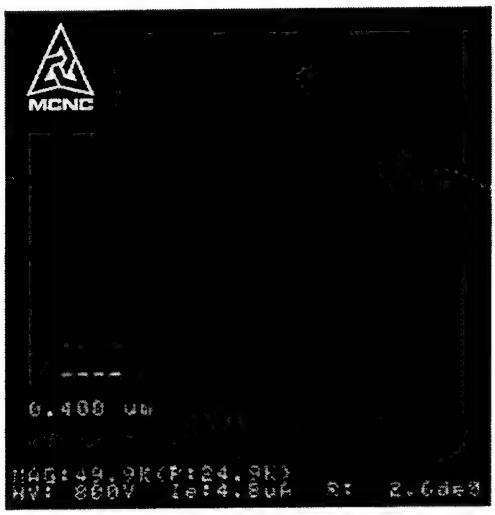

Figure 3.8 A MCNC Si field emission array single tip configuration (courtesy of MCNC).

Molybdenum cathodes from SRI

The molybdenum FEA cathode, provided by SRI International, consisted of an array of 50,000 tips with 0.9 μm gate aperture diameters on 4 μm centers fabricated on a 2000 Ohm-cm silicon wafer. The high resistivity wafer protects the cathodes against arc damage by effectively providing an isolated resistor in series with each emitter. Figure 3.9 shows a FEA cathode from SRI that was cracked in liquid nitrogen and imaged in a SEM. The cathode shown has been damaged by xenon ion bombardment. An undamaged cone is much sharper, with the tip flush with the top surface of the gate

electrode. The structure of the conical SRI cathode is significantly different from the MCNC cathode, which has a tip-on-post structure.

The molybdenum cathode used in these experiments was fabricated at SRI using a process in which the gate electrode is deposited before the tip structure. First the silicon wafer was covered with a 1 μm thick insulating layer of thermally grown SiO_2. A molybdenum film with a 0.25 μm thickness was deposited on the insulating layer. An array of 50,000 apertures with 0.9 μm diameters on 4 μm centers were then patterned on the Mo film with electron beam lithography and then etched. Cavities in the SiO_2 were then etched using the gate electrode as the etch mask. A lift-off layer was then deposited on the gate electrode. Mo was then deposited on the film forming a cone structure in the cavity as the gate aperture closed. The excess Mo was then lifted off and the cone structure remained in the cavity as shown in Figure 3.9. The cathodes are then cleaned in a H+Ne plasma.

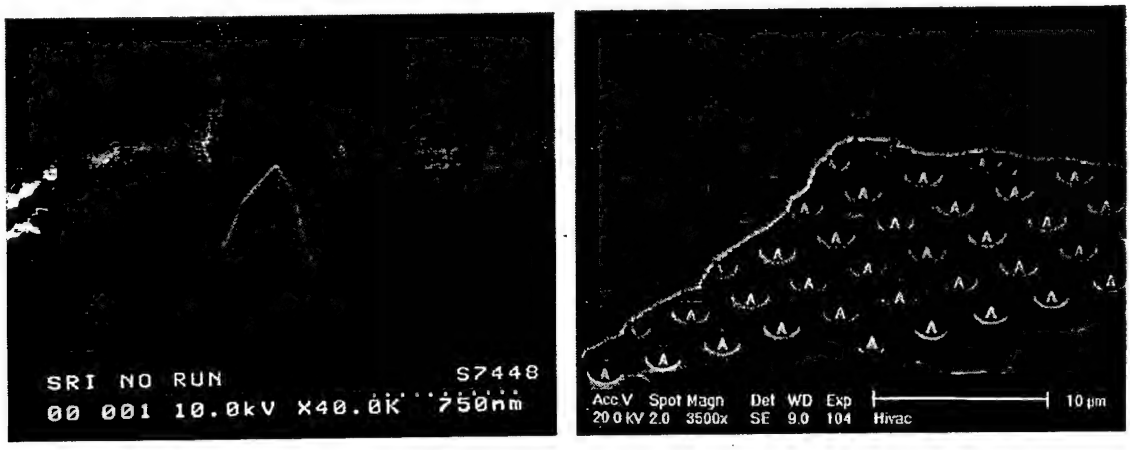

Figure 3.9 A SRI International Mo field emission array cathode single tip and array.

3.2.2 Experimental Apparatus

Silicon and molybdenum FEA cathode testing was performed at the JPL. The test facility consisted of a 0.0664 m^3 vacuum chamber that was pumped by turbomolecular, ion, and sublimation pumps to pressures as low as $7x10^{-11}$ Torr. The vacuum facility is shown in Figure 3.10. The cathodes were mounted to electrical feedthrus on conflat flanges. The cathode test flange is shown in Figure 3.11. Xenon pressure was increased using a Granville-Phillips leak valve, "The Leak". The cathodes and the ionization gauge were equidistant from the xenon inlet orifice and vacuum pumps to minimize pressure gradients between the cathodes and pressure gauge. Three Keithley 480 picoammeters were used to measure the current emitted through the base and collected by the gate electrode and anode. The picoammeters on the anode and gate electrodes floated electrically above ground to minimize the measurement of stray currents. Pressure was measured using a Varian UHV-24 nude ionization gauge. Pressure, current, and voltage signals were recorded using a National Instruments LabVIEW data acquisition system. The electrical configuration employed during the experiments is shown in Figure 3.12. A 10 MΩ resistor was used on the gate electrode for microtip cathode testing. This resistor was used to significantly reduce V_g when several microamperes of current were collected by the gate electrode, to prevent arcing between the tip and gate electrode.

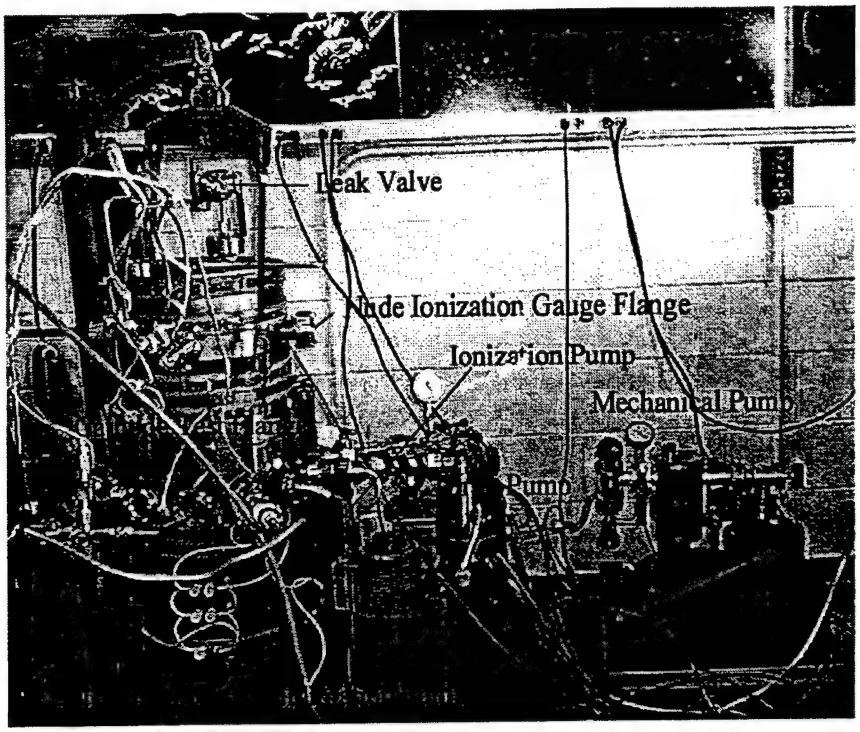

Figure 3.10 The ultra-high vacuum (UHV) facility at the Jet Propulsion Laboratory.

Figure 3.11 The field emission cathode test flange in UHV facility.

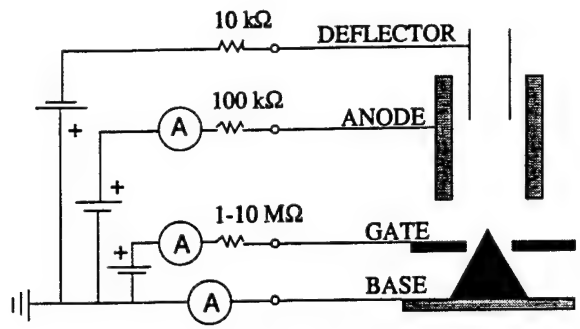

Figure 3.12 Electrical schematic for field emission cathode testing.

3.2.3 Si FEA Cathode Experimental Methods and Results

The first experiments investigated the effect of xenon exposure on the work function of a MCNC Si FEA cathode with 16,000 tips. The cathode was exposed to xenon at $2x10^{-4}$ Torr for 1 hour to provide a dose of xenon to the surface of the cathode greater than it experienced during the exposure tests at $2x10^{-5}$ Torr with the cathode operating. Data obtained during this and repeated experiments show that xenon coverage did not change the work function of the silicon cathode surface. These data are shown in Figure 3.13.

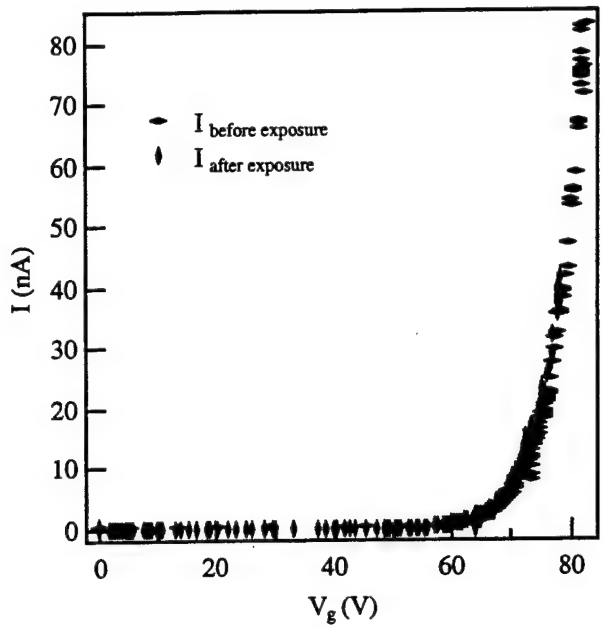

Figure 3.13 I-V curves taken before and after the Si cathode was exposed to Xe.

The objective of the next experiments was to determine if the cathode could operate at low enough voltages to avoid being sputter damaged. An experiment similar to those conducted at MCNC was conducted at JPL where the cathode was exposed to 7×10^{-6} Torr of xenon with an initial current of 20 μA. The gate voltage in this experiment was 86 V and the anode voltage was 400 V. The response of the cathode current to the increase in pressure is shown in Figure 3.14. During the 2 hours of operation in UHV after the exposure test, the cathode current continued to decay. The experiment was repeated on another cathode with the same configuration. During this exposure the initial current was 22 μA with 75 V on the gate electrode and 500 V on the anode. The same results were obtained; during the 10 hr. at UHV that followed the second exposure, the current never recovered to the original value. The results of these experiments suggest that the tips were damaged from ion bombardment. Experiments conducted with anode voltages below 90 V also showed performance degradation due to sputtering; therefore, high-energy ions generated between the gate and anode electrodes are not responsible for

the tip sputtering observed. A model for estimating the E_{th} was developed by Yamamura et al.[67] This model was used to predict that the energy threshold for xenon ions sputtering a silicon target is 91 eV. Because damage was done to the cathode at anode and gate voltages below that value, the true threshold value must be lower than 91 eV.

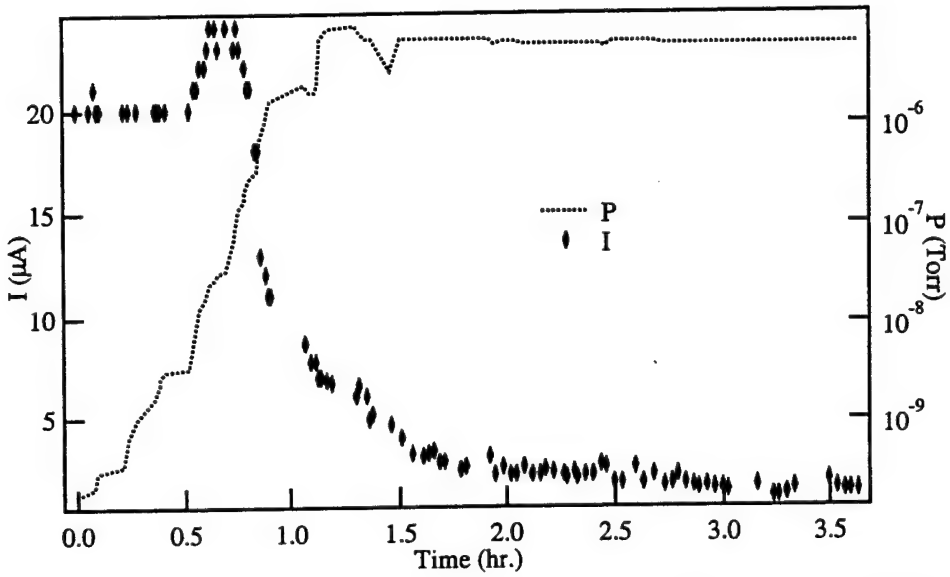

Figure 3.14 Si cathode current response to an increase in Xe pressure with V_g at 86 V and V_a at 400 V.

Experiments were then conducted at lower gate voltages to determine the xenon ion energy threshold for sputtering silicon. Irreversible performance degradation was observed during exposures to xenon at $2x10^{-5}$ Torr with gate voltages of 75 (V_a at 100 V), 70 (V_a at 70 V) and 60 V (V_a at 80 V). Typically, the current dropped in half during the first hour of the exposure. Data acquired from the xenon exposure experiment at $2x10^{-5}$ Torr with V_a and V_g at 70 V is shown in Figure 3.15. An initial increase in current was commonly observed when xenon was introduced. This response could be attributed to cleaning of the cathode by ion bombardment before the ions begin to damage the cathode. Cathode cleaning was observed in the FEM when carbide cathodes were exposed to argon during operation at LRI. With 50 V applied to the gate electrode no

performance degradation was observed during a one hour exposure to $2x10^{-5}$ Torr of xenon with 70 V applied to the anode; the current actually increased slightly. The results of this experiment are presented in Figure 3.16. During other experiments with MCNC cathodes, the current through the gate electrodes was usually less than a factor of 100 lower than the anode current. The efficiency of this cathode was poor; about 50% of the current was measured through the gate electrode. After the exposure, the emitted current increased while the efficiency decreased.

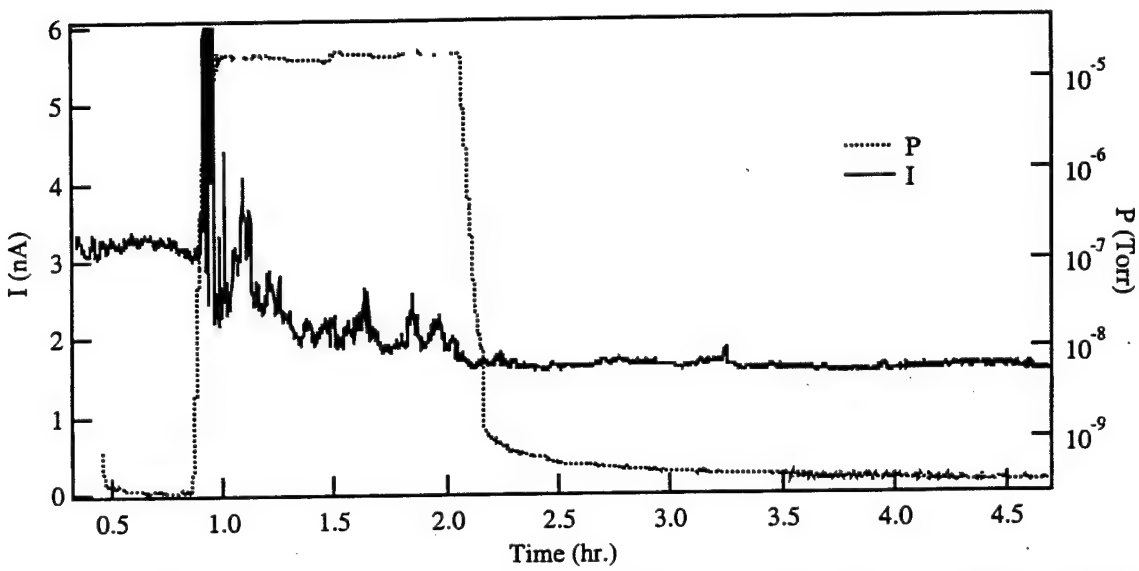

Figure 3.15 Si cathode current response to $2x10^{-5}$ Torr of Xe with V_g at 70 V and the V_a at 70 V.

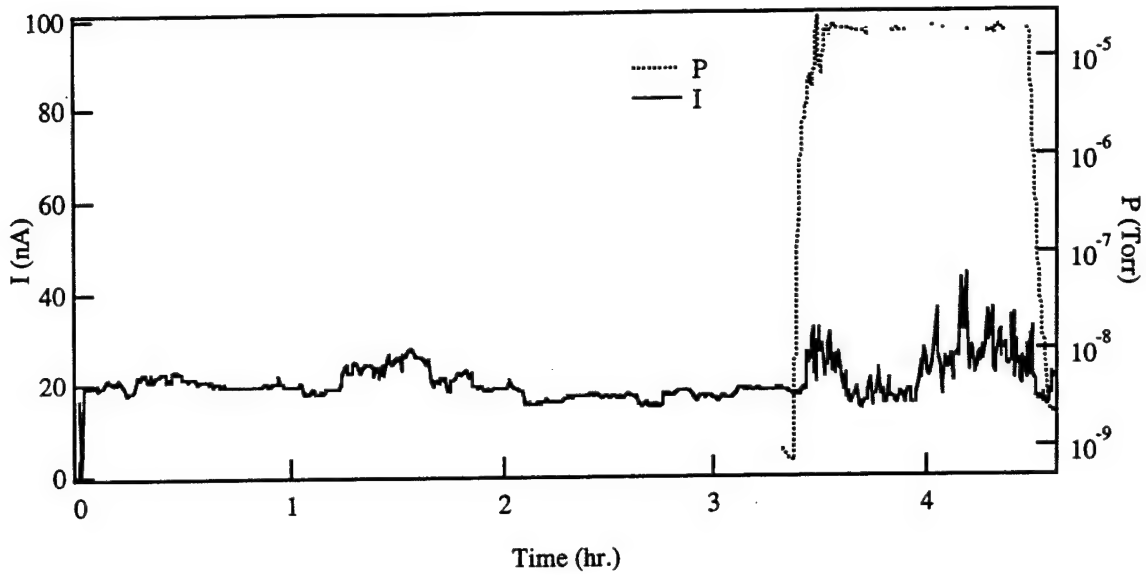

Figure 3.16 MCNC Si cathode current response to a 1 hour Xe exposure with V_g at 50 V and V_a at 70 V.

These MCNC cathodes operated for several hours without catastrophic arcing in xenon environments. The results of these experiments showed that xenon adsorption does not change the cathode work function. Performance degradation occurred in xenon environments as a result of the microtip structure being sputtered by ion bombardment. Experimental results showed that when the cathodes were operated at low enough voltages, ~50 V, ion energies were not high enough to cause significant sputter damage in one hour. Silicon cathodes emitting 100 mA at 50 V should satisfy current and lifetime limitation requirements necessary for the successful integration of Hall thruster and FE cathode technologies. A current of 2.5 μA has been measured from a single Si microtip structure with the gate voltage at 25 V.[68] Therefore, an array of less than 100,000 tips could provide100 mA of current to a Hall thruster if 2.5 μA/tip can be extracted from the array at 25 V.

3.2.4 Mo FEA Cathode Experimental Methods and Results

The first experiments, conducted on the Mo cathode from SRI International with 50,000 tips, investigated the effect of xenon adsorption on the work function of the cathode. The cathode was exposed to $2x10^{-4}$ Torr of xenon for one hour to provide a dose of xenon to the surface of the cathode greater than it experienced during the exposure tests at $2x10^{-5}$ Torr with the cathode operating. I-V traces were taken at UHV immediately before and after the exposure; these data are shown in Figure 3.17. The I-V trace taken after the exposure showed slightly better performance than before the exposure. The results of this experiment suggest that the work function did not increase due to the adsorption of xenon or any contaminants in the xenon supply. Any performance degradation observed during xenon exposure can, therefore, be attributed to changes in the geometrical parameters of the cathode.

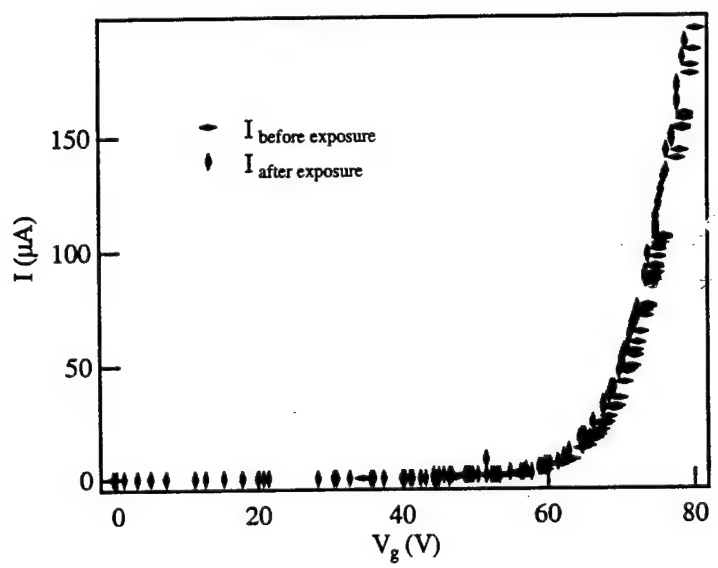

Figure 3.17 I-V data taken before and after the Mo cathode was exposed to xenon.

The next experiments focused on studying microtip sputtering by ion bombardment in xenon environments. A xenon exposure test, with operating conditions

similar to the operating conditions during experiments conducted at SRI International with a gate electrode voltage at 65 V and an anode voltage of 80V with ~18 μA for one hour in $2x10^{-6}$ Torr. Figure 3.18 shows the current response to the increase in xenon pressure. The current dropped to one-third of its original value in one hour. No current recovery was observed in 13 hours at UHV that followed the xenon exposure. The cathode was permanently damaged from ion bombardment.

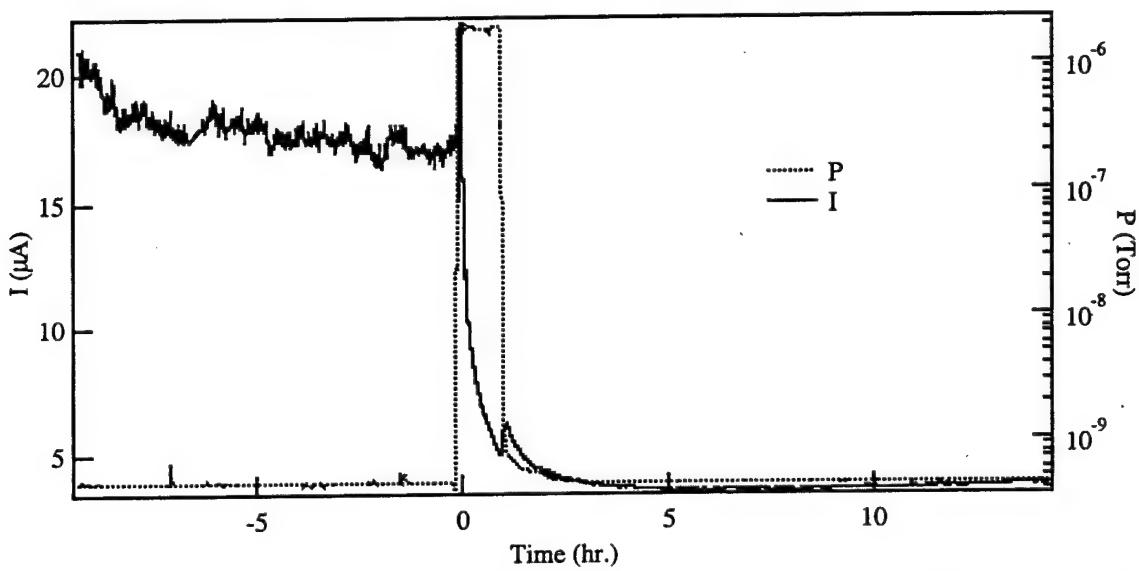

Figure 3.18 Mo cathode current response to $2x10^{-6}$ Torr of xenon with V_g at 65.6 V and V_a at 80 V.

An experiment was conducted to determine the gate voltage that corresponded to the onset of cathode sputter damage. The anode voltage in this experiment was 100 V, and the xenon pressure was $2x10^{-5}$ Torr. The gate voltage was increased in 1 V increments every 10 minutes, starting at 50 V. Performance decay caused by tip sputtering was observed within 10 minutes when the gate voltage reached 58 V, as shown in Figure 3.19. With further increases in gate electrode voltage, the current initially increases and then decays before stabilizing. Preliminary experiments showed that a few minutes are required for stabilization after the changes in gate electrode voltage. Figure

3.20 shows the current response to increases in gate electrode voltage in both UHV and 10^{-5} Torr xenon environments. This cathode had already been exposed to xenon environments for several hours and had suffered significant sputter damage before this experiment. It is expected that other cathodes will respond somewhat differently. A cathode with sharper tips and the same number of emitting tips, should show performance decay within ten minutes at even lower gate voltages, because the energy of the ions bombarding the emitting area of the tips will be slightly higher for sharper tips. This effect is a result of the higher electric fields at the tips. The maximum energy of the ions bombarding the emitting area of the tips slightly increases with decreasing tip radius, as will be shown in the following section.

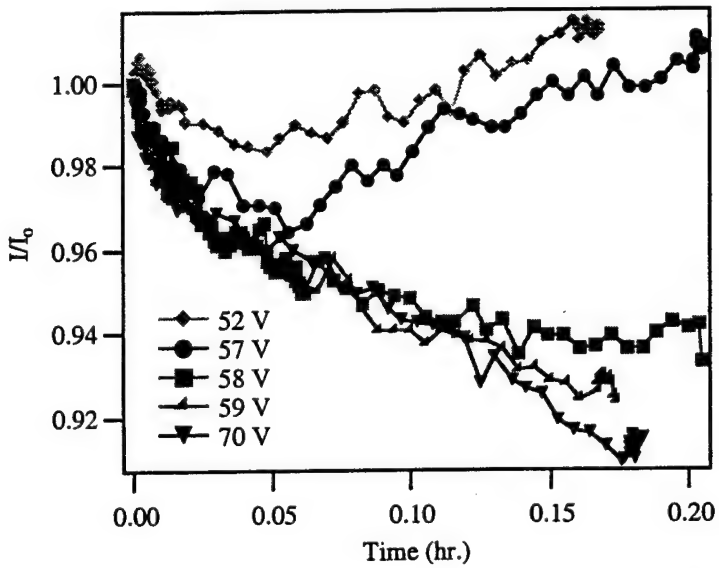

Figure 3.19 The Mo cathode current response to increasing gate electrode voltage with V_a at 100 V, $2x10^{-5}$ Torr of Xe.

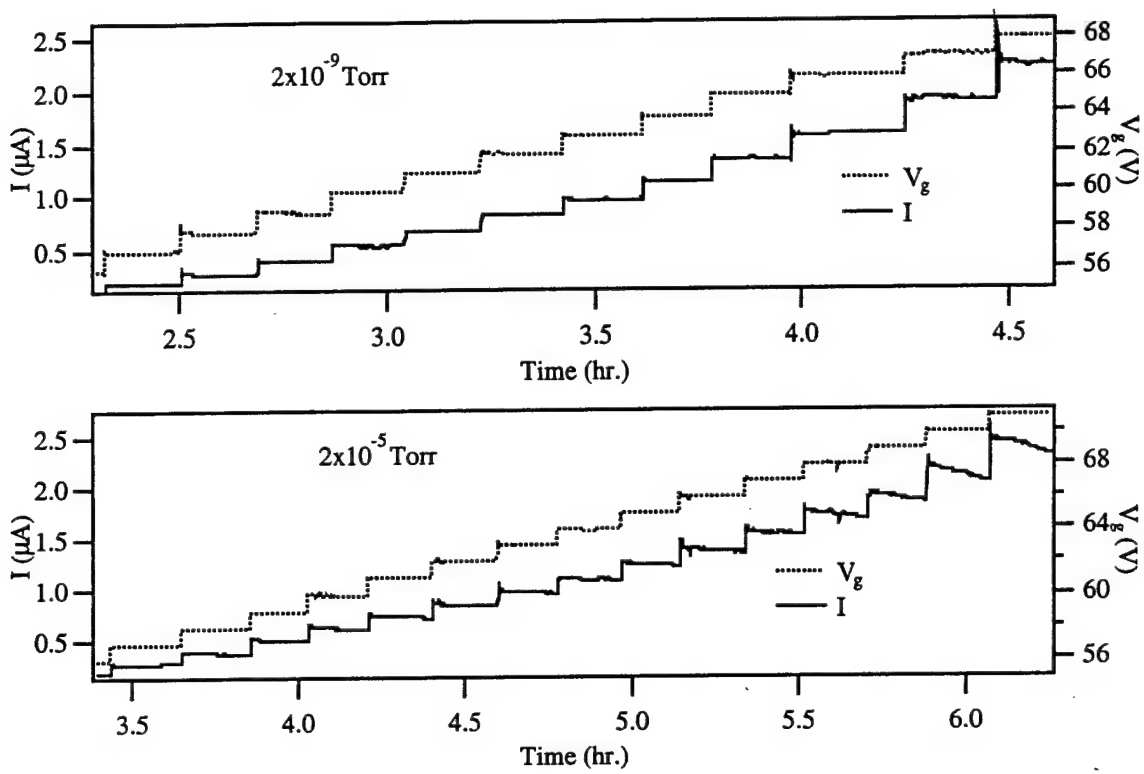

Figure 3.20 A comparison of the Mo cathode current response to increasing gate electrode voltage in $2x10^{-9}$ Torr and $2x10^{-5}$ Torr of Xe.

Several experiments were conducted with the gate voltage at 50 V. The maximum ion energy in this configuration is 46 eV, as predicted by the models discussed in the next chapter. In an experiment with the pressure at $2x10^{-5}$ Torr that lasted for 5 hours with the gate voltage at 50 V and the anode voltage at 60 V, the current initially increased and then decayed monotonically. The results of this experiment are shown in Figure 3.21. These results imply that the E_{th} for Mo sputtering by Xe ions is below 46 eV. Another experiment was conducted at the same pressure with V_g at 50 V to study the effect of increasing anode voltage. It was anticipated that at a high enough anode voltage the current would begin to decay. The current dropped from 110 nA to 85 nA in response to the initial increase in Xe pressure up to $2x10^{-5}$ Torr, and then increased with increasing anode voltage from 60 V up to 130 V in 10 V increments every 10 min. The results from this experiment are shown in Figure 3.22. They show that increasing the anode voltage

from V_a=V_g with V_g~E_{th} can actually improve the performance of the cathode. In an experiment at the same pressure with V_g at 50 V and V_a at 100 V, the current only increased during a two hour xenon exposure test with constant voltages. These results are shown in Figure 3.23.

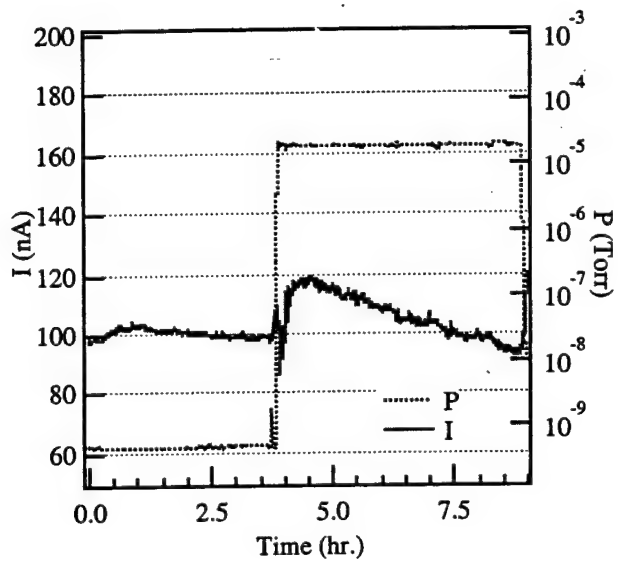

Figure 3.21 Mo cathode current response to a Xe pressure increase up to $2x10^{-5}$ Torr of xenon for 5 hours with V_g at 50 V and V_a at 60 V.

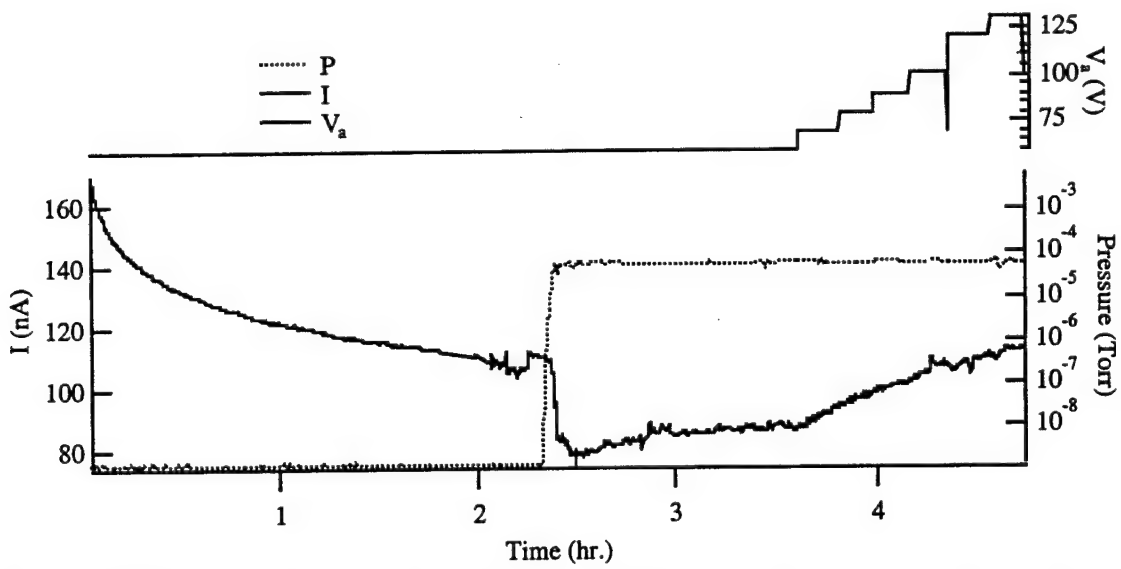

Figure 3.22 Mo cathode current response to a Xe pressure increase up to $2x10^{-5}$ Torr with varying V_a and V_g at 50 V.

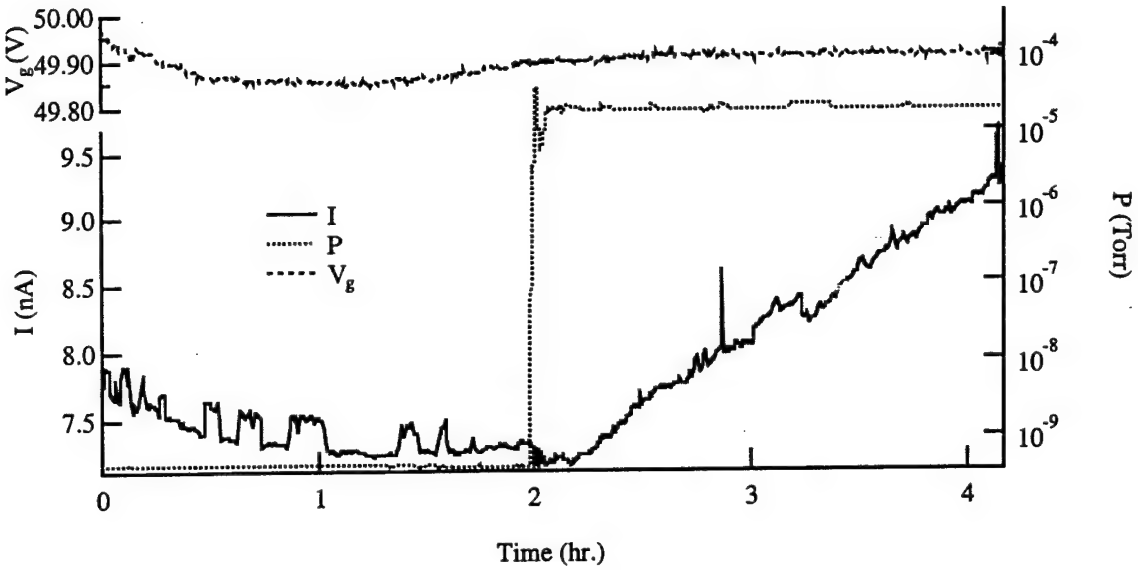

Figure 3.23 Mo cathode current response to a Xe pressure increase up to $2x10^{-5}$ Torr for 2 hours with V_g at 50 V and V_a at 100 V.

The performance improvements observed at low gate voltages and increasing anode voltage could be attributed to increases in the electric field at the cathode tips from changes in the tip microstructure. An increase in anode voltage to increase the electric field at the tip would result in an initial increase before the current equilibrates; equilibration typically required less ~5 min. During exposures with ~100 V applied to the anode and 50 V applied to the gate electrode, the current continually increased. If the increase in anode voltage increased the energy of the ions bombarding the emitting area of the tips, a current decay would be observed because the r_t would increase from sputtering. However, not only is the emitting area being sputtered, the cone sidewalls are also being sputtered by ion bombardment. While the emitting area is being bombarded with ions primarily at a normal incidence to the surface, the cone sidewalls are also being bombarded by ions at smaller angles. Sputter yields increase with decreasing incident ion angle from 90° to 60°. With a uniform flux of ions to the cone surface, the sidewalls will sputter faster to decrease the half-cone angle and increase the current at a constant

voltage. As the anode voltage increases, ion acceleration into the cathode tip is less focused on the cathode emitting area and more ions hit the cathode sidewalls where the sputter yield is higher. Cathode sputtering by ion bombardment is discussed in more detail in the following chapter.

The SRI cathode survived for 21 hours in $2x10^{-6}$-$2x10^{-5}$ Torr of xenon without catastrophically arcing. The cathode performance degraded during the xenon exposures because the cathodes were sputtered by ion bombardment. The results of the xenon exposure experiments showed that xenon adsorption does not change the cathode work function. They also showed that it is possible to avoid sputter damage while operating in xenon environments if operating voltages are low enough. The experimental results showed that the gate voltage should be below 50 V to avoid sputter damaging the emitting areas of the tips. It was learned that anode voltage does affect cathode performance in xenon environments. Increasing the anode voltage up to 100 V with the gate electrode ~50 V improved the cathode performance, possibly by reducing cone half-angles or sharpening the emitting cones. However, operating with the anode voltage at 100 V is not favored because the material sputtered off of the cone sidewalls will then redeposit on the insulator walls, eventually shorting the tips and gate electrodes.

3.3 Carbon Film FE Cathode Experiments

A carbon film cathode from FEPET was used to determine the effect of xenon ion bombardment on field emission cathodes with thin films instead of microtip structures. These cathodes have low electron affinity and require lower macroscopic field strengths than FEA cathodes. Electron emission from the carbon films is not as sensitive to ion bombardment as microtip structures. The current emitted by the microtip structures is exponentially sensitive to changes in tip radius from sputtering by ion bombardment. Limited sputtering of carbon film may not affect the emission current; these cathodes can

withstand more sputter damage without performance degradation. Carbon film cathodes are more sensitive to chemical changes in the surface of the film; inert gas environments should not affect the surface chemistry.

Carbon film cathodes can tolerate much higher pressure environments than micro tip cathodes when operating, and can operate more safely at much higher voltages. The disadvantages to using currently available carbon film cathodes are the high gate electrode voltages required and low operating efficiency. The FEPET cathode is not a microintegrated structure like the microtip cathodes. Gate voltages of several hundred volts are required for microamperes of current. Low cathode efficiency is also a concern; the gate electrode collects up to 80% of the current. Large improvements in the cathode efficiency are expected when a microintegrated film and gate structure is fabricated.

In this investigation, the focus of the experiments with a FEPET cathode was on the response of the current to increases in xenon pressure up to $2x10^{-6}$ Torr. The pressure was only increased to $2x10^{-6}$ Torr of xenon because of the close proximity of the ionization gauge and anode and the high anode voltage at 900 V. Charged particles were created in this configuration with high pressures and were collected by the electrodes at a much higher rate than the electrons emitted by the cathode, making it impossible to measure the emitted electron current. With high operating voltages required by this cathode, the rate of xenon ion bombardment will be much higher than the cathode will experience in the thruster environment where operating voltages will be much lower. Therefore, any positive results in these experiments are extremely promising.

3.3.1 Carbon Film FE Cathode

The carbon film cathode used in this investigation was fabricated at Field Emission Picture Element Technology (FEPET). The FEPET graphitic and amorphous carbon films are grown on a ceramic substrate by hot filament chemical vapor deposition

(HFCVD). The ceramic substrate is specially treated to improve the emission properties of the film with a proprietary substance. Deposition of this substance can be controlled when a special emission pattern or emitting area is required. A hydrogen and methane gaseous mixture is introduced in a reactor chamber which is activated by hot filaments. Activated species are then deposited on the substrate surface. The filament and substrate temperatures, gas flow rate, and gas consumption are carefully controlled to obtain films with good emission properties. Post-growth processing is not required.

The cathode used in these experiments consisted of a thin carbon film deposited on a ceramic substrate with a stainless steel extraction grid spaced 100 μm from the cathode. The size of the emitting area of the cathode is 0.25 cm^2. The cathode is mounted on a glass stem as shown in Figure 3.24.

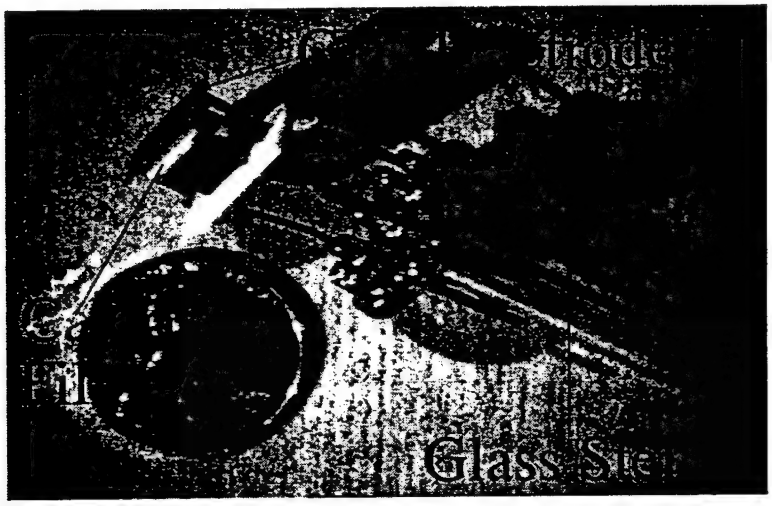

Figure 3.24 A FEPET carbon film cathode on a glass stem.

3.3.2 Experimental Apparatus

The experimental apparatus is described in section 3.2.2. The electrical configuration is shown in Figure 3.12. Note: This figure shows a cathode with a tip

structure, however, the FEPET cathode does not use an emitting cone structure; the emitting surface is a thin film.

3.3.3 Experimental Methods and Results

The efficiency of this film cathode is much lower than the Spindt-type cathodes. The gate electrode intercepts the majority of the current. About 20 % of the current emitted from the carbon film was typically collected at the anode during these experiments; however, the efficiency was often much higher at currents below 200 nA. The performance of the FEPET cathode used in these experiments in UHV is shown in Figure 3.25.

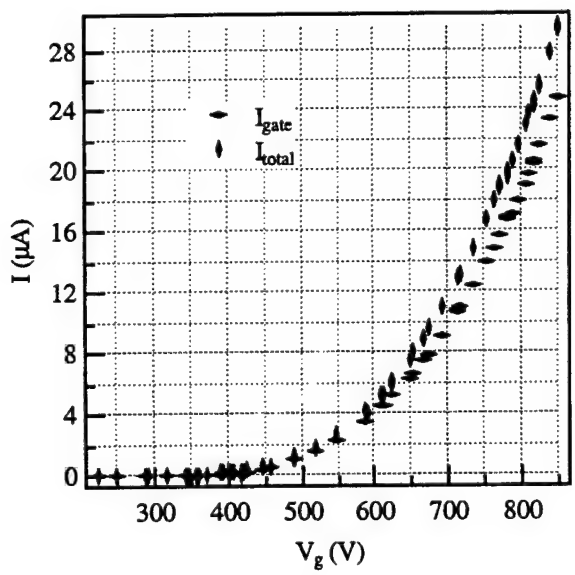

Figure 3.25 I-V traces showing the performance of a FEPET carbon film cathode in a UHV environment.

The cathode demonstrated impressively stable performance in the xenon environment as shown in Figure 3.26. This figure also shows that fluctuations in the current can be attributed to gate voltage fluctuations. Operation of the ionization gauge caused the gate electrode voltage to fluctuate between 835 V and 850 V. This caused 2

μA fluctuations in the emitted current. In the high pressure environments, the ionization gauge affected the current measurements on all of the electrodes. The ionization gauge was responsible for ~250 μA to the anode and 15 μA to the gate electrode. With a 1 MΩ resistor on the gate electrode, this increase in current changed the gate voltage by 15 V. The ionization gauge was turned off and on several times during the high pressure exposure experiments to record the pressure. The large jumps in the gate voltage, and responding current can be attributed to the ionization gauge current. The results of these experiments show that, even at such high electrode voltages, the cathode performance is not affected by ion bombardment and sputtering of the carbon film during ~10 hours. Two of these exposure test were conducted at the same operating conditions. The first exposure test lasted for 4 hours, and the second exposure lasted for 3 hours. No performance degradation was observed during either of the experiments. I-V data taken before and after 4 hours of xenon exposure were identical, as shown in Figure 3.27. These data also show that the cathode was not damaged during the exposures.

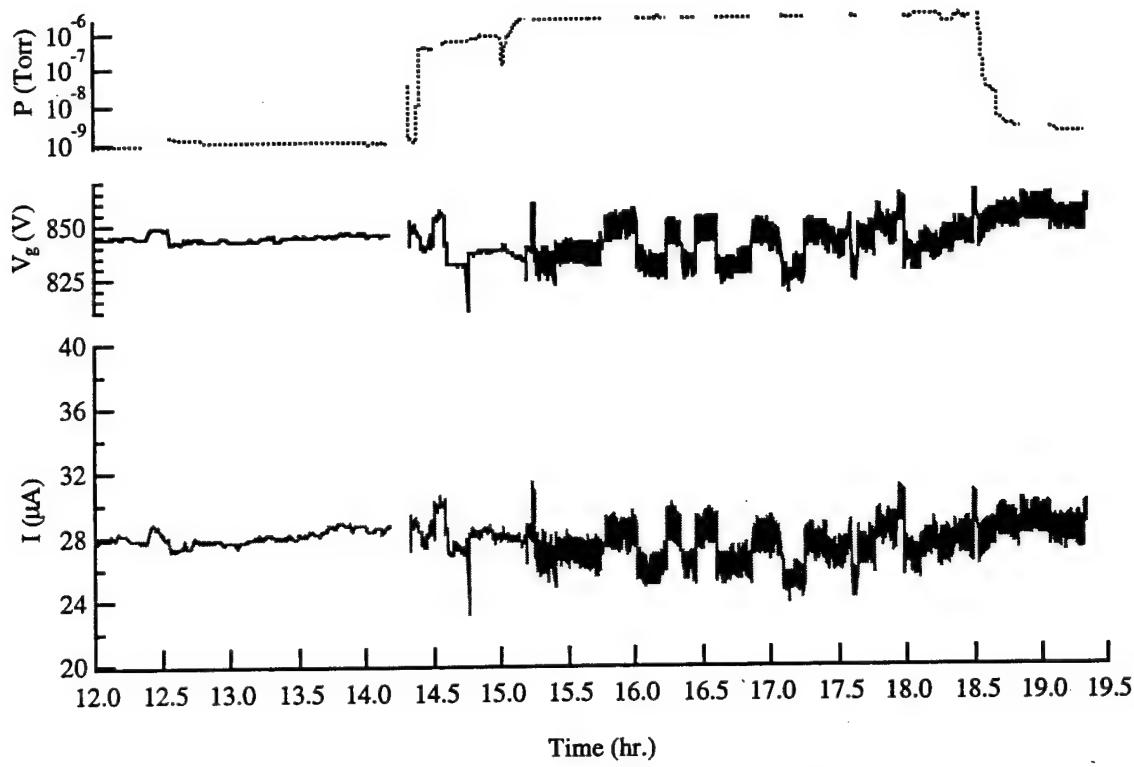

Figure 3.26 The cathode current response to increasing the Xe pressure up to $2x10^{-6}$ Torr for 4 hours. The anode potential was 900 V above the potential of the carbon film.

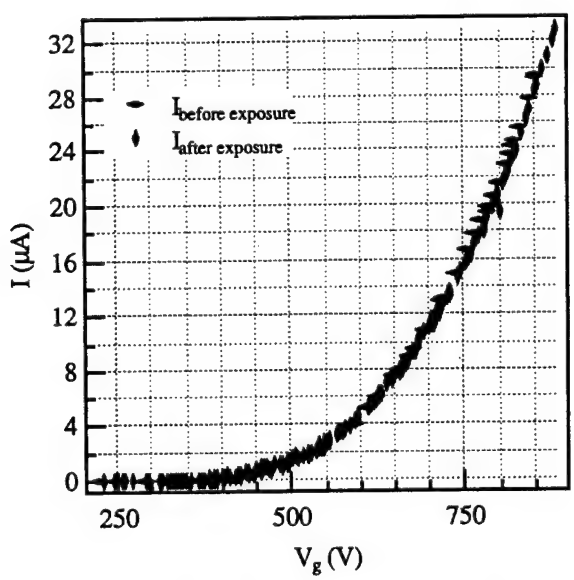

Figure 3.27 I-V curves taken in UHV before and after the carbon film cathode was exposed to xenon.

Figure 3.28 shows I-V data taken in UHV and xenon environments. The xenon pressure was increased to $2x10^{-6}$ Torr and stabilized while the cathode was off. The cathode was then slowly turned on in the xenon environment for ~8 min. and then slowly reduced to zero current to obtain two of the data sets shown in Figure 3.28. The cathode start-up in $2x10^{-6}$ Torr was no different from the start-up in UHV environment. This experiment was repeated with the same results. This characteristic of the cathode is extremely valuable because the base pressure of the facilities used in Hall thruster testing is ~10^{-7}-10^{-6} Torr; therefore cathodes must comfortably start-up in this environment.

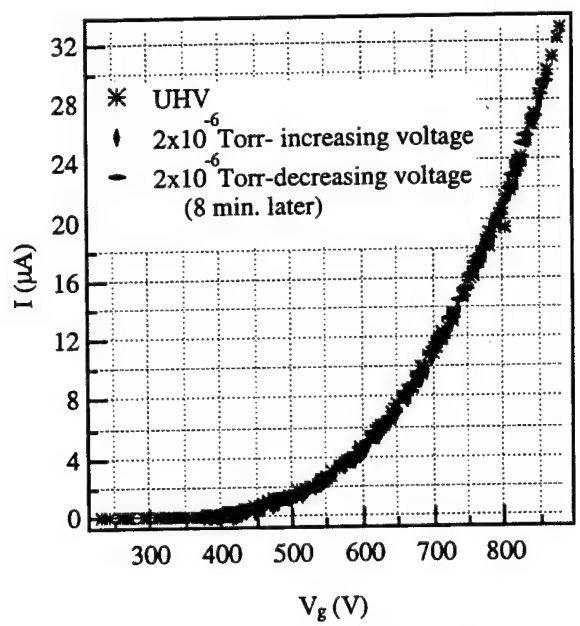

Figure 3.28 Carbon film cathode turn-on and turn-off I-V curves with an anode voltage of 900 V in $2x10^{-6}$ Torr of xenon compared to turn-on I-V data in UHV.

The FEPET FE cathode was operated for a total of 9 hours in $2x10^{-6}$ Torr xenon environment with 850 V on the gate electrode and 900 V on the anode to get ~28 μA of emission current. During this time, the cathode showed no performance degradation from the intense ion bombardment. The operating voltages and efficiency of this cathode must be significantly improved before this cathode can be used with ion and Hall

thrusters; however it is believed that these objectives can be achieved with a microfabricated integrated gate and carbon film structure. At the current state of FEPET carbon film technology, this cathode presents itself as a strong candidate for ion beam neutralization with FEEP systems, which consume approximately 1/4 W for 1 mA at 10 kV ion accelerating potentials.

CHAPTER 4

MICROTIP CATHODE PERFORMANCE MODELING

4.1 FEA Cathode Performance Degradation Model

To expedite FEA cathode development for EP systems and reduce development costs, a FEA cathode performance decay model was used in conjunction with experimentation. A different model must be developed to predict the effect of a plasma thruster environment on the performance of thin film cathodes. The model discussed in this chapter incorporates 3 previously existing models with slight modifications which predict cathode emission currents, flux of ions to the surface, and sputter yields of cathode materials by xenon ions, and an additional model to predict changes in tip radius from ion bombardment. With these models and experimental results, the lifetime of Si and Mo FEA cathodes can be predicted in xenon environments of electric propulsion systems.

A flow diagram for this performance degradation model is shown in Figure 1.7. The inputs to this model are I-V data obtained in UHV, cathode work function, half-cone angle of the microtip structures, β_c, the energy threshold for sputtering cathode material by ion bombardment, E_{th}, gate aperture diameters, r_g, and number of tips, N_{tips}. The I-V data are used in a model developed by Jensen to estimate the effective tip radius, r_t, and distribution of radii in the array.[69] The Jensen model is also used to determine the emission current from an array. To determine current changes in time caused by changes

in tip radius, the change in tip radius in time must be determined. The rate at which the tip radius increases in time is approximated by

Eqn. 4.1
$$\frac{dr_t}{dt} = \frac{d}{t_e},$$

where the atomic spacing in the material is d (Å), and a monolayer of material is removed from the tip emitting area with an effective tip radius, r_t, in t_e (s). A model developed by Brodie was used to determine t_e. Material sputter yields were determined using the model developed by Yamamura et al.[67] The tip radius increases in time are approximated by assuming that each layer removed from the emitting area of the tip increases the tip radius by the atomic spacing in the tip material. Tip radii are represented statistically by an effective tip radius and spread in tip radius across an array, Δs. The radius of the sharpest tips in the array will change at the fastest rate so that the uniformity in the array improves in time. The changes in the spread in tip radii, in time, shown in Eqn. 4.2, is a function of the change in effective tip radius in time and the maximum tip radius in the array. I(r(t),Δs(t)) can then be determined using Jensen's emission model for FEA cathodes.

Eqn. 4.2
$$\Delta s(t) = \frac{r_{t\,\max}}{r_t(t)} - 1.$$

The following three sections of this chapter present the details of the Jensen model to predict cathode parameters from I-V data and cathode emission current, the Brodie model to predict the removal rate of material from the tip emission area, and the model developed by Yamamura et al.[67] which predicts the sputter yields of xenon ions bombarding Si and Mo targets.

4.1.1 Field Electron Emission Model

The analytical and statistical model used to predict the emission current from a field emission tip and gate electrode structure as shown in Figure 1.5, was developed by

Jensen[69]. The model is described in much more detail in another article.[69] The emission model takes a statistical approach to estimating the current emitted by field emission cathodes because the emitting area of a tip, current distribution in that area, number of tips contributing to the measured current, and current per tip are impossible to determine exactly for any FEA cathode. Work function, tip radius, emission cone half-angle, and cone structure half-angle assume a range of values in a field emission array cathode. Because each tip is processed in parallel and exposed to the same environments, the cone structure half-angles and work functions for the all of the tips in the array should be very similar. The experimental results discussed in the previous chapter showed that the emitting area of the tip depends on the cleanliness of the tip and its radius of curvature. Other studies have shown that field emission from a cathode can originate from protrusions of atomic dimensions, even on a cone structure with a radius of curvature of several nanometers.[70] Emission from a cathode microtip is not uniform within the emitting area as shown in the previous chapter. The emitting area of tips in an array is then best represented statistically by an effective tip radius and distribution of tip radii in the array of emitters. These parameters can be determined from experimentally acquired I-V data and the Jensen FE current model. It has been successfully used to model the performance of Si and Mo FE cathodes.[71]

Jensen's model represents the tip with a hyperbolic shape; the field (V/Å) at the apex of the tip can then be approximated by

Eqn. 4.3
$$F_{tip} \approx \beta_g V_g,$$

where V_g is the voltage on the gate electrode with respect to the emitting cone. The electric field at the tip surface increases with decreasing tip radius, r_t, and half-cone angle, β_c, by the field enhancement factor, β_g(1/Å),

Eqn. 4.4
$$\beta_g \approx \left(\frac{\pi}{\ln\left(kr_g / r_t\right)} - \tan^2 \beta_c \right) \frac{1}{r_t}, \text{ and}$$

Eqn. 4.5 $$k \approx \frac{1}{54}\left(86+\frac{r_g}{r_t}\right)\cot(\beta_c).$$

With these relationships, F_{tip} (eV/Å) can be approximated with an analytical expression. The current density is approximated by the Fowler-Nordheim (F-N) equation for emission current density J_{FN}(e/fs-Å^2),[20,21]

Eqn. 4.6 $$J_{FN}(F) = a_{fn}F^2\exp(-b_{fn}/F),$$

where the Fowler-Nordheim coefficients, b_{fn}(eV/Å) and a_{fn}(e/ eV^{2}fs), are given in atomic units, by

Eqn. 4.7 $$b_{fn} = 0.642\phi^{3/2} \text{and}$$

Eqn. 4.8 $$a_{fn} = (116\phi)^{-1}\exp\left(14.3994 b_{fn}/\phi^2\right).$$

When the current density is integrated over the surface of the emitter, the tip current in microamperes can then be determined by

Eqn. 4.9 $$I_{tip}(V_g) = b_{area}J_{FN}\left(F_{tip}\right).$$

The area factor, b_{area}(Å^2), is the ratio between the current from the tip and the current density on-axis, and depends upon the magnitude of the gate voltage as

Eqn. 4.10 $$b_{area} = 2\pi r_t^2\cos^2(\beta_c)\left(\frac{F_{tip}}{b_{fn}+\sin^2(\beta_c)F_{tip}}\right).$$

The current emitted from an array of tips can be defined by

Eqn. 4.11 $$I_{array}\left(V_g\right) = N_{tips}\sum\left(\Delta s, V_g\right)b_{area}\left(V_g\right)J_{FN}\left(F_{tip}\left(V_g\right)\right),$$

where Σ is the distribution factor associated with a spread in tip radii, Δs. The tip radii are distributed according to $r(s)=r_t(1+s)$, where $0 \le s \le \Delta s$. For a single tip emitting, $\Delta s=0$. However, this value governs the distribution of tip radii with N_{tips}, and therefore accounts for the non-uniformity of an array. The field for a tip of radius $r(s)=r_t(1+s)$ is then $F(s) \approx (1+c_o s)F(0)$, where $F(0)=F_{tip}$, and

Eqn. 4.12 $$c_o = \frac{1}{\pi\beta_g r_t}\left(\tan^2(\beta_c)+\beta_g r_t\right)^2 - 1.$$

The natural log of $I_{tip}(s)/I_{tip}(0)$ is approximated as a linear function in s and results in

Eqn. 4.13 $$\sum(\Delta s, V_g) = \frac{\exp(\Delta s b) - 1}{\Delta s b};$$

Eqn. 4.14 $$b = \frac{c_o b_{fn} + (3c_o + 2)\beta_g V_g}{\beta_g V_g} - \frac{c_o \beta_g V_g}{b_{fn}} \tan^2(\beta_c).$$

Invoking a Legendre least square analysis on

Eqn. 4.15 $$I_{array} \cong A_{FN} V_g^2 \exp\left(\frac{-B_{FN}}{V_g}\right),$$

B_{FN} and A_{FN} are

Eqn. 4.16 $$B_{FN} = \frac{b_{FN}}{\beta_g} + \frac{\delta^2 + 2x_o}{x_o^3}, \text{ and}$$

Eqn. 4.17 $$A_{FN} = N_{tips} 2\pi r_t^2 \cos^2(\beta_c) a_{fn} \frac{\beta_g^3}{x_o b_{fn}} \exp\left(2 + \frac{4}{3}\frac{\delta^2}{x_o^2}\right) \sum(\Delta s, x_o^{-1}), \text{ where}$$

Eqn. 4.18 $$\delta = \frac{V_{rf}}{V_{pk}(V_{pk} - 2V_{rf})},$$

Eqn. 4.19 $$x_o = \frac{V_{pk} - V_{rf}}{V_{pk}(V_{pk} - 2V_{rf})}, \text{ and}$$

Eqn. 4.20 $$V_{rf} = \frac{V_{max} - V_{min}}{2}.$$

Experimental data are used to estimate r_t and Δs. If I-V data are presented on a Fowler-Nordheim plot ($\ln(I/V^2)$ vs. $1/V$), $A_{FN}(A/V^2)$ is the y-intercept and $B_{FN}(V)$ is the slope of the curve. From these parameters and an estimated work function, effective tip radius, r_t, and distribution parameter, Δs, can be determined. Once the effective tip radius and spread in tip radius throughout the array of emitters are known, the current from the array can be calculated. The radius distribution parameter, Δs, represents the spread in tip radii. In an array, $\Delta s = r_{tmax}/r_t - 1$, where $r_{tmax} = r_t(1+\Delta s)$ is the maximum radius and r_t is the minimum radius. During exposure to xenon environments, the performance

of the sharpest tips will degrade the fastest as dr/dt will be highest for those tips. Sputtering of the cathode tips will decrease the spread in tip radii to improve the uniformity of the array. It is assumed that r_{tmax} is constant during the exposure and that Δs changes in time with Xe exposure as r_t changes, as Eqn. 4.2 shows. The change in effective tip radius in time depends on the removal rate of material from the tip emission area. The time required to remove a monolayer of material from the tip emission area is determined using the tip sputtering model discussed in the next section.

4.1.2 Tip Sputtering Model

Brodie developed the field emission cathode tip sputtering model described in this section.[72] It is described in more detail in another article.[72] This model is capable of estimating sputter rates of microtips by ions generated by the emitted electrons. It is used here to estimate the change in tip radius in time when operating in xenon environments. Brodie used average sputter yield and ionization cross-sections in his calculations for high operating voltages, >100 V. This study is primarily investigating low voltage operation where ion and electron energies are low and ionization cross-sections, Q, and sputter yields, Y, are exponentially dependant on ion and electron energies. Accurate sputter yield and ionization cross sections are very important to these calculations; therefore, average values were not used in the calculations of the removal rate of material from the emission area of the tips, n_s. The time, t_e, required to erode a single layer of atoms from the emission area is given by

Eqn. 4.21
$$t_e = \frac{2\pi r_t^2 (1-\cos\sigma)}{d^2 n_s},$$

where d=0.416 nm for the atomic spacing of evaporated molybdenum, d=0.313 nm for silicon. The removal rate of material from the tip emitting area is n_s(atoms/s). The emission half-cone angle is σ; it is estimated as 37° in this model. The half-cone emission angle varies significantly for tips in an array. Experimental results discussed in

the previous chapter showed that this value ranged from 8° to 44° for eight carbide tips with an average value of 28°. Gomer claims that the current density drops to approximately 10% of the value on axis by 45° off axis.[19] A half-cone emission angle of 37° is used because it significantly simplifies the mathematics of the sputter rate calculations and is a reasonable estimate to represent tip half-cone emission angle in an array.

The removal rate of material from the tip emitting area depends on the flux of ions, energy of the ions, and the dependence of material sputter yields on ion energy. The number of ions striking the emitting area per second, n, is given by

Eqn. 4.22
$$n = \int_{r_t}^{r_m} \frac{I_e}{e} N Q_i(V_r) dr,$$

and the number of atoms sputtered from the emitting area per second, n_s, is given by

Eqn. 4.23
$$n_s = \int_{r_t}^{r_m} \frac{I_e}{e} N Q_i(V_r) Y(V_r) dr,$$

where the field emitted electron current is I_e and the number of molecules per cm^3 in the chamber is $N = 3.55 \times 10^{16} P$ molecules/cm^3 (P is the pressure in Torr at room temperature). The cross-section for ionization of gas molecules by electrons of energy eV_r is $Q(V_r)$. The sputter yield in atoms per ion of energy eV_r is $Y(V_r)$.

In this cathode sputtering model, the cathode configuration is approximated as an isolated sphere of radius r_t at ground potential, as shown in Figure 4.1, and the gate electrode as a concentric sphere with radius r_g. The radial potential distribution on the axis of the tip is V_r, and can be approximated by

Eqn. 4.24
$$\frac{V_r}{V_g} = \left(\frac{r_t}{r} - 1\right)\left(\frac{r_t}{r_g} - 1\right)^{-1}.$$

This simple concentric spheres model gives remarkably good results compared to exact predictions obtained by computer solutions of Laplace's equation and geometric

boundary conditions because close to the emitting area of the tip, the field lines are radial and fall off inversely as the square of the distance.[73] The Jensen model more accurately predicts the electric field at the tip surface, which is more important when calculating the field emission current from a tip. However, the Brodie model is sufficient for predictions of the potential distribution near the tip to determine ion production near the cathode. For this analysis, the electric field and current over the emitting area of the tip are assumed to be uniform.

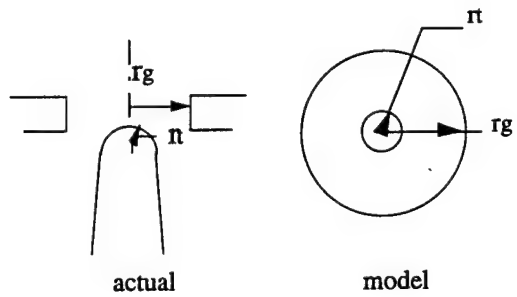

Figure 4.1 The actual cathode configuration, and the configuration used in the microtip sputtering model to predict the potential field near the microtip and electric field at the microtip.

The ion flux to the tip depends on the local gas temperature and the positions at which ionization occurs. If an ion is formed with initial cross radial velocity, v_t, corresponding to a temperature of V_t(eV), then only the ions formed within a radial distance r_m, will strike the emitting area of the tip, where

Eqn. 4.25
$$r_m = r_t\left(\frac{V_g}{V_t}\right)^{\frac{1}{3}}.$$

Usually the ion temperature is estimated to be 0.03 eV, which assumes that the ions are in equilibrium with their surrounding vacuum chamber walls with the same temperature as the neutral particles. If a higher temperature of ions is assumed, the flux of ions to the

emitting area of the tips will decrease. Therefore the assumption that V_t=0.03 eV will provide an upper limit on dr_t/dt.

The significant radial positions used in this model are shown in Figure 4.2. The radial position at which the energy of the emitted electrons reaches the threshold of ionization ($V_r(r_i)$ = Vi = ionization threshold) is r_i. The radial position from which an ion, if formed, gathers sufficient energy to reach the threshold for sputtering when it strikes the tip surface ($V_r(r_s)$ = Vs = sputtering threshold) is r_s. The radial position beyond which the average ion formed will not strike the emitting area of the tip is r_m.

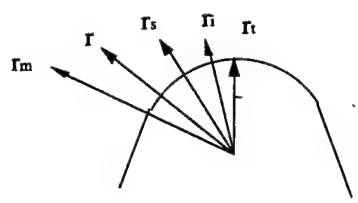

Figure 4.2 Significant radial positions used in the model of microtip sputtering.

The calculations made by Brodie employed average values of V_r and then used corresponding Q and Y values. In this study, data curves and interpolation were used to estimate these parameters because these parameters are exponentially sensitive to ion and electron energies in the energy range relevant in this investigation. The integral for n_s was then evaluated numerically for hundreds of points. Ionization cross-sections from Brown[74] used in the calculations are shown in Figure 4.3. Interpolation was used to determine values between data points. Sputter rates for xenon ions on molybdenum and silicon targets were used in the model because the thruster environment is primarily xenon. The relationship between sputter yield and ion energy is discussed in the next section.

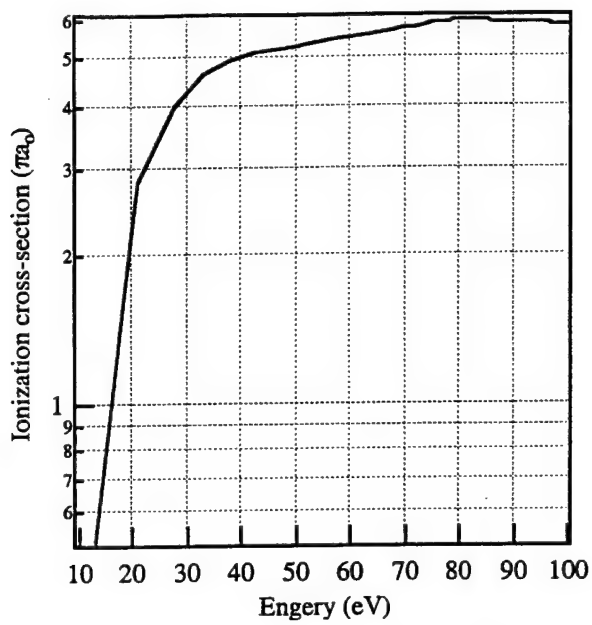

Figure 4.3 Xe ionization cross-sections, Q_i, from Brown.[74]

4.1.3 Sputter Yield Model

Sputter yield and energy threshold values used in this study for xenon ions bombarding molybdenum and silicon targets with a zero degree angle of incidence were calculated using a model developed by Yamamura et al.[67] using fit parameters,Q, from Matsunami at al.[75] The electric field within r_m of the tip is primarily radial. Therefore the ion incidence angle can be approximated by zero. Because experimental data exist only above 100 eV ion energies, the accuracy of the model is unknown at energies below this level. The energy of ions bombarding the emitting area of the cathodes in the configurations of interest will primarily be below 100 eV.

In the model developed by Yamamura et al.[67], the sputter yield is defined as

Eqn. 4.26
$$Y(E) = 0.42\frac{\alpha Q K_1 s_n(\varepsilon)}{U_s[1+0.35U_s s_e(\varepsilon)]}\left[1-\left(\frac{E_{th}}{E}\right)^{\frac{1}{2}}\right]^{2.8},$$

and the energy threshold for sputtering is defined by,

Eqn. 4.27 $$E_{th} = \left(1.9 + 3.8\frac{M_I}{M_{II}} + 0.134\left(\frac{M_{II}}{M_I}\right)^{1.24}\right)U_s,$$

where the subscripts I and II refer to the incident and target particles, respectively. Q is an empirically derived parameter for a specific ion target combination, U_s(eV) is the sublimation energy of the target material, and E(eV) is the ion energy. Q values are presented for different ion target combinations by Matsunami at al.[75] Other parameters used in the model are

Eqn. 4.28 $$\alpha = 0.08 + 0.164\left(\frac{M_{II}}{M_I}\right)^{0.4} + 0.0145\left(\frac{M_{II}}{M_I}\right)^{1.29},$$

Eqn. 4.29 $$K_1 = 8.478\frac{Z_I Z_{II}}{\left(Z_I^{2/3} + Z_{II}^{2/3}\right)^{1/2}}\left(\frac{M_I}{M_I + M_{II}}\right),$$

Eqn. 4.30 $$\varepsilon = \frac{0.03255}{Z_I Z_{II}\left(Z_I^{2/3} + Z_{II}^{2/3}\right)^{1/2}}\left(\frac{M_{II}}{M_I + M_{II}}\right)E,$$

Eqn. 4.31 $$s_n(\varepsilon) = \frac{3.44\varepsilon^{1/2}\ln(\varepsilon + 2.718)}{1 + 6.355\varepsilon^{1/2} + \varepsilon\left(-1.708 + 6{,}882\varepsilon^{1/2}\right)},$$

Eqn. 4.32 $$S_e = k_2\varepsilon^{1/2}, \text{ and}$$

Eqn. 4.33 $$k_2 = 0.79\frac{\left(M_I + M_{II}\right)^{3/2}}{M_I^{3/2}M_{II}^{1/2}}\frac{Z_I^{2/3}Z_{II}^{1/2}}{\left(Z_I^{2/3} + Z_{II}^{2/3}\right)^{3/4}}.$$

The parameters used in this investigation for molybdenum and silicon targets bombarded by xenon ions are shown in Table 4.1.

Table 4.1 Ion and target material parameters used in the sputter yield model.

	Xe	Mo/MoXe	Si/SiXe
M	131.3	95.94	28.1
Z	54	42	14
U_s (eV)		6.82	4.63
Q		0.84	0.78
E_{th} (eV)		49	91

Table 4.1 shows E_{th} values predicted by the model for Mo and Si targets being bombarded by xenon ions. Other models predict even higher values for E_{th}[76], while some experimental measurements extrapolated to low energies yield E_{th} estimates for a Mo target and Xe ion combination that is 27 eV.[77] Experimental results presented in the previous chapter show that cathodes were damaged by ion bombardment when maximum ion energies were lower than the E_{th} values shown in Table 4.1. Also, these values for E_{th} led to great underestimates of dI/dt using the FEA cathode performance and sputtering models. To obtain better correlation between measured and theoretical dI/dt, lower E_{th} values were used in the models. These E_{th} values were more consistent with experimental results presented in the previous chapter and generated sputter yield curves that provided a better fit through measured sputter yield values at ion energies less than 300 eV. This section discusses the modeling results and comparisons to experimental results.

The model developed by Yamamura et al. was used to predict that the E_{th} values for xenon ions sputtering silicon and molybdenum targets are 91 eV and 49 eV, respectively. This model was also used to determine the relationship between ion energy and sputter yield; these relationships are shown in Figure 4.4 and Figure 4.5 for Mo and Si, respectively. The cathode sputtering model was used to estimate the maximum energy of the ions bombarding the emitting area of the tips, $E_{imax}(r_m)$, at any operating condition. Results from experiments during which cathodes were exposed to xenon while operating showed that MCNC Si cathodes were damaged when gate electrode voltages were at 85, 70, and 60 V (E_{imax} = ~55 eV). The cathode was not damaged during

1 hr. in $2x10^{-5}$ Torr of xenon with 50 V applied to the gate electrode (E_{imax} = ~46 eV). These results are preliminary because the experiments lasted only a few hours and some of them have not yet been repeated; however, they suggest that the E_{th} for sputtering of Si by xenon ions is below 55 eV. When the experimental results are combined with results of the performance model discussed in this chapter, a better estimate of the E_{th} can be obtained.

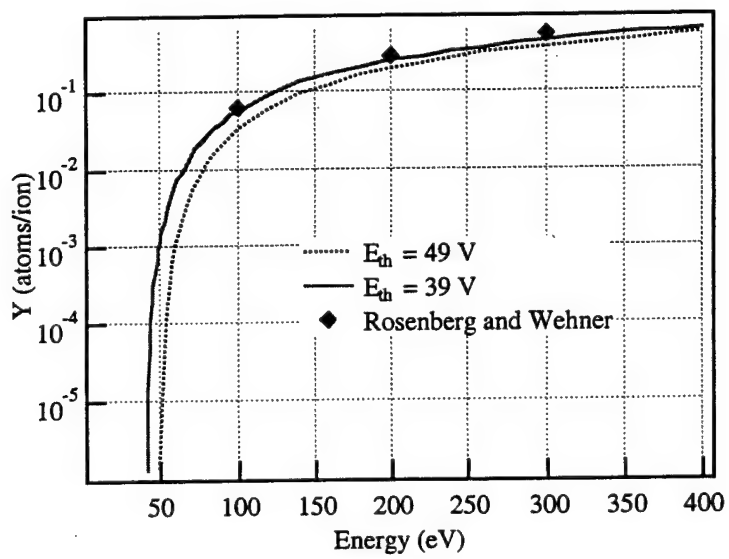

Figure 4.4 Sputter yields for a Mo target being bombarded by Xe ions. Shown on the graph are theoretical curves for two values of E_{th}, and experimental values measured by Rosenberg and Wehner.[78]

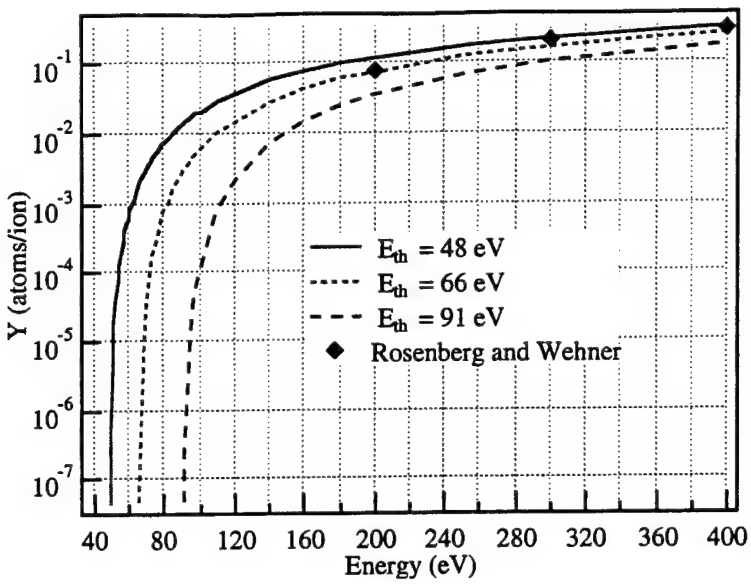

Figure 4.5 Sputter yields for a Si target being bombarded by Xe ions. Shown on the graph are theoretical curves for three values of E_{th}, and experimental values measured by Rosenberg and Wehner.[78]

The results of molybdenum cathode testing are reported with more confidence because experiments were conducted at low voltages lasted for several hours and were repeated. The model developed by Yamamura et al. predicted that E_{th}=49 eV. Cathode experiments in $2x10^{-5}$ Torr of xenon showed that performance changes sometimes occurred with V_g at 50 V where E_{imax} is 46 eV, therefore the E_{th} must be below 49 eV. Experimental results combined with results of the performance model discussed in this chapter, is required for a better estimate of the E_{th}.

4.2 Modeling Results

The performance degradation model discussed in this chapter requires input including experimental I-V data from a FEA cathode, cathode geometry parameters, and sputter yield parameters before FEA cathode performance degradation can be predicted. It incorporates the physics of field electron emission, ionization of xenon, and sputtering of the tip emitting area by ion bombardment and are used to estimate the change in radius

of curvature of cathode microtips and corresponding current expected during electron emission into xenon environments. This model can only predict changes in the cone structure by increases in the effective tip radius, r_t. If tip sharpening occurs or a reduction in cone half-angle, cathode performance will improve. It is possible that this process did occur during Xe exposure experiments with V_a>80 V and is responsible for the performance improvements discussed in the previous chapter. Therefore, the performance degradation model is expected to predict cathode performance degradation in Xe environments best when V_a is low and damage from ion bombardment primarily occurs to the emitting area of the tips. This situation is of primary interest for the electric propulsion application. In the xenon environment of a Hall thruster, the virtual anode potential will only be ~20 V above the gate electrode potential. Therefore, operating with V_a at 20V +V_g best represents the cathode and thruster operating configuration.

4.2.1 Mo SRI International Cathode

The performance degradation of a Mo cathode operating in a Xe environment with a low V_a (80 V) and V_g at 65 V was modeled with remarkable results. The measured response of the cathode current to increases in xenon pressure is shown in Figure 4.6 as I_{meas}. I-V data taken before the exposures are shown in Figure 4.7 as I_{meas}. The Jensen performance model was used with these data to estimate Δs and r_t shown in Table 4.2 as data set I. Figure 4.7 also shows the I-V relationship calculated with the Jensen electron emission model using the experimentally determined Δs and r_t, as I_{calc}. The cathode performance decay caused by exposure to the xenon environment was predicted using the model. If an E_{th} of 49 eV was assumed, as the model developed by Yamamura et al. predicted, the performance decay rate was greatly underestimated. Using E_{th} at 39 eV, the cathode performance degradation model predicted the performance decay shown in Figure 4.6 as I_{calc}. The correlation between experiment and

theory is remarkable. The sputter yield curve generated by the model model developed by Yamamura et al.[67] using E_{th} at 39 eV provides a better fit to values measured by Rosenberg and Wehner[78] at ion energies below 300 eV, as shown in Figure 4.4. Cathode parameters obtained from I-V traces taken before and after the Xe exposure are shown in Table 4.2. Changes in cathode parameters predicted by the performance degradation model are shown as data set III in Table 4.2. During exposure to xenon, r_t increased and Δs decreased; the sharpest tips were damaged at the fastest rate increasing uniformity in tip radius across the array, and decreasing Δs.

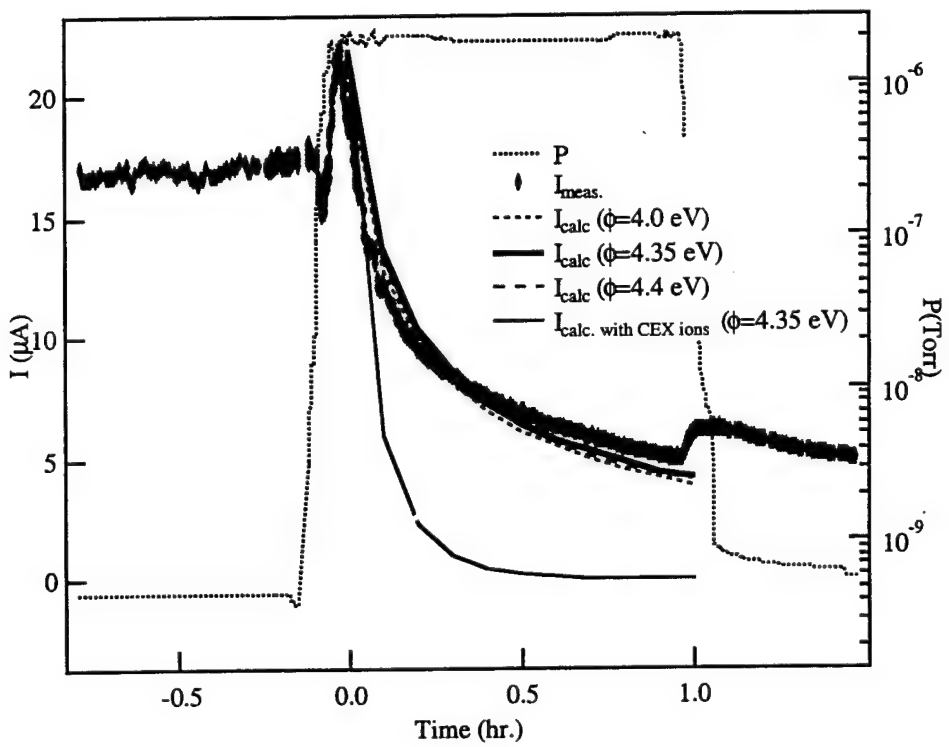

Figure 4.6 Experimental and theoretical Mo cathode current response to a Xe pressure increase up to $2x10^{-6}$ Torr with V_g at 65.6 V and V_a at 80 V with E_{th} of 39 eV.

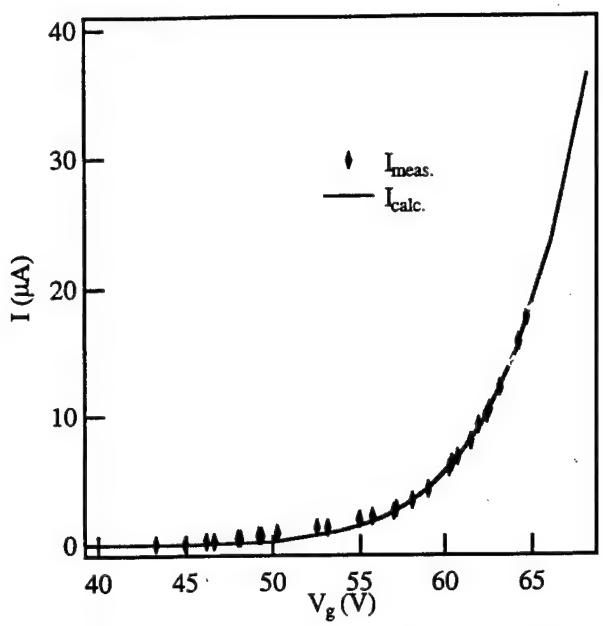

Figure 4.7 Mo cathode I-V data measured experimentally before the Xe exposure and predicted by Jensen's performance model.

Table 4.2 Cathode parameters before (I) and after (II) Xe exposure obtained from I-V data and predicted (III) by the performance degradation model.

	ϕ_w (eV)	β_c (rad.)	r_g (Å)	Ntips	A_{FN} (A/V^2)	B_{FN} (V)	r_t (Å)	Δs
I	4.35	0.26	4500	50000	0.0013	819	43.6	50.0
II	4.35	0.26	4500	50000	0.0024	952	53.5	42.5
III	4.35	0.26	4500	50000			53.6	40.8

The performance degradation model was also used to study the effect of work function on E_{th} estimates. The work function typically used for Mo is 4.3-4.4 eV.[79] Performance degradation rates were predicted assuming three different work function values and the same E_{th} value of 39 eV. The results showed that performance degradation rates predicted using each ϕ_w value were consistent with experimental results when an E_{th} value of 39 eV was used. Therefore, the E_{th} estimates do not seem to be significantly affected by the assumed work function in the range of possible values.

The performance degradation model was applied to predict the gate electrode voltage threshold for significant performance degradation for comparison to experimental

observations. Experimental results presented in the previous chapter in Figure 3.19 show that at 58 V the SRI cathode current dropped by 6% during 10 min. with V_a at 100 V. The cathode parameters before the exposure are shown in Table 4.3 as data set I. Figure 4.8 shows that the model predicted the dI/dt measured with V_g at 64 V for this cathode. A comparison of cathode parameters before and after the exposure to xenon in Table 4.3 shows that Δs increased and r_t barely changed. Ion bombardment of the microtips could have changed half-cone angle or nanoprotrusion emission sites while sputtering the tip emitting area. The same cathode was used in an experiment which showed that the cathode performance is affected by the voltage applied to the anode in xenon environments. With V_g at 50 V, the cathode performance increased as V_a was increased from 60 V up to 120 V. With increasing anode voltage, more ions could be bombarding the microtips off-axis increasing the sputtering of the cone sidewalls, which sharpens the tips and reduces the cone half-angle. With V_a at 100 V there is a combination of changes occurring to the cathode to improve and degrade cathode performance. At lower V_a, modeling results are more consistent with experimental results. Longer duration experiments are required at lower anode voltages to better understand discrepancies between theoretical and experimental results.

Initial cathode performance requirements are less than 10% current reduction during 100 hours in $2x10^{-5}$ Torr of xenon. The performance degradation model was used to investigate the effect of xenon exposure on cathode performance during 100 hours. The cathode parameters shown in Table 4.3, data set I, were used in the model. The performance degradation model predicted that if this cathode is operated in $2x10^{-5}$ Torr, it will demonstrate a current reduction of 5% when V_g is 55 V after 10 hours of operation. Performance degradation predicted by the model for the same cathode in the same environment at various gate voltages during 100 hours is shown in Figure 4.9. During 100 hours of operation, the current will decrease by 34 % of its original value with V_g at 55 V. It was determined that the gate voltage for this cathode cannot be higher than 52 V

to limit the current decay to less than 10% during 100 hours. The current for this cathode at 52 V is only 10.4 nA. At this voltage, 10^7 of these cathodes would be required, or $5x10^{11}$ tips to emit 100 mA. The size of this cathode would be 8 m^2. The performance degradation of the cathode only considered the ions created locally. If additional ion populations are present, operating voltages will be limited to even lower values and cathode dimensions will be significantly larger.

Table 4.3 Cathode parameters before (I) and after (II) xenon exposure which are used in the performance decay model for V_a at 100 V in $2x10^{-5}$ Torr of xenon.

	ϕ_w(eV)	β_c(rad.)	r_g(Å)	A_{FN}(A/V^2)	B_{FN}(V)	r_t(Å)	Δs
I	4.35	0.26	4500	0.0043	1092	64.9	18.2
II	4.35	0.26	4500	0.00246	1104	66	32

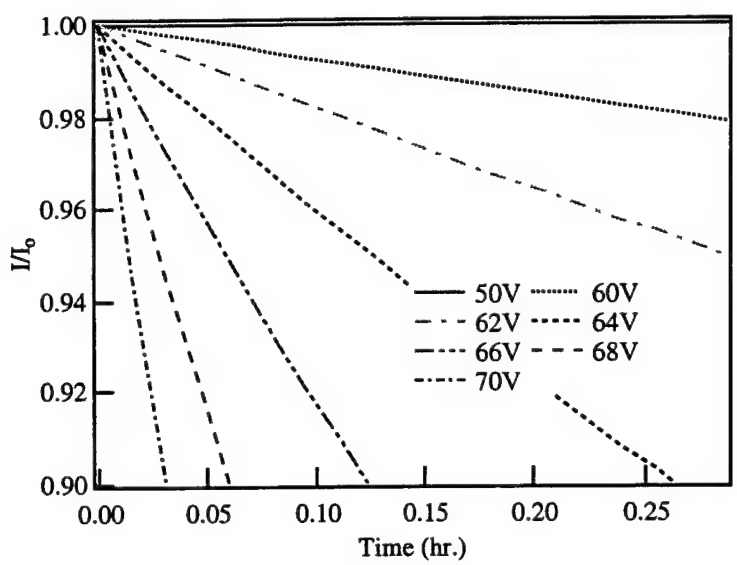

Figure 4.8 Performance decay rate predicted by the performance degradation model for a Mo cathode operating in a Xe environment with a pressure of $2x10^{-5}$ Torr for a cathode with parameters (I) shown in Table 4.3.

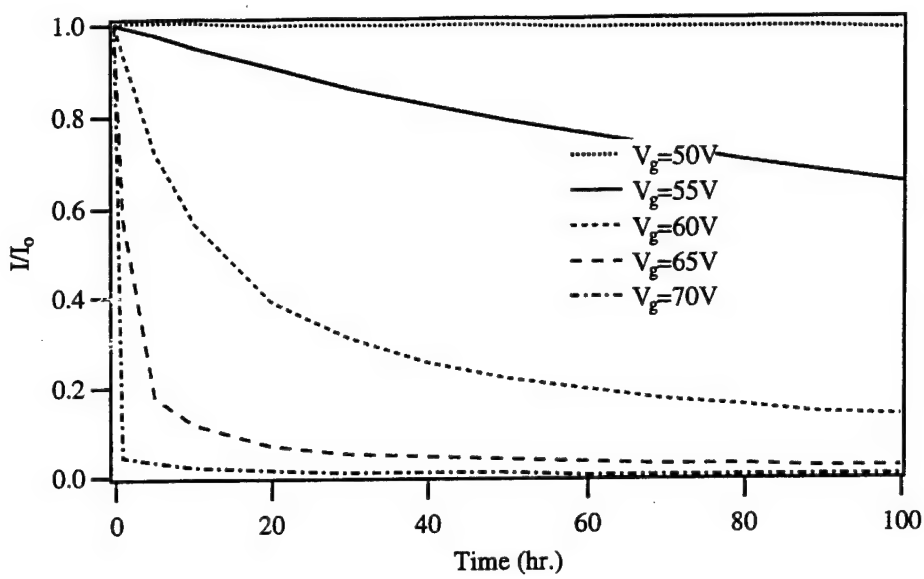

Figure 4.9 Field emission array cathode performance decay predicted by the performance degradation model for a Mo cathode operating in 2x10^{-5} Torr of Xe for 100 hours at various gate electrode voltages with initial cathode parameters (I) shown in Table 4.3.

In the cathode environment of a Hall thruster with a virtual anode potential only 20 V greater than the gate electrode potential, ions bombarding the cathode that originate near the tips will primarily affect changes in r_t. In the Hall thruster environment, the CEX ion population will contribute an additional ion current density of 0.02 mA/cm^2 to the cathode which is distributed uniformly to the surface of the cathode cones, as discussed in Chapter 2. The significant effect of the CEX population on performance degradation of the Mo cathode with parameters (I) shown in Table 4.2, is also shown in Figure 4.6. The cathode performance degradation attributable to local ions is negligible in comparison. Not only will this ion population degrade cathode performance by sputtering the microtip radius of curvature to degrade performance as shown in Figure 4.6, it will also sputter material off of the cone sidewalls which will redeposit on the insulator walls. With ion energies at eV_g+20eV=85eV, and xenon pressure at 2x10^{-5} Torr, the gate could be shorted to the tips within several minutes. For thruster and Mo FEA cathode technologies to be compatible, either the potential between the plasma and

microtips must be below the voltage threshold for sputtering, or the cathode must be shielded from this population of ions. To shield the microtips from CEX ions, CLAIR was developed. CLAIR is a cathode lens and ion repeller (CLAIR) configuration proposed to prevent the CEX ions from bombarding the cathode microtips. CLAIR has a series of electrodes similar to the gate electrode that electrostatically retards CEX ions and focuses the electrons through the highest voltage electrode. The CLAIR configuration is shown and discussed in Appendix B. If the cathode cannot be shielded from these ions, then molybdenum cathodes must be limited to operating voltages below ~19 V to achieve lifetimes greater than 100 hours.

4.2.2 Si MCNC FE Cathodes

Silicon FEA cathode performance degradation was also modeled, and the results were compared to experimental results. Results of modeling and experimental measurements of the performance degradation of Si cathodes in Xe environments showed that the E_{th} is also much lower than originally predicted by the model developed by Yamamura et al. Figure 4.10 shows the measured cathode response to an increase in xenon pressure with V_g at 70 V and V_a at 70 V. Cathode performance was poor because this cathode had been damaged in several other experiments. The cathode current before the exposure with V_g at 70 V was 3.2 nA with good emission stability. The cathode current dropped to 1.6 nA during 1 hour at $2x10^{-5}$ Torr. Correlation between experiment and theory is good if an E_{th} value of 48 eV is used in the sputter yield model. Sputter yield curves with different E_{th} values are shown in Figure 4.5. With E_{th} at 48 eV a better fit to experimental measurements of sputter yield data obtained by Rosenberg and Wehner is obtained than with E_{th} at 91 eV. Performance degradation curves were determined using a range of work function values, as shown in Figure 4.10. Results showed that an E_{th} value at 48 eV produced theoretical results consistent with

experimental results for a range of possible silicon work functions. The work function of silicon depends on how it has been doped. A work function of 4.05 eV is assumed for the MCNC Si cathodes tested.[80] To avoid sputter damaging the MCNC Si cathode by ions created locally, operating voltages must be limited to values below 53 V. At this voltage E_{imax} is 47 eV, below the E_{th} for Xe ions to sputter Si targets.

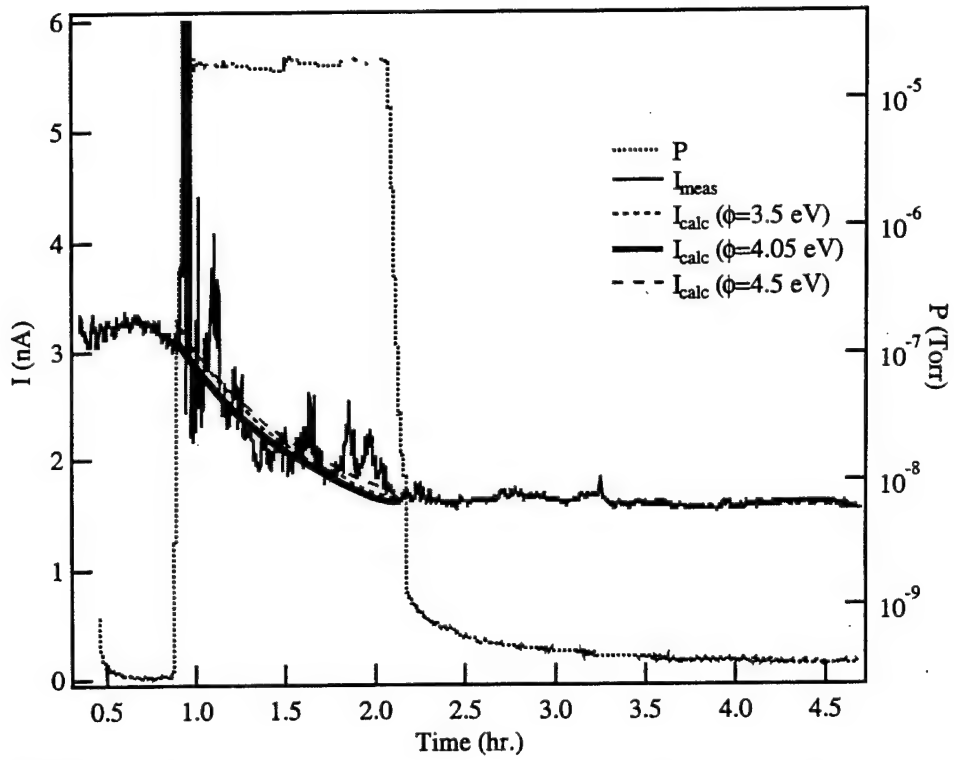

Figure 4.10 Measured and predicted Si cathode current response to an increase in Xe pressure up to $2x10^{-5}$ Torr with V_g and V_a at 70 V.

Modeling results were compared to another set of experimental data acquired during Si cathode operation in a xenon environment. This experiment was conducted with a much higher voltage applied to the anode, 400 V, and higher emission current. In experiments conducted with V_a>80 V, it is believed that the performance degradation model is not sufficient to account for all of the changes in cathode structure caused by xenon ion bombardment. Figure 4.11 shows the response of a Si cathode from MCNC to

an increase in Xe pressure. The cathode parameters before the exposure are shown in Table 4.4. Figure 4.11 shows the performance decay predicted by the model using the initial cathode parameters. The model slightly over predicts the performance degradation rate. It is possible that this result occurs because of the high voltage applied to the anode, 400 V. At this voltage, there could be a combination of tip blunting to degrade performance and tip sharpening and half cone angle reduction to improve cathode performance as shown in Figure 3.22. Reductions in work function could also be occurring as the xenon ions sputter clean the cathode surface. The increase in current as the xenon pressure is increased initially could be attributed to decreases in cathode work function. Silicon emitters naturally have a SiO_2 film on the tips that increases the work function. If this film is sputtered off, work function decreases would be expected. Any change in cathode configuration to improve performance will result in a slower performance degradation rate and discrepancies between experimental and theoretical results.

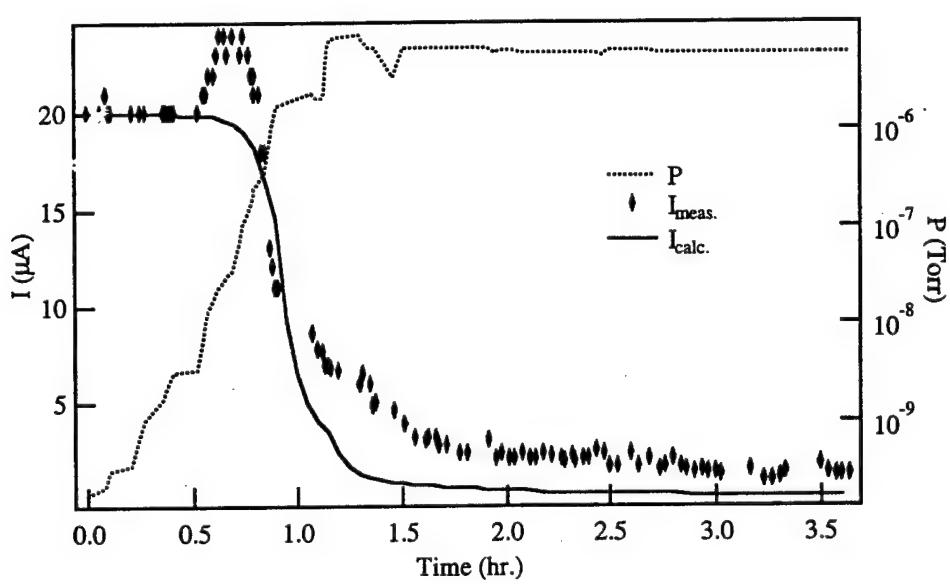

Figure 4.11 Measured and calculated Si cathode performance degradation as the Xe pressure increases up to $7x10^{-6}$ Torr with V_g at 86 V and V_a at 400 V.

Table 4.4 MCNC Si cathode parameters before the exposure to xenon during operation.

ϕ_w (eV)	β_c (rad.)	r_g (Å)	N_{tips}	r_t (Å)	Δs
4.0	0.26	10000	16000	45.2	185

Experimental and performance decay modeling results were used together to gain a better understanding of how Mo and Si FEA cathodes will respond to the xenon environment of a Hall thruster. Experimental results showed that the E_{th} values for xenon ions sputtering Mo and Si are much lower than the model developed by Yamamura et al.[67] predicted. The modeling and experimental results showed that the gate voltage should be below 43 V and 53 V to avoid sputter damaging the emitting area of the Mo and Si tips, respectively, by ions created locally. It was shown that the population of CEX ions created near the thruster will be even more damaging to the cathode than the ions created locally. To prevent local and CEX ions from sputter damaging the Mo and Si tips and CEX ions from shorting the gate to the tips, the gate voltage should be lower than 19 V and 28 V, respectively.

There are a lot of assumptions made to predict electron emission and tip sputtering by ion bombardment that greatly simplify modeling the physics of these processes. In spite of such simplifications, the models are able to capture the majority of the physics so that modeling results show impressive correlation with experimental results in the cathode and test configurations studied. Experimental and theoretical results also lead to a better understanding of how and when to use the model. The results of this investigation can now be applied in parametric studies of cathode design and performance in Xe environments.

4.3 Application of Modeling and Experimental Results

The cathodes used in this investigation demonstrated less than ideal FE cathode performance because they did not represent state-of-the-art FE cathode technology and the anode and cathode could not be cleaned in the vacuum facility prior to testing. Any FEA cathodes are very difficult to acquire; state-of-the-art FEA cathodes were impossible to acquire. Cathodes with better uniformity and smaller dimensions have demonstrated better performance in other UHV test facilities. Even the Mo cathode used in this investigation demonstrated much better performance at SRI International before it was tested at JPL. However, the experiments produced the results required in this study. This model can now be applied to predict the performance degradation of any cathode once the cathode geometry is known and an I-V trace has been obtained in UHV to estimate r_t and Δs. The initial cathode performance objective is emission of 100 mA from ~1 cm^2 in $2x10^{-5}$ Torr of xenon for 100 hours with less than 10 % current reduction from local and CEX ion bombardment. The performance of the cathodes evaluated at JPL indicated that the cathodes used in this study could not meet these requirements, however, cathodes tested elsewhere may satisfy the requirements. This section presents the results of an investigation into the theoretical performance of more ideal cathode configurations in Hall thruster environments to determine the cathode configurations required to be compatible with EP systems.

The performance of a Mo cathode configuration from SRI International was modeled in a Hall thruster environment. This cathode, #52M, was tested at SRI International where an I-V curve was obtained to determine Δs and r_t. The actual cathode parameters are shown in Table 4.5 in the first row and first 5 columns in bold type. The predicted performance of cathodes with similar configurations is also presented in that table to show how varying some parameters would affect the cathode performance. Upper limits on operating voltages were determined for operating conditions with and

without a CEX ion population so that the current did not drop by more than 10% during 100 hours. The number of tips in an array was scaled to attain approximately100 mA. Table 4.5 shows the number of tips required to emit ~100 mA from different cathode configurations with lifetimes greater than 100 hours. Higher gate voltage operation, ~43 V, is tolerable when the CEX ion population is not contributing to cathode microtip sputtering. With the original cathode configuration (case I) and a gate electrode at 43 V, 1.3×10^8 tips are required. The packing density of this cathode, #52M, is 16,000,000 tips/cm^2, therefore, this cathode would be 8 cm^2 in size. Much smaller cathodes are required for the compatibility of Hall thrusters and FEA cathodes. The size of this cathode would be acceptable if the packing density is increased by a factor of 10. The number of tips required from similar cathode configurations is also shown in Table 4.5. Reducing the gate aperture radius from 2000Å to 1000Å reduces the number of tips required in the cathode by an order of magnitude. The cathode described by case 2 should be compatible with a Hall thruster without CEX ions bombarding the microtips. Decreasing the tip radius and increasing the uniformity of tip radii in an array can also significantly improve the performance of the cathode so that the cathode size is less than 1 cm^2. Increasing the packing density in an array by an order of magnitude will also reduce the size of the cathode required to <1 cm^2.

Presence of a CEX ion population significantly reduces the upper limit on the operating voltage. With the CEX ions, voltage of the gate electrode must not be higher than 20 V for a Mo cathode. At this low voltage, a prohibitively large number of microtips, 4.5×10^{15}-3.5×10^{11}, are required to attain the desired current, 100 mA. Improvements to the cathode uniformity of microtip radius could significantly reduce the number of microtips required for the desired current. This cathode would still be prohibitively large because it would be considerably larger than the propulsion system. While this cathode demonstrated excellent performance in UHV environments, it could

only be used with a Hall thruster if a filter like CLAIR is used to prevent CEX ions from bombarding the cathode tips so that operation ~42 V is an option.

Table 4.5 SRI International #52M Mo cathode parameters (in bold) and predicted performance using different parameters, with and without a CEX ion bombardment during 100 hours.

case	ϕ_w (eV)	β_c (rad.)	r_g (Å)	r_t (Å)	Δs	V_g (V)	N_{tips}	I_o (mA)	I_f (mA)
1-Mo	**4.41**	**0.1974**	**2000**	**40.4**	**1.98**	43	$1.3x10^8$	108	107
2-Mo	4.41	0.1974	1000	40.4	1.98	42	$1.4x10^7$	105	101
3-Mo	4.41	0.1974	1000	30	1.98	42	$1.2x10^6$	108	107
4-Mo	4.41	0.1974	2000	40.4	1	43	$6.5x10^7$	107	106
5-Mo	4.41	0.1974	2000	30	1.98	43	$7x10^6$	100	95
6-Mo_{CEX}	**4.41**	**0.1974**	**2000**	**40.4**	**1.98**	20	$4.5x10^{15}$	108	101
7-Mo_{CEX}	4.41	0.1974	1000	40.4	1.98	20	$4x10^{13}$	104	98
8-Mo_{CEX}	4.41	0.1974	1000	30	1.98	20	$3x10^{11}$	107	101

Molybdenum cathodes fabricated at MIT/LL have demonstrated record low operating voltages because of incredibly small cathode dimensions. FEA cathodes at MIT/LL have been fabricated with r_g only 800 Å and packing densities of $10^9/cm^2$. A current of 1 μA has been demonstrated at 25 V with a molybdenum cathode that has 900 tips (2.8 nA/tip) and 0.32 μm tip-to-tip spacing. A cathode with the same configuration and quality could supply 100 mA at 25 V from a 3x3 mm cathode with $9x10^7$ tips and possibly 100 mA from less than 1 cm^2 at 20 V. Scaling up the cathode in number of tips with the same performance and uniformity is the challenge yet to be met so that Mo cathodes are compatible with EP systems. Mo cathodes may only be compatible with EP systems if CLAIR is used to prevent CEX ions from bombarding the microtips.

FEA cathodes employing other materials, which are currently being developed, could demonstrate performance superior to the Mo cathodes. A Si cathode with dimensions much smaller than the cathodes used in the experiments discussed in Chapter

3 could run at higher gate voltages and require fewer microtips for the lifetime and current requirements, as shown in Table 4.6. The performance of Si cathodes could be better than Mo for this application because the work function is lower and the E_{th} for sputtering is higher. Even considering the CEX ion population, silicon cathodes with the dimensions shown in cases 12 and 13 should be able to operate at 100 mA for 100 hours if tips are fabricated on 0.5 μm centers or smaller so that the cathode dimensions will be less than 1 cm^2. A current of 2.5 μA has been measured from a single silicon microtip structure at 25 V.[68] If silicon FEA cathodes could be fabricated with great uniformity in tip radius across an array, they could provide 100 mA of current from an array with less than 10^6 microtips with an emitting area <1 cm^2. Fabricating FEA cathode with the uniformity required is currently the greatest challenge in FEA cathode fabrication. Other cathode materials can further improve cathode performance. HfC and ZrC have demonstrated work function values between 3.3 and 3.5 eV.[81,82] Table 4.6 shows the reduction in number of tips required if the work function is reduced to 3.3 eV for a particular cathode configuration. The number of tips required was reduced by almost two orders of magnitude by reducing the work function from 4.0 to 3.3 eV. The performance degradation was determined using the sputter yield of a Si target by xenon ions, however it is believed that the sputter yield of HfC and ZrC will be much lower because these materials have demonstrated incredible robustness during ion bombardment. HfC and ZrC cathodes could operate at much higher voltages than Si and Mo cathodes without being damaged by ion bombardment which will further result in fewer tips required to meet lifetime and current requirements. Table 4.6 shows that HfC cathodes will be able to operate in EP system environments with or without CEX ions and with or without CLAIR.

Table 4.6 Performance limitations of Si and HfC cathodes with and without a charge-exchange (CEX) ion population.

Case	ϕ_w (eV)	β_c (rad.)	r_g (Å)	r_t (Å)	Δs	V_g (V)	N_{tips}	I_o (mA)	I_f (mA)
9-Si	4.0	0.26	2000	40.4	1	52	$6x10^5$	105	104
10-Si	4.0	0.26	2000	40.4	2	52	$1.2x10^6$	106	106
11-Si_{cex}	4.0	0.26	2000	40.4	2	30	$8.3x10^9$	109	101
12-Si_{cex}	4.0	0.26	2000	30	2	30	$2.6x10^8$	100	92
13-Si_{cex}	4.0	0.26	1000	40.4	2	30	$2.9x10^8$	109	102
14-HfC_{cex}	3.3	0.26	1000	40.4	2	30	$3x10^6$	106	100
15-HfC_{cex}	3.3	0.26	2000	40.4	2	30	$4.6x10^7$	105	100

HfC and ZrC cathodes have also demonstrated greater stability in contaminating environments and at higher currents than Mo and Si cathodes. Chemical inertness will be very important during operation in Hall thruster test facilities where base pressures are typically greater than 10^{-7} Torr. With cathodes that are capable of >100 mA/cm^2, the emission current will be limited by space-charge effects. The cathode must be designed with the proper tip-to-tip spacing to achieve the desired emission current, ~100 mA. Space-charge limited emission is discussed in the following chapter.

CHAPTER 5

SPACE-CHARGE LIMITED ELECTRON EMISSION FROM FIELD EMISSION CATHODES INTO A PLASMA

In this chapter, the development of a sheath model is discussed with results used to predict sheath structure and emission current limitations for different cathode operating configurations. The sheath was modeled in one dimension only, therefore the effect of the potential of surrounding electrodes on sheath structure was not considered. The model is based on a planar sheath model that was originally developed by Crawford and Cannara[54] and Prewett and Allen[55] with a sheath boundary criterion derived by Andrews and Allen[56] This model and criterion were used and augmented by Goodfellow to consider the initial electron thermal energies at the surface of a hot cathode.[57] In the derivation of the sheath model used in this investigation, initial electron energies were used which corresponded to the accelerating potential between the electron emitting surface and gate electrode. This sheath model was then developed for cylindrical and spherical sheath configurations also. One of the objectives of this study was to determine the potential of the gate electrode, with respect to the plasma potential, required to transmit the desired electron current through the sheath with various electron energies. The details of the pre-sheath were not explored; however, it was assumed that the ions were accelerated through the pre-sheath up to high enough velocities to ensure monotonic potential profiles in the cathode sheath. The Andrews and Allen criterion was used to determine the ion energy at the sheath boundary. It is possible that a virtual cathode forms in the sheath, where a potential minimum in the sheath is lower than the cathode

potential. Virtual cathode formation plasma instabilities could increase the upper limits on the space-charge limited emission current and change the structure of the sheath; however these scenarios cannot be considered by the sheath model. This 1-D sheath model was used to determine upper and lower limits on current emitted by a planar FE cathode due to space-charge effects and limiting sheath geometries and is limited to stable monotonic potential profiles in the sheath. The results of this model are compared to the results of a Particle-in-Cell (PIC) model capable of considering virtual cathode formation.

This sheath model was developed for planar, cylindrical, and spherical cathode and sheath geometries. A cathode and sheath potential diagram is shown in Figure 1.6 and a possible potential profile is shown in Figure 5.1. FE cathodes are planar, however the structure of the sheath depends on the size of the cathode and on the plasma environment. With cathode dimensions greater than several electronic Debye lengths, the sheath structure is primarily planar. If cathode dimensions are much smaller than the sheath thickness, the sheath is better represented by a spherical sheath model. Two different cathode and sheath scenarios are illustrated in Figure 5.2. The cathode dimensions and environment significantly affect the emission current limitations, as shown in the following sections of this chapter.

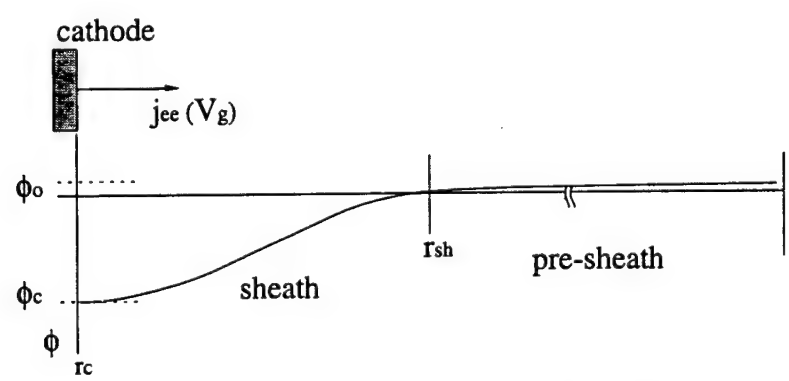

Figure 5.1 Cathode sheath configuration which was modeled. The boundary between the sheath and pre-sheath is shown at r_{sh}.

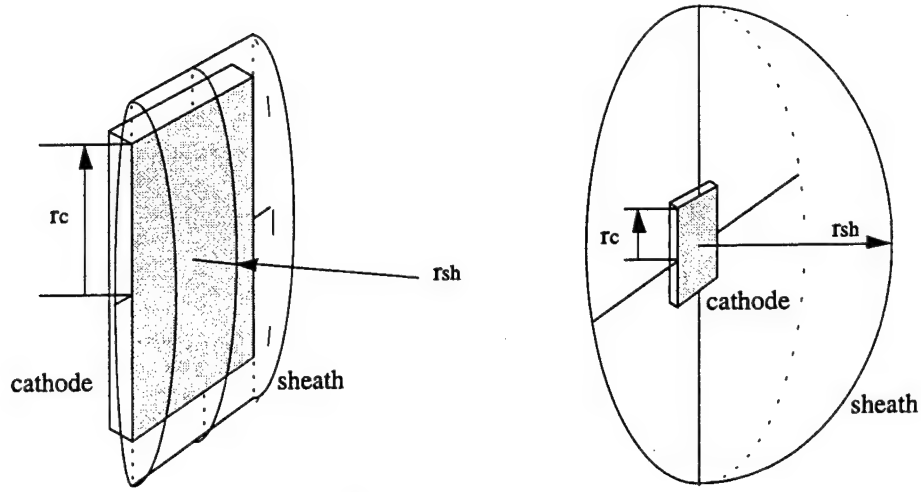

Figure 5.2 A planar cathode sheath scenario (left) with $r_c > r_{sh}$ and a spherical cathode sheath scenario (right) with $r_c < r_{sh}$.

The three environments considered in this study for space-charge limited emission from a FE source of electrons into a plasma are those generated by a Hall thruster, a mesoscale ion thruster, and a tethered spacecraft in low Earth orbit. Since a large Hall thruster could use a FE cathode internal or external to the thruster as shown in Figure 1.3, both conditions were considered in the analysis. A small or mesoscale Hall thruster will require an external cathode. Electron temperatures in the environment of a Hall thruster were obtained by Domonkos et al.[83] in the plasma plume of a 1.4 kW Hall thruster. Plasma number densities were approximated from Faraday probe measurements discussed in Chapter 2. These parameters were used in the model because initial testing of these cathodes with Hall thrusters will most likely occur with such medium scale systems. An ion engine requires two cathodes; one cathode in the discharge chamber for propellant ionization, and another cathode external to the thruster for ion beam neutralization. Plasma parameters used to represent the environment of an ion engine discharge chamber are estimates only for a mesoscale ion engine. Charged particle number densities could be much higher in mesoscale ion engines to get the required

performance. There is also interest in using FE cathodes on tethers in low Earth orbit to emit electrons ~250-1000 km above the earth. The parameters used to represent each of these environments are presented in Table 5.1. Ambient electron number densities are given at an altitude of 300 km; at higher altitudes, electron number densities will be even lower.

Table 5.1 Characteristics of the thruster and tether plasma environments investigated using the cathode sheath model.

	n_{eo}(/cm^3)	T_e(eV)	λ_D (mm)
Hall/Ion thruster side	$8x10^8$	5	0.60
Hall thruster center[a]	$8x10^{10}$	1	0.03
Ion engine discharge chamber	$3x10^{11}$	2-3	0.02
Tether at 250 km[b]	$5x10^5$	0.1	3.3

[a] Domonkos, M. T. Marrese, C. M., Haas, J. M., Gallimore, A. D., "Very Near-Field Plume Investigation of the D-55 Anode Layer Thruster," AIAA-97-3062 Joint Propulsion Conference, Seattle, WA, July 1997.

[b] F. F. Chen, *Plasma Physics and Controlled Fusion*, Plenum Press, New York, 1984.

A sheath model described in this chapter was used to estimate space-charge current limits that can be expected for FE cathodes in Hall, ion thruster, and electrodynamic tether environments described in Table 5.1. The effect of cathode operating voltages, sheath geometry, and cathode dimensions on the current limit was investigated. Modeling results are presented at the end of this chapter.

5.1 Sheath Model

5.1.1 Planar Sheath Geometry

A sheath model with a planar cathode and sheath geometry predicts conservative limits on cathode emission current due to space-charge effects. All potentials represented with ϕ are defined with respect to the potential at the sheath boundary where quasineutrality is

assumed. The pre-sheath accelerates the ions through ϕ_o to the sheath boundary. The potential difference between the plasma and cathode gate electrode is ϕ_c. Virtual cathode formation can not be predicted by this model; it can only predict monotonic potential profiles. The maximum current is associated with a zero electric field at the cathode surface. Full recombination is assumed for the ions at the cathode surface. Potential magnitudes are used in the input and output of this model for simplicity, however, their true signs are inherent to the following equations. In this case, the 1-D form of Poisson's equation is

Eqn. 5.1
$$-\frac{d^2(-\phi)}{dx^2} = \frac{\rho}{\varepsilon_o} = \frac{e}{\varepsilon_o}(n_i - n_{ee} - n_e).$$

The continuity and energy equations for the ions and electrons in the sheath are used to determine particle number densities. The ion number density at the sheath boundary is n_{io}. The ion number density, n_i, is

Eqn. 5.2
$$j_i = n_i e v_i = n_{io} e v_o(\phi_o),$$

Eqn. 5.3
$$\frac{1}{2} m_i v_i^2 = e(\phi + \phi_o),$$

Eqn. 5.4
$$n_i = n_{io}\left(1 + \frac{\phi}{\phi_o}\right)^{-\frac{1}{2}}.$$

Plasma electron densities are defined by the Boltzmann relationship for a Maxwellian distribution of electrons

Eqn. 5.5
$$n_e = n_{eo} \exp\left(\frac{-e\phi}{kT_e}\right).$$

It is assumed that the electrons are Maxwellian with temperature, T_e, and the number density at the sheath boundary is n_{eo}. The beam electron number densities are defined as

Eqn. 5.6
$$j_{ee} = n_{ee} e v_{ee}.$$

Eqn. 5.7
$$\frac{1}{2} m_e v_{ee}^2 = e(V_g + \phi_c - \phi),$$

Eqn. 5.8

$$n_{ee} = \frac{j_{ee}}{\left(\frac{2e^3}{m_e}\right)^{1/2}}\left(V_g + \phi_c - \phi\right)^{-1/2}.$$

The condition of quasineutrality at the sheath boundary is used to define the ion number density at the sheath boundary in terms of electron number densities. At ϕ=0

Eqn. 5.9

$$n_{io} = n_{eo} + n_{ee}\text{, and}$$

Eqn. 5.10

$$\frac{n_{io}}{n_{eo}} = 1 + \frac{j_{ee}}{n_{eo}\left(\frac{2e^3}{m_e}\right)^{1/2}}\left(V_g + \phi_c\right)^{-\frac{1}{2}}.$$

Poisson's equation can then be written as

Eqn. 5.11

$$-\frac{d^2(-\phi)}{dx^2} = \frac{\rho}{\varepsilon_o} = \frac{e}{\varepsilon_o}\left(n_{io}\left(1+\frac{\phi}{\phi_o}\right)^{-1/2} - \frac{j_{ee}}{e\left(\frac{2e}{m_e}\right)^{1/2}}\left(V_g + \phi_c - \phi\right)^{-1/2} - n_{eo}\exp\left(\frac{-e\phi}{kT_e}\right)\right).$$

The parameters used to normalize Eqn. 5.11 are

Eqn. 5.12

$$\eta = \frac{e\phi}{kT_e},$$

Eqn. 5.13

$$\xi = \frac{x}{\lambda_D},$$

Eqn. 5.14

$$\lambda_D = \left(\frac{\varepsilon_o kT_e}{n_{eo}e^2}\right)^{\frac{1}{2}},$$

Eqn. 5.15

$$\bar{\rho} = \frac{\rho}{en_{eo}}$$

Eqn. 5.16

$$j_e = n_{eo}e\left(\frac{2kT_e}{m_e}\right)^{1/2}\text{, and}$$

Eqn. 5.17 $$J_{ee} = \frac{j_{ee}}{j_e},$$

where λ_D is the electronic Debye Length. The normalized form of Eqn. 5.11 is

Eqn. 5.18 $$\frac{d^2\eta}{d\xi^2} = \bar{\rho} = \left(1 + J_{ee}\left(\eta_g + \eta_c\right)^{-\frac{1}{2}}\right)\left(1 + \frac{\eta}{\eta_o}\right)^{-\frac{1}{2}} - J_{ee}\left(\eta_g + \eta_c - \eta\right)^{-\frac{1}{2}} - \exp(-\eta).$$

The non-dimensional charge density is $\bar{\rho}$. Integrating Poisson's equation once and applying the first of the following two boundary conditions,

Eqn. 5.19 $$\frac{d\eta}{d\xi}(\eta = 0) = 0 \text{ and}$$

Eqn. 5.20 $$\eta(\xi = 0) = \eta_c,$$

the electric field in this region was determined to be

Eqn. 5.21 $$\left(-\frac{d\eta}{d\xi}\right)^2 = 4\eta_o\left(1 + J_{ee}\left(\eta_g + \eta_c\right)^{-\frac{1}{2}}\right)\left(\left(1 + \frac{\eta}{\eta_o}\right)^{\frac{1}{2}} - 1\right)$$

$$+4J_{ee}\left(\left(\eta_g + \eta_c - \eta\right)^{\frac{1}{2}} - \left(\eta_g + \eta_c\right)^{\frac{1}{2}}\right) + 2\left(\exp(-\eta) - 1\right).$$

The electric field at the sheath boundary is approximated at zero. This approximation is common because the electric field is very small in this region and has little effect on the structure of the sheath.[57,84] The ion energy at the sheath boundary can be approximated using the criterion derived by Andrews and Allen,[56]

Eqn. 5.22 $$\left.\frac{d\bar{\rho}}{d\eta}\right|_{\eta=0} = 0.$$

The ion energy at the sheath boundary, η_o, is determined using Eqn. 5.18 and Eqn. 5.22.

Eqn. 5.23 $$\eta_o = \frac{1 + J_{ee}\left(\eta_g + \eta_c\right)^{-\frac{1}{2}}}{2 - J_{ee}\left(\eta_g + \eta_c\right)^{-\frac{3}{2}}}.$$

Notice that in the limit of zero cathode emission η_o is 1/2. This result is consistent with the model developed by Bohm.[53] The upper limit on the emission current is defined as the current emitted when the electric field at the cathode surface becomes zero,

Eqn. 5.24
$$0 = 4\eta_o\left(1 + J_{ee\max}\left(\eta_g + \eta_c\right)^{-\frac{1}{2}}\right)\left(\left(1 + \frac{\eta_c}{\eta_o}\right)^{\frac{1}{2}} - 1\right)$$
$$+4J_{ee\max}\left(\left(\eta_g\right)^{\frac{1}{2}} - \left(\eta_g + \eta_c\right)^{\frac{1}{2}}\right) + 2\left(\exp(-\eta_c) - 1\right).$$

With this assumption, the maximum emission current possible is

Eqn. 5.25
$$J_{ee_{\max}} = \frac{\eta_o\left(\left(1 + \frac{\eta_c}{\eta_o}\right)^{\frac{1}{2}} - 1\right) + \frac{1}{2}\left(\exp(-\eta_c) - 1\right)}{\eta_o\left(\eta_g + \eta_c\right)^{-\frac{1}{2}}\left(1 - \left(1 + \frac{\eta_c}{\eta_o}\right)^{\frac{1}{2}}\right) + \left(\eta_g + \eta_c\right)^{\frac{1}{2}} - \left(\eta_g\right)^{\frac{1}{2}}}.$$

Eqn. 5.23 and Eqn. 5.25 can then be solved simultaneously to estimate J_{eemax} and η_o for any combination of η_c and η_g. J_{eemax} is the emission current density that corresponds to a zero electric field at the cathode surface. This value represents the lower limit on the emission current density capability of FE cathodes emitting electrons into a plasma. If electron beam expansion occurs in the sheath, virtual cathodes form in the sheath, or plasma instabilities develop, larger emission currents can be possible. Emission current limitations predicted by this model agree with results of the Goodfellow sheath model, which provided the basis for this model. In the case considered, η_c was 10, η_g was 0.3, and both models predicted that J_{eemax} was 0.7. Goodfellow used a similar sheath model combined with thermal models to predict cathode temperatures in a magnetoplasmadynamic thruster system, and achieved good correlation between experiment and theory. The results of the 1-D sheath model derived in this thesis work were also compared with the Prewett and Allen model results. A comparison of the

results from both models shown in Figure 5.3. The Prewett and Allen model assumes negligible initial velocities, and an η_g value of 10^{-8} is used in the model developed in this thesis work to obtain the results shown in Figure 5.3. The results of this model are consistent with results from the Andrews and Allen model and the Goodfellow model.

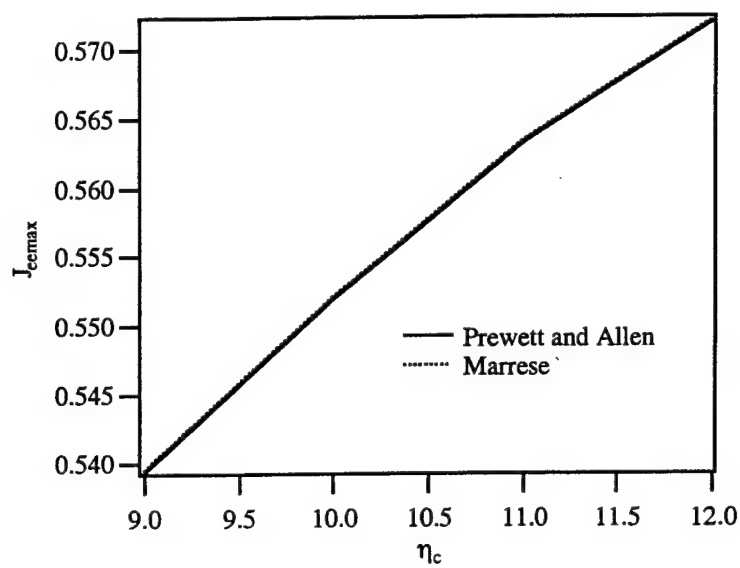

Figure 5.3 Results of the cathode sheath model compared to the Prewett and Allen sheath model results.

5.1.2 Cylindrical Geometry

The same sheath model was also developed for a cylindrical cathode and sheath geometry. This model assumes a 1/r expansion of the emitted electron current in the cathode sheath and consequent decrease in ion number density. As the sheath dimensions become comparable to the cathode dimensions some radial beam expansion occurs and the cylindrical sheath model becomes more appropriate than the planar model. In the cylindrical sheath model, the cathode is emitting electrons radially outward into a plasma where the electron number density is n_{eo}. Plasma electron number density is given by the Boltzmann equation, assuming a Maxwellian distribution of energies,

Eqn. 5.26 $$n_e = n_{eo}\exp\left(\frac{-e\phi}{kT_e}\right).$$

The number density of electrons emitted from the cathode is derived using the continuity,

Eqn. 5.27 $$j_{ee}(\pi r_c) = n_{ee}ev_{ee}(\pi r),$$

and energy equations,

Eqn. 5.28 $$v_{ee} = \left(\frac{2e(\phi_g + \phi_c - \phi)}{m_e}\right)^{\frac{1}{2}}.$$

The electron number density for the beam electrons is then

Eqn. 5.29 $$n_{ee} = \frac{j_{ee}}{\left(\frac{2e^3}{m_e}\right)^{1/2}}(\phi_g + \phi_c - \phi)^{-\frac{1}{2}}\left(\frac{r_c}{r}\right).$$

The continuity and energy equations are used to determine the ion number density,

Eqn. 5.30 $$j_i = n_i ev_i(\pi r) = n_{io}ev_{io}(\pi r_{sh}),$$

Eqn. 5.31 $$v_i = \left(\frac{2e(\phi_o + \phi)}{m_i}\right)^{\frac{1}{2}}, \text{ and}$$

Eqn. 5.32 $$n_i = n_{io}\left(1 + \frac{\phi}{\phi_o}\right)^{-\frac{1}{2}}\left(\frac{r_{sh}}{r}\right).$$

The initial ion energy at the sheath boundary is $e\phi_o$, and the ion number density at the sheath boundary is

Eqn. 5.33 $$n_{io}=n_{eo}+n_{ee}=n_{eo}\left(1 + \frac{j_{ee}}{n_{eo}\left(\frac{2e^3}{m_e}\right)^{\frac{1}{2}}}(\phi_g + \phi_c)^{-\frac{1}{2}}\left(\frac{r_c}{r_{sh}}\right)\right),$$

where quasineutrality is assumed. The ion number density in the sheath is

Eqn. 5.34

$$n_i = n_{eo}\left(1+\frac{j_{ee}}{n_{eo}\left(\frac{2e^3}{m_e}\right)^{\frac{1}{2}}}\left(\phi_g+\phi_c\right)^{-\frac{1}{2}}\left(\frac{r_c}{r_{sh}}\right)\right)\left(1+\frac{\phi}{\phi_o}\right)^{-\frac{1}{2}}\left(\frac{r_{sh}}{r}\right).$$

Poisson's equation can then be written for this cathode configuration and environment as

Eqn. 5.35

$$-\nabla^2(-\phi) = -\left(\frac{d^2(-\phi)}{dr^2}+\frac{1}{r}\frac{d(-\phi)}{dr}\right) = \frac{\rho}{\varepsilon_o}$$

$$= \frac{e}{\varepsilon_o}\left[n_{io}\left(1+\frac{\phi}{\phi_o}\right)^{-\frac{1}{2}}\left(\frac{r_{sh}}{r}\right) - \frac{j_{ee}}{e\left(\frac{2e}{m_e}\right)^{\frac{1}{2}}}\left(\phi_g+\phi_c-\phi\right)^{-\frac{1}{2}}\left(\frac{r_c}{r}\right) - n_{eo}\exp\left(-\frac{e\phi}{kT_e}\right)\right].$$

Eqn. 5.12-Eqn. 5.17 are used to get the normalized form of Poisson's equation describing the potential profile in the cylindrical sheath,

Eqn. 5.36

$$\frac{d^2\eta}{d\xi^2}+\frac{1}{\xi}\frac{d\eta}{d\xi} = \overline{\rho}$$

$$= \left(1+J_{ee}\left(\eta_g+\eta_c\right)^{-\frac{1}{2}}\left(\frac{\xi_c}{\xi_{sh}}\right)\right)\left(1+\frac{\eta}{\eta_o}\right)^{-\frac{1}{2}}\left(\frac{\xi_{sh}}{\xi}\right) - J_{ee}\left(\eta_g+\eta_c-\eta\right)^{-\frac{1}{2}}\left(\frac{\xi_c}{\xi}\right) - \exp(-\eta).$$

The Andrews and Allen criterion[56] is evaluated at the sheath boundary to derive the relationship for the normalized potential drop across the pre-sheath,

Eqn. 5.37

$$\eta_o = \frac{1+J_{ee}\left(\eta_g+\eta_c\right)^{-\frac{1}{2}}\left(\frac{\xi_c}{\xi_{sh}}\right)}{2-J_{ee}\left(\eta_g+\eta_c\right)^{-\frac{3}{2}}\left(\frac{\xi_c}{\xi_{sh}}\right)}.$$

Eqn. 5.36 is evaluated numerically using a Runge-Kutta fourth order method. The initial conditions at the sheath boundary are given by

Eqn. 5.38

$$\eta(\xi=\xi_{sh}) = 0 \text{ and}$$

Eqn. 5.39

$$\frac{d\eta}{d\xi}(\xi=\xi_{sh}) = 0.$$

The cylindrical cathode sheath problem is not very well defined, since only the potential at the cathode and sheath boundaries, and the electric field at the sheath boundary are known. The position of the sheath boundary is an input to the model, however, it has to be estimated initially. The much simpler nature of the equations for charged particle densities in the planar sheath geometry does not require this input parameter. The sheath thickness is a result of the planar sheath model; therefore, the structure of the sheath can be determined for any J_{ee}, η_c, and η_g combinations. In cylindrical coordinates the Poisson equation is more complicated, requiring more input parameters. Initial estimates are made for the thickness of the sheath, ξ_{sh}. It is assumed that the maximum current is emitted when the electric field at the cathode surface is zero and the potential at the cathode surface is equivalent to the cathode potential. The sheath thickness is adjusted until these conditions are met at the cathode surface to estimate J_{eemax}. A potential profile for the sheath can only be obtained for limiting cases. Potential profiles and J_{eemax} are obtained in this model for the limiting case of a zero electric field at the cathode surface.

5.1.3 Spherical Geometry

The sheath model with a spherical geometry was derived like the cylindrical model except that the ion and electron number densities change with a $1/r^2$ relationship in the sheath. Poisson's equation in spherical coordinates for this cathode, sheath configuration, and environment is

Eqn. 5.40

$$\frac{d^2\eta}{d\xi^2}+\frac{2}{\xi}\frac{d\eta}{d\xi}=\bar{\rho}$$

$$=\left(1+J_{ee}\left(\eta_g+\eta_c\right)^{-\frac{1}{2}}\left(\frac{\xi_c^2}{\xi_{sh}^2}\right)\right)\left(1+\frac{\eta}{\eta_o}\right)^{-\frac{1}{2}}\left(\frac{\xi_{sh}^2}{\xi^2}\right)-J_{ee}\left(\eta_g+\eta_c-\eta\right)^{-\frac{1}{2}}\left(\frac{\xi_c^2}{\xi^2}\right)-\exp(-\eta)$$

The pre-sheath accelerates the ions through a normalized potential η_o

Eqn. 5.41

$$\eta_o = \frac{1 + J_{ee}\left(\eta_g + \eta_c\right)^{-\frac{1}{2}}\left(\frac{\xi_c^2}{\xi_{sh}^2}\right)}{2 - J_{ee}\left(\eta_g + \eta_c\right)^{-\frac{3}{2}}\left(\frac{\xi_c^2}{\xi_{sh}^2}\right)},$$

as derived using the Andrews and Allen criterion. Eqn. 5.40 is evaluated numerically using a Runge-Kutta fourth order method for a second order differential equation. The initial conditions at the sheath boundary are Eqn. 5.38 and Eqn. 5.39. An upper limit on j_{ee} is determined using the spherical sheath model. Initial guesses are made for the thickness of the sheath, r_{sh}. It is assumed that the maximum current is emitted when the electric field at the cathode surface is zero and the potential at the cathode surface is equivalent to the cathode potential. The sheath thickness is adjusted until these conditions are met at the cathode surface.

5.2 Modeling Results

Space-charge limited FE was investigated for three geometrical sheath configurations in one dimension. The planar geometry was the simplest geometry considered. The results of this model are most accurate when the sheath thickness is much smaller than the cathode dimensions. As the cathode dimensions become smaller or the ambient ion and electron number densities decrease, the sheath becomes less planar and some radial beam expansion begins to occur in the cathode sheath. When the sheath thickness becomes several times larger than the cathode radius, the sheath approaches a spherical geometry. Lower energy emitted electrons will support a more spherical sheath configuration because the electron beam will be less collimated in the sheath. Local radial electric fields generated by high negative charge densities in the sheath will generate more expansion for a lower energy beam. With cylindrical and spherical sheath geometries, ion number densities increase in the sheath as $1/r$ and $1/r^2$, respectively, providing much better negative space-charge neutralization at the cathode surface by the

plasma ions than the planar geometry to permit higher emitted electron currents. The cylindrical and spherical sheath models were used to study the effect of cathode dimensions on FE current limitations, an investigation not possible with the planar model.

The planar model provided conservative estimates of upper cathode current limits set by space charge effects for a monotonic potential distribution. Virtual cathode formation and some plasma instabilities will increase the upper limits on the emission current. The results of this model are shown in Table 5.2. Current density objectives for tether and thruster environments are ~100 mA/cm^2 from a 1 cm^2 cathode. The results of the planar model show that the conservative estimates of lower limits on the emission current greatly exceed the requirements when the cathodes are used in the discharge chamber of an ion thruster or at the internal position of a Hall thruster. The sheath model results show that FE cathodes emitting into a tether environment are prohibitively limited by space-charge effects if a planar sheath geometry is assumed.

Table 5.2 Space-charge limited currents estimated by the planar sheath model for thruster and tether environments.

	n_{eo} (/cm^3)	T_e (eV)	V_g (V)	ϕ_c (V)	j_{eemax} (mA/cm^2)
Hall thruster-external	$8x10^8$	5	500	20	160
	$8x10^8$	5	100	20	68
	$8x10^8$	5	30	20	34
	$8x10^8$	1	30	20	17
Hall thruster-internal	$8x10^{10}$	1	30	20	1,700
	$8x10^{10}$	1	100	20	2,884
Ion engine discharge chamber	$3x10^{11}$	2	30	20	8,800
Tether	$5x10^5$	0.1	30	20	0.003
	$5x10^5$	0.1	100	20	0.005
	$5x10^5$	0.1	1000	20	0.016
	$5x10^5$	0.1	30	100	0.002

The effects of V_g and ϕ_c on the current limitations were also considered. The results of this investigation are also shown in Figure 5.4 and Figure 5.5. According to

these model results, cathodes will require operating voltages, ~200 V, which greatly exceed the sputter threshold of the Si or Mo cathodes if used external to the Hall or ion thruster where n_{eo} is $8x10^8$ /cm^3 and T_e is 5 eV. The effect of increasing the electron energy with the gate voltage, V_g, is shown in Figure 5.4. Increasing the electron energies at the gate electrode does increase the emission current from the cathode. Increasing the potential between the cathode and plasma, ϕ_c, either increases or decreases the emission current limit, depending on the initial electron energies, as represented by the gate electrode voltage,V_g. Increasing this potential only decreased the cathode current limit for η_g >2, as shown in Figure 5.5. Increased potential drops in the cathode sheath do not increase the electric field proportionally because increasing ϕ_c also increases the size of the sheath. Increasing ϕ_c with a planar sheath geometry also decreases the ion number density at the gate electrode because the ions are accelerated through a larger potential between the sheath boundary and gate electrode. This effect reduces negative space-charge neutralization by the ions. FE cathode gate electrode potentials should not be much more than 20 V below the plasma potential to maximize the current emitted from the cathode and minimize the thermalized electron current collected by the gate electrode. A gate electrode which is no more than 20 V below plasma potential is also required to avoid excessive cathode sputtering by the local ions, as shown in the results of the cathode sputtering model discussed in the previous chapter.

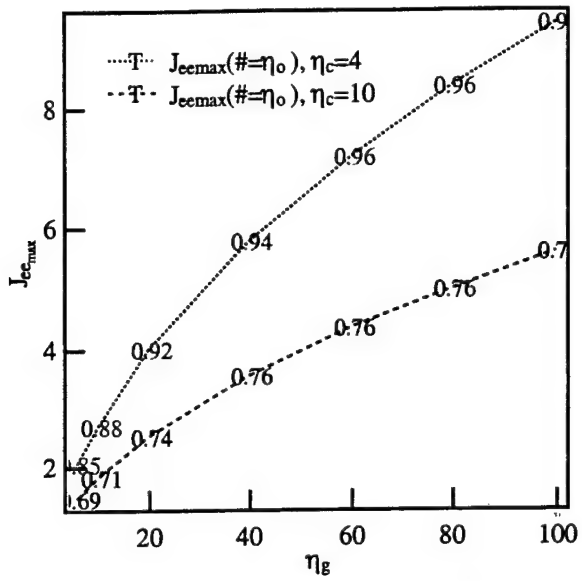

Figure 5.4 The effect of V_g on J_{eemax} for the planar sheath geometry. The numeric markers represent the value of η_o for each solution.

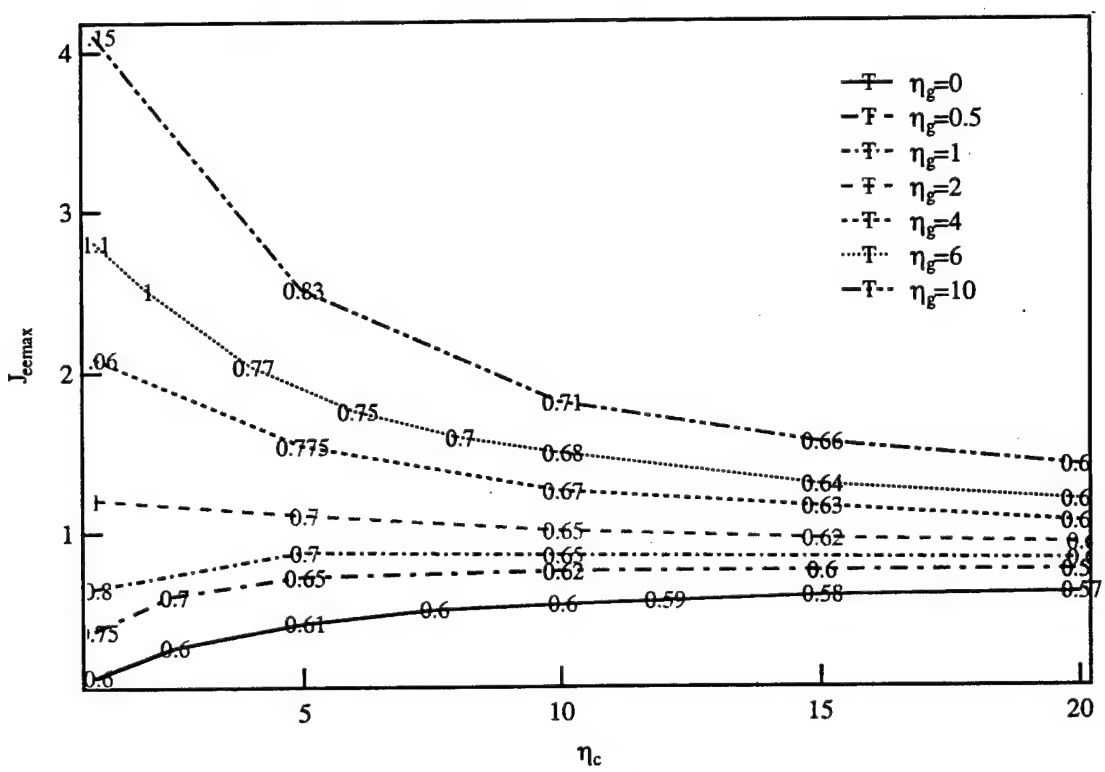

Figure 5.5 The effect of ϕ_c on J_{eemax} for the planar sheath geometry. The numeric markers represent the value of η_o for each solution.

Potential, electric field, and charge density profiles, as predicted by the planar cathode sheath model, are shown in the following figures for the Hall thruster application. Figure 5.6 shows potential and electric field profiles in the cathode sheath for some operating configurations. Charge density profiles are shown in Figure 5.7. The effect of J_{ee} on the sheath structure is shown. The charge density profiles show the double sheath structure for both J_{ee}=1.5, and 2.0, where the sheath consists of both positive and negative space-charge regions.

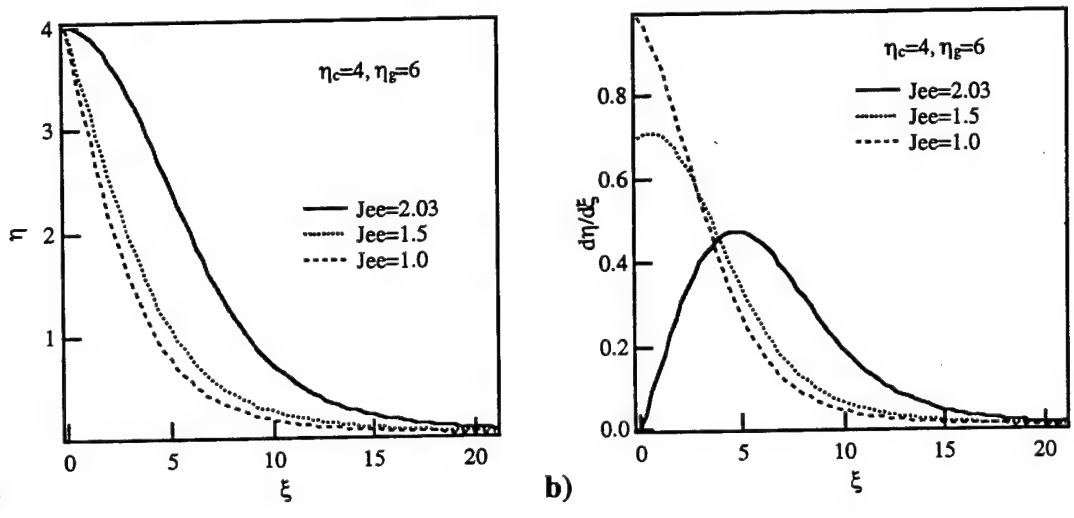

Figure 5.6 a, b Potential (a) and electric field (b) profiles for different emission currents in the cathode sheath.

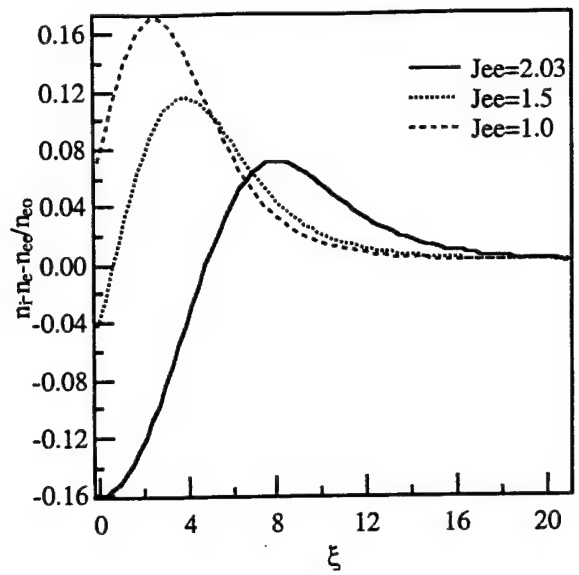

Figure 5.7 Charge density profiles in a planar cathode sheath with η_c=4 and η_g=6.

In the Hall thruster configuration where the cathode is external to the thruster, the sheath dimensions are comparable to the cathode dimensions, which are assumed to be 1x1 cm. Therefore, the sheath would be better represented by a cylindrical geometry that considers some radial electron beam expansion. In the tether environment, plasma densities are so low that the cathode sheath dimensions can be much larger than the cathode dimensions, necessitating the use of a sheath model that is more spherical in geometry with a $1/r^2$ change in number densities across the sheaths. A comparison of the results of the models of three different sheath geometries is presented in Table 5.3. The planar model can be used to predict lower limits on the cathode current. The spherical model should predict the upper limits on the current that can be emitted from the cathode because this sheath configuration will assume the highest negative space-charge neutralization at the cathode surface. The ion collection area of the sheath boundary will be much larger with a spherical geometry than with a planar or cylindrical geometry. It is uncertain, however improbable, that virtual cathode formation can not supply the same advantage to electron beam emission as a spherical sheath geometry.

Table 5.3 Space-charge limited currents predicted by the planar, cylindrical, and spherical sheath models in normalized units.

geometry	ξ_c	ξ_{sh}	η_c	η_g	η_o	J_{eemax}
planar		20.0	4	6	0.85	2.0
cylindrical	40	54.0	4	6	0.87	2.9
cylindrical	20	32.0	4	6	0.87	3.5
cylindrical	10	19.4	4	6	0.85	4.0
cylindrical	4	13.0	4	6	0.85	6.6
cylindrical	1	8.8	4	6	0.80	15.3
cylindrical	1	18.4	20	6	0.55	9.8
spherical	40	48.6	4	20	1.34	31.0
spherical	40	47.0	4	6	1.34	6.5
spherical	20	27.0	4	6	1.22	7.4
spherical	10	17.0	4	6	1.10	9.9
spherical	4	10.4	4	6	0.95	17.6
spherical	1	6.8	4	6	0.76	70.0
spherical	0.4	5.4	4	6	0.65	168.0

The environment investigated for the results shown in Table 5.3 was that of a Hall thruster with T_e=5 eV so that V_c=20 V and V_g=30 V. V_c was assumed to be 20 V because it is common for hollow cathodes to float 20 V below the local plasma potential to retard the collection of plasma electrons. The sheath and cathode geometry strongly influences the results of the models, as data in Table 5.3 show. The planar model predicts lower current density limits. The cylindrical and spherical geometry sheath models predict current limits that approach the planar model results for large cathode configurations.

Results from the sheath models for cathodes operating in the external cathode position of a Hall thruster are presented in Table 5.4 for different sheath geometries. While cathodes can emit much higher current densities into spherical sheaths, spherical sheath formation requires that $r_c \ll r_{sh}$. With such small emitting cathode areas, total cathode current is sacrificed for greater current density as shown in Table 5.4. The area of the cathode is determined by assuming a rectangular (cylindrical sheath) or square (spherical sheath) and that one-half of the length of one side is r_c. The most favorable

cathode configuration for this application is a ~1.2 cm cathode with j_{ee} at 82 mA/cm. Therefore, with a 1.2 cm cathode length, I_{ee} will be 98 mA. Many of these cathodes could be used to provide a few Amperes of current required by a 1.35 kW system or 1-2 could be used for a 50 W thruster.

Table 5.4 Field emission current limitations predicted by the sheath model in dimensional parameters for planar, cylindrical, and spherical geometries for the Hall thruster environment with an external cathode. V_g is at 30 V and V_c is at 20 V.

geometry	ξ_c	r_c (mm)	j_{ee} (A/cm^2)	j_{ee} (mA/cm)	I_{ee} (mA)
planar			34		
cylindrical	10	6	68	82	
	4	2.4	112	54	
	1	0.6	260	31	
spherical	4	2.4	299		69
	1	0.6	1190		17

Space-charge current limitations are also predicted using the sheath model to study a cathode emitting from an electrodynamic tether system into a Low Earth Orbit (LEO) environment. Results with non-dimensional parameters for a spherical sheath are shown in Table 5.5. This table shows that the sheath dimensions are so large that the sheath geometry could be spherical even when ξ_c is 10. In the tether environment T_e is 0.1 eV, therefore η_g is 300 and η_c is 200 when V_g is 30 V and V_c is 20 V. The current density emitted by the cathode greatly increases with decreasing cathode dimensions. Table 5.6 shows how the total current emitted by the cathode is affected by the size of the cathode. Smaller cathodes are capable of larger current densities, however, the emitting area is also considerably smaller. Therefore, there is no inherent advantage in reducing cathode size in terms of emission characteristics. Also shown in Table 5.5 and Table 5.6 is the current gain attributable to increases in the energy of the emitted electrons by increasing the potential of the gate electrode. Increasing the gate electrode from 30 V up to 100 V only increases the current by a factor of ~2. To satisfy the ~2 A current

requirements of the tether application, several hundred cathodes will be required according to these model results.

Table 5.5 Field emission current limitations predicted by the sheath model in normalized parameters for a spherical sheath in a tether environment where T_e is 0.1 eV.

ξ_c	ξ_{sh}	η_c	η_g	r_{io}	J_{eemax}
10	64	100	100	0.53	40
10	100	200	200	0.52	91
9	103	200	300	0.52	145
5	100	200	300	0.52	430
1	97	200	300	0.52	8650
1	99	200	400	0.52	10400
1	101	200	600	0.52	13400
1	104	200	1000	0.52	18400
1	109	200	10000	0.53	63550
1	60.5	100	300	0.53	4925
1	37	50	300	0.55	2750
1	38	50	1000	0.56	5350
1	38.5	50	10000	0.56	17400

Table 5.6 Field emission current limitations predicted by the spherical sheath model for the tether environment.

ξ_c	r_c(mm)	V_c (V)	V_g (V)	I_{ee} (mA)
5	16.5	20	30	7.0
1	3.3	20	30	5.6
1	3.3	20	40	6.8
1	3.3	20	60	8.8
1	3.3	20	100	12.0
1	3.3	20	1000	41.5
1	3.3	10	30	3.2
1	3.3	5	30	1.8
1	3.3	5	100	3.5
1	3.3	5	1000	11.3

Unfortunately, these modeling results have yet not been substantiated by experimental observations. The trends observed are consistent with modeling results obtained in other sheath studies that increasing sheath potential increases the size of the sheath, and that

increasing the electron current emitted from the cathode increases the size of the sheath.[57] The enormous size of the cathode sheath in the tether environments was especially surprising; however, the CHARGE 2 sounding rocket experiment coupled with NASCAP/LEO computer simulations[85] did predict sheath dimensions similar to the dimensions predicted by the sheath model discussed in this chapter.

The sheath structure around a rocket payload charged up to 460 V negative to the ambient ionospheric plasma at 245 km altitude was studied experimentally and by computer simulations of the CHARGE 2 sounding rocket experiment. The payload was split into two sections connected by a conducting tether. The mother section was biased to potentials as much as 450 V below the daughter section, which was close to ambient plasma potential. The mother section carried four floating probes on a boom, which extended out from the spacecraft with probes at 25, 50, 75, and 100 cm. In this investigation, electron number densities were assumed to be $4x10^4$ cm^{-3}, electron temperatures 0.086 eV, and ion temperatures 0.1 eV. The sheath boundary in that study was defined at -0.4 V. Theoretical and experimental results showed that the cylindrical sheath thickness was 60 cm when the spacecraft potential was –30 V. The cylindrical sheath model discussed in this chapter cannot be used to estimate sheath thickness without the electric field at the cathode surface being known *a priori*; however, the planar sheath model could be used, assuming zero electron emission, and the thickness of the sheath could be adjusted for a cylindrical sheath. The planar sheath model was used to predict a sheath thickness of 79 cm if the sheath boundary was defined at –0.4 V and the sheath voltage was –30 V with T_e at 0.086 eV and n_{eo} at $4x10^4 cm^3$. This correlation was fairly good considering that a planar sheath model will over-predict the thickness of a cylindrical sheath. A cylindrical sheath around a negatively charged electrode requires a smaller thickness than a planar sheath because of the amount of positive charge contained within the sheath volume. A cylindrical sheath with a thickness of 68 cm will contain the

same volume of charge as a planar sheath with a thickness of 79 cm. The sheath model effectively predicted the sheath dimensions in this case with an error of 13%.

The modeling results discussed in this chapter were also compared to the results of a three-dimensional particle-in-cell simulation model developed by Wang[86]. The one-dimensional sheath model can be used to obtain almost immediate results, while the three-dimensional PIC model is computationally expensive. The Wang simulation model considers three-dimensional beam expansion, determines the true structure of the sheath, and can evaluate the effect of virtual cathode formation on space-charge limited electron emission into a plasma. His model was originally developed to study virtual anode formation in ion beam emission in space[87] and was later modified to investigate electron beam emission into a plasma.[86] It is capable of resolving interactions between beam electrons and ambient plasma with a full particle, three-dimensional electrostatic PIC code, which follows both the beam electrons and the plasma ions and electrons.

Results of the three-dimensional PIC simulation model and the one-dimensional sheath model were compared for scenarios with cathodes operating in thruster and tether environments. The results from the Wang model for a FE cathode operating in a thruster environment are shown in Table 5.7. The current emitted from the cathode is I_{ce}, while the current transmitted through the sheath is I_{trans}. The minimum potential in the cathode sheath with respect to the potential at the sheath boundary, the virtual cathode potential, is ϕ_{min}. Note how a virtual cathode potential at –50 V in the sheath does not prevent the total emitted current from escaping through the sheath. However, with I_{ce} at 52 mA/cm^2 in this case, a virtual cathode forms with a potential at –75 V which limits the transmitted current to 34 mA. In this scenario, 18 mA would be collected by the cathode gate electrode, which is intolerable with FEA cathodes. Some of this current will be absorbed by the flux of ions to the gate electrode; however, the current to this thin film gate electrode is limited to only ~10-20 μA. The electron emission current density upper limit predicted by the Wang model in this cathode and plasma configuration is between 125

and 236 mA/cm^2. The current density limitations predicted by the 1-D sheath model of planar, cylindrical, and spherical sheath geometries are 34, 112 and 299 mA/cm^2, respectively. The Wang model showed that virtual cathode formation does not provide a current advantage greater than that provided by the ideal spherical sheath geometry, for a planar cathode configuration. The 3-D Wang model predicted upper limits on the emission current density that were between the upper and lower limits predicted by the 1-D sheath model, closest to the current limit predicted using the cylindrical sheath model.

Table 5.7 Current limitations and virtual cathode potentials predicted by the Wang simulation model for a field emission cathode in a Hall thruster environment with $r_c = 4\,\lambda_D$, V_g at 30 V, ϕ_c at –20 V, T_e at 5 eV, and n_{eo} at 8×10^8/cm^3.

j_{ee} (mA/cm^2)	I_{ee} (mA)	Φ_{min} (V)	I_{trans} (mA)	I_{trans}/I_{ee}
34	7.5	-20	7.5	1
84	18.5	-34	18.5	1
125	27.5	-50	27.5	1
236	52	-75	34	0.67

Wang also used his 3-D PIC model to study electron emission from FE cathodes into a space tether environment. The cathode and spacecraft potential configuration affects the emission current limitations; however these details were not investigated with this model. In the configuration investigated, the spacecraft was at the cathode potential. The results are shown in Table 5.8. In this case, a current density of 13 mA/cm^2 is unacceptable because of the prohibitively high current that will be collected by the gate electrode. The current density upper limit, as predicted by that model is between 6.5 and 13 mA/cm^2. The upper limit on the current density predicted by the spherical 1-D sheath model is 13 mA/cm^2. Considering virtual cathode formation in cathode sheaths with a 3-D PIC model leads to current density limit estimates below those made by the 1-D spherical sheath model. According to the 3-D PIC model, the1-D spherical and planar

sheath models do provide upper and lower limits on the electron current density that can be expected from planar FE cathodes in plasma environments, which was the objective for the simple model development. The advantage of the 1-D sheath model is that results can be obtained almost immediately. The 3-D PIC model is computationally expensive, requiring approximately two hours to execute. To study the effect of the potentials of surrounding electrodes, the interaction of multiple electron beams, and to obtain more accurate predictions of the emission current limitations from FE cathodes in plasma environments, the 3-D PIC simulation model is required.

Table 5.8 Current limitations and virtual cathode potentials predicted by the Wang simulation model for a field emission cathode operating in a tether environment with $r_c = \lambda_D$, V_g at 30 V, ϕ_c at –20 V, T_e at 0.1 eV, and n_{eo} at $5 \times 10^5/cm^3$.

j_{ee} (mA/cm^2)	I_{ee} (mA)	Φ_{min} (V)	I_{trans} (mA)	I_{trans}/I_{ee}
6.5	2.86	-42	2.86	1
13	5.7	-49	4.9	0.86
26	11.4	-60	5.8	0.51

This chapter presented a sheath model which is capable of predicting upper and lower limits on the emission current density that can be expected from a FE cathode in plasma environments. It can be used to estimate the maximum and minimum number of cathodes required to supply the desired current in a plasma environment. This model was used to study the effects of initial electron energies, eV_g, gate electrode potential below the potential at the plasma sheath boundary, ϕ_c, and r_c on emission current limitations. Increasing V_g increases the j_{ee} limit. While decreasing r_c increases j_{ee}, I_{ee} from the cathode decreases. The optimal V_c value depends on the cathode operating configuration and environment; j_{ee} could increase or decrease with increasing V_c.

The model was used to assess the compatibility of FE cathode and electric propulsion and tether systems. Modeling results showed that the FE cathode current

should not be space-charge limited within the required current regime if operated in the discharge chamber of an ion engine or internal position of a Hall thruster. In the external position of a Hall or ion thruster, a cathode area of 40 cm^2 is required if V_g is 30 V for 4.5 A. This current could be emitted from a segmented cathode ring around the thruster. Cathode area can be decreased by increasing V_g. Much smaller cathode areas are required for smaller power systems. The size of the cathodes required is not prohibitively large. The results of the sheath model for some possible cases show that the tether application will require a prohibitively large number of cathodes, or cathode area, if electrons are emitted at 30 eV. A reasonable number of cathodes is required if V_g is 1000 V. However, it is not possible to operate FEA cathodes with V_g at 1000 V, because of the breakdown strength of the insulator material between the gate electrode and tip. Acceleration of the electron beam from 30 eV up to 1000 eV could occur downstream of V_g by another electrode. The CLAIR structure disclosed in Appendix B could be used to decouple the electron energy from the gate electrode potential and accelerate the electron beam by an electrode downstream of the gate electrode.

CHAPTER 6

CONCLUSIONS

The objective of this thesis was to gain a better understanding of the effects of EP system environments on FE cathode performance, address compatibility issues, and develop models to predict performance limitations which can then be used in cathode design and accelerated life tests. Sheath models developed were also used to study space-charge limitations of FE cathodes in tether environments. The results of this research, possible cathode configurations for the thruster and tether applications of interest, and recommendations for future research are discussed in this concluding chapter.

6.1 Summary of Major Results

Initial cathode experiments in xenon environments were based on experimental results obtained in research laboratories at SRI International and MCNC and cathode environment characterization of the PEPL-70. The results obtained from experiments with single HfC and ZrC cathode tips in ~10^{-6} Torr Ar and O_2 environments showed that these materials are incredibly robust. The cathodes were not destroyed in hostile environments; often performance improved from the high-pressure exposures with operating voltages at a few thousand volts. Experiments with Mo and Si FEA cathodes, and carbon film FE cathodes showed that no work function increases resulted from xenon exposure. The efficiency of these cathodes was not affected by increases in pressure up to 2×10^{-5} Torr until the tips were damaged by ion bombardment. Si and Mo FEA

cathodes were operated in xenon environments with pressures as high as 10^{-5} Torr for several hours without measurable performance degradation. Experimental results showed that FEA cathode performance in xenon pressure environments similar to Hall thruster environments is very sensitive to operating voltages. Energy threshold values for sputtering Mo and Si targets by xenon ions were determined to be much lower than the model developed by Yamamura et al. predicted. Experimental results also showed that the SRI International cathode, fabricated on a high resistivity wafer, was more resistant to arcing in high-pressure environments than other cathode configurations tested. The carbon film cathode was incredibly robust, showing no performance degradation during several hours in $2x10^{-6}$ Torr of xenon with the gate electrode at 800 V. This cathode turned on no differently in $2x10^{-6}$ Torr of xenon and in UHV environments.

Combining the performance degradation model with experimental results enabled much more accurate predictions of E_{th} than ever before available. The E_{th} for a Mo target being sputtered by Xe ions is now estimated at 39 eV as opposed to 49 eV predicted by the sputter yield model. The E_{th} for a Si target being sputtered by Xe ions is estimated at 48 eV as opposed to 91 eV as predicted by the sputter yield model. These results are consistent with experimental observations of gate electrode thresholds for sputtering and measured sputter yield values. Predictions of performance degradation rates in xenon environments correlate well with experimental results. Using the improved estimates for E_{th}, this model can now be used to estimate the performance degradation rates of any Mo or Si FEA cathode operating in neutral xenon environments at any pressure. Operating voltages are limited to values near E_{th}; the operating voltage limits depend on the cathode configuration. This model was also used to determine the effect of the CEX ion population on the cathode performance degradation rate. It was shown that this CEX ion population is so detrimental to the cathode performance that upper limits on operating voltage were further reduced by 20 V when this ion population is bombarding the field emission microtips. In this situation, the population of ions generated locally is

negligible; CEX ions dictate performance degradation rates. To meet cathode lifetime requirements of greater than 100 hours in $2x10^{-5}$ Torr of xenon, Si cathodes will be limited to operating voltages below 30 V and Mo cathodes will be limited to operating voltages below 20 V. These values will increase with decreasing pressure from $2x10^{-5}$ Torr. Even at these voltages, current limiting cathode architectures will be required to prevent catastrophic arcing between the tips and gate electrodes.

Modeling of space-charge current limits in the applications of interest showed that this issue could significantly limit the performance of FE cathodes in thruster and tether environments. It was shown that cathode dimensions and environment play a major role in determining their performance limitations because they affect the configuration of the sheath. Planar sheath modeling results showed that cathodes emitting electrons into the discharge chamber of an ion thruster will have a lower current density limit which is >8 A/cm^2, and exceeds the current density requirements in this application. If positioned in the center of the PEPL-70 Hall thruster, a field emission cathode emitting electrons at 30 eV will have a space-charge current density limit greater than ~1.7 A/cm^2, independent of cathode dimensions, as determined by the planar model. A 1.2 x 1.2 cm cathode in the external position of a Hall thruster or ion engine emitting electrons at 30 eV should be able to emit near ~68 mA/cm^2, assuming a 1/r electron beam expansion in the cathode sheath. Either a few cathode arrays could be used in the center of the thruster to provide up to 4.5 A or a segmented cathode ring could be used in the external cathode position of a Hall thruster with a much larger area. The external cathode position will be required for small and microscale propulsion systems. Current requirements for small and microscale propulsion systems will be less than a few hundred milliamperes so that a cathode area of a few cm^2 will suffice. If electrons are emitted at 100 eV, the lower limit on current density for the 1.2 x 1.2 cm cathode with V_g at 100 V and ϕ_c at 20 V should be ~120 mA/cm^2. Of course, operating voltages limit cathode lifetime. While silicon cathodes are limited to operation with gate electrode voltages no higher than 30 V,

molybdenum cathode gate electrodes are limited to potentials no higher than 19 V. If electrons must be emitted at higher energies, the electron energy must be decoupled from the potential of the gate electrode. CLAIR would provide additional electrodes so that electron acceleration up to 100 eV or higher would occur downstream of the gate electrode.

In a tether environment, much higher cathode operating voltages will be tolerated because of low pressures; however, there are fewer ions to neutralize the negative space-charge of the electron beam so that the space-charge current limits will be significantly lower than the limits in the thruster environment. The current density limits in this environment are significantly affected by the size of the cathode. Only a few operating configurations were explored. A 6.6 x 6.6 mm cathode should not be able to emit more than 5.6 mA if ϕ_c is 20 V and V_g is 30 V, according to the spherical sheath model. If a current of 2 A is required, then several hundred cathodes will be necessary to supply that current. This configuration of cathodes may be prohibitively complicated. With the gate electrode at 100-1000 V, it is possible that fewer than 100 cathodes will be required to emit 2 A in some operating configurations. It was also shown that increasing ϕ_c also increases the emission current from a tether system.

Cathode dimensions for the applications discussed must consider both space-charge limitations and cathode performance at the voltages limited by lifetime requirements. Even though current densities >1.7 A/cm^2 are possible in the Hall thruster internal position, that performance is very optimistic for a cathode that must survive for >100 hours. If the cathode microtips are not shielded from CEX ions, then Si and Mo cathodes will be limited to operating voltages ~30 and ~19 V respectively. Such low operating voltages severely limit the current/tip so that the array of microtips could be prohibitively large to provide the required current. The size of the cathode and number of microtips required in the different applications depends on the packing density of the microtips, ϕ_w, r_t, r_g, and Δs. Results presented in Chapter 4 show how the cathode

parameters affect the number of tips required for the desired current and operating voltages limited by cathode lifetime. Some possible cathode configurations are suggested in the next section for the applications of interest.

6.2 Recommended Cathode Designs

The number of microtips or thin film cathodes necessary to emit the required current depends on the environment and cathode configuration and materials. The environment places lower limits on operating voltages, as discussed in Chapters 3 and 4, and current densities, as discussed in Chapter 5. The cathode materials and dimensions also affect the number of cathodes required and sizes of the arrays as discussed in Chapter 4. The design of FE cathodes for the applications discussed requires careful consideration of the environment, current and lifetime requirements for the applications, and performance of available cathodes. The modeling tools developed for this dissertation can be used to optimize the cathode configuration and electrode potentials for the application.

The models developed were used to suggest cathode configurations that would satisfy the requirements of the applications discussed. The limits on current density were determined from the sheath model. Then data presented in Table 4.5 and Table 4.6 were used to determine which cathodes could supply that current density at sufficiently low voltages to ensure cathode lifetimes greater than 100 hours without CLAIR to retard CEX ions. One-half of the side length of a square cathode is given as r_c. The cathode packing density was assumed to be $10^8/cm^2$. Other cathode parameters were assumed to be $\Delta s=2$, $r_g=1000$ Å, and $r_t=40$ Å. This cathode configuration is not overly optimistic. Typically, cathode parameters are not this good, however, higher packing densities and lower r_t, r_g, and Δs have been demonstrated. Cathode configurations suggested with these assumed parameters are shown in Table 6.1. Cathode configurations are also suggested at higher

operating voltages assuming a CLAIR structure is used to improve cathode lifetime at higher voltages. Cathodes with higher packing densities and smaller Δs, r_t, and r_g will require smaller cathode arrays or fewer arrays to supply the required current than configurations suggested in Table 6.1 and Table 6.2. The number of cathodes can be scaled down for much smaller thrusters to meet lower current requirements. Modeling results suggest that Mo cathodes could not be used without a CLAIR structure, with the assumed parameters, because they could only supply the required current from reasonable cathode areas with a gate electrode voltage that is at least at 42 V. In the cases where V_g is 30 V, Si, HfC, or ZrC cathodes could provide the currents required from the maximum cathode size noted in Table 6.1.

Table 6.1 Recommended number of cathodes, operating voltage, cathode material, and emitting area required in different applications if packing density is $10^8/cm^2$, Δs= 2, r_g=1000, and r_t=40.

Application	I (A)	r_c (cm)	V_g (V)	I/cathode (mA)	$N_{cathodes}$	Area (cm^2)	Material
PEPL-70-ext.	4.5	0.6	30	>68	<66	<95	Si,HfC,ZrC
PEPL-70-int.	4.5	1.5	30	>4500	1	<9	Si,HfC,ZrC
Ion engine-int.	<6	0.5	30	>6000	1	<1	HfC,ZrC
Tether	2	0.33	30	<4.3	>460	>460	Mo,Si,HfC,ZrC
Tether	2	0.33	100	<9.1	>220	>220	Mo,Si,HfC,ZrC

Table 6.2 Recommended number of cathodes, operating voltage, cathode material, and emitting area required in different applications if packing density is $10^8/cm^2$, Δs= 2, r_g=1000, r_t=40, and CLAIR is used.

Application	I (A)	r_c (cm)	V_g (V)	I/cathode (mA)	$N_{cathodes}$	Area (cm^2)	Material
PEPL-70-ext.	4.5	0.6	100	>136.0	<33	<47.5	Mo,Si,HfC,ZrC
PEPL-70-int.	4.5	1.5	42	>4500	1	<9	Mo,Si,HfC,ZrC
Tether	2	0.33	100	<9.1	>220	>220	Mo,Si,HfC,ZrC
Tether	2	0.33	1000	<41.0	>49	>21	Mo,Si,HfC,ZrC

6.3 Recommendations for Future Research

This research topic is rich and has only begun to be explored. This thesis is the first in a series of studies investigating the compatibility of FE cathodes and EP systems and tethers. Many of the experiments were preliminary. More of the same experiments at low operating voltages are recommended to support the E_{th} estimates. The effect of anode potential on performance degradation rates with low gate electrode potentials in higher-pressure environments should be further investigated. HfC and ZrC cathodes should be tested in xenon environments and E_{th} should be determined for these materials also.

Cathode configuration improvements have been prescribed to successfully merge these technologies. Cathodes should have smaller dimensions and more microtips in the cathode arrays with better uniformity than those cathodes tested in this study. The next step is to fabricate the recommended Mo, Si, HfC, and ZrC FEA cathodes. Cathodes with VECTL architectures are required to prevent arcing between tips and gate electrodes and maximize cathode efficiency. These cathodes should be tested at current levels ~1 mA in xenon environments, and life tests should be conducted to show which field emission cathodes can operate in $2x10^{-5}$ T for ~100 hours and validate theoretical results. I-V traces in UHV environment, cathode geometry, and work function are now sufficient to estimate cathode lifetime in xenon environments.

Carbide cathodes are incredibly robust; however, they operate at high voltages and low efficiencies. The gate electrode and carbon film should be microfabricated as an integrated structure to significantly reduce operating voltages and current collected by the gate electrode.

CLAIR should be developed to improve the compatibility of FEA cathodes and EP systems. The multi-electrode structure must be microfabricated and tested at the necessary operating voltages. Microtips must then be deposited in the back of the

channels in CLAIR. CLAIR should be tested in UHV environments, xenon environments, and then with EP systems.

Field emission cathodes must be tested with EP systems. Initially they will share current with hollow cathodes to evaluate lifetime and space-charge limitations in a thruster environment. Eventually, these cathodes could provide the total discharge current. New start-up sequences must be developed for FE cathodes and Hall and ion thrusters. In the typical start-up sequences, the propellant breakdown into a plasma is initiated at the cathode. This start-up could destroy the delicate cathodes. If field emission cathodes are used, propellant breakdown should be initiated at the anode.

Another issue to explore is the deposition of vacuum chamber material on the cathodes. High energy ion beams emitted from the thruster sputter material off of the vacuum chamber walls, which could then redeposit on the cathode, shorting the tips to the gate electrodes. Cathode positioning could play an important role in the effect of this issue on cathode lifetime.

Field emission cathodes must also be tested in simulated LEO environments. Modeling results of space-charge current limits must be validated experimentally. The modeling results predict very large cathode sheaths in LEO environments. Plasma potential measurements of space-charge limited currents in a simulated LEO environment will determine the accuracy of the sheath modeling results.

6.4 Other Applications

There are several other applications of the results of this research including those discussed in the introduction and throughout this thesis. These cathodes could be used for spacecraft discharging to control the potential of different surfaces.[88] FE cathodes could also be used with Field Emission Electric Propulsion (FEEP) systems to neutralize cesium ion beams. Because cesium ions are accelerated though several keV, more robust

cathode configurations are recommended, like the carbon film cathodes. It has been proposed to use FE cathodes as pressure sensors.[89] The models developed in this thesis can be used to design these sensors and estimate lifetime. The indirect methods used to determine E_{th} for sputtering of Mo and Si by xenon ions could be applied to experimentally determine these values for other FEAC materials.

APPENDICES

APPENDIX A

NOMENCLATURE

a_{fn}	Fowler-Nordheim term ($e(V\text{Å})^2/fs$)
A_{FN}	Fowler-Nordheim I term (A/V^2)
a_o	Bohr radius (Å)
b	term in radius distribution factor for cathode
b_{area}	area factor (Å^2)
b_{fn}	Fowler-Nordheim term (eV/Å)
B_{FN}	Fowler-Nordheim I term (V)
c	speed of light (Å/fs)
c_o	term in radius distribution factor for cathode
d	atomic spacing (nm)
e	electron charge (C)
E	ion energy (eV)
E_{th}	energy threshold for sputtering (eV)
F_{tip}	electric field on axis of the microtip structure (V/cm)
$\hbar$	Plank's constant (eV-fs)
I_a	current collected by the anode (A)
I_d	Hall thruster discharge current (A)
I_e	field emission current (A)
I_{ee}	cathode current (A)
I_f	final cathode current after 100 hour xenon exposure (A)
I_g	current collected by the gate electrode (A)
I_o	initial cathode current (A)

I_{tip}	current emitted from a single microtip structure (A)
I_{trans}	current transmitted through the sheath (A)
J	ion current density measured by the Faraday probe (A/cm^2)
j_e	plasma electron current density (mA/cm^2)
j_{ee}	electron beam current density (mA/cm^2)
J_{ee}	normalized electron beam current density
J_{eemax}	normalized upper limit on electron beam current density
J_{FN}	Fowler-Nordheim field emission electron current density (A/cm^2)
k	Boltzmann constant (J/K)
k	electric field factor
K	term in sputter yield model
$\dot{m}$	mass flow rate of propellant (mg/s)
M_I	incident ion atomic weight
M_{II}	target atom atomic weight
M_i	initial mass of a rocket with fuel (kg)
M_f	final mass of a rocket (kg)
n	number of ions striking the emitting area of a microtip during one second
n_e	plasma electron number density ($electrons/cm^3$)
n_{ee}	electron beam electron number density ($electrons/cm^3$)
n_{eo}	electron number density in the plasma ($electrons/cm^3$)
n_i	ion number density ($ions/cm^3$)
n_{io}	ion number density at the sheath boundary ($ions/cm^3$)
n_s	number of atoms sputtered from the emitting area of a microtip per second
N	neutral xenon number density ($atoms/cm^3$)
N_{tips}	number of tips in a field emission array cathode
P_{NPF}	xenon pressure measured by the NPF probe (Torr)
P_{tank}	xenon pressure measured by the vacuum gauge (Torr)

Q_i	cross-section for ionization (πa_o^2)
Q	term in sputter yield model
r	radial distance from microtip structure (cm)
r_i	radial position corresponding to ionization potential (cm)
r_c	cylindrical or spherical cathode radius (cm)
r_t	radius of curvature of a microtip structure (cm)
r_g	radius of aperture in gate electrode (cm)
r_m	maximum distance from a microtip within which an ion formed will hit the emitting area of the tip (cm)
r_s	radial position corresponding to the sputter threshold voltage (cm)
s_n	term used in sputter yield model
S_e	term used in sputter yield model
T	temperature (eV)
t_e	time to erode a single layer of atoms from a microtip emitting area (s)
T_e	electron temperature (eV)
T_N	thrust (N)
U_s	sublimation energy (eV)
V_a	anode voltage with respect to ground
V_d	discharge voltage of the Hall thruster (V)
v_{ee}	velocity of electrons emitted from the cathode (m/s)
V_g	potential of the gate electrode with respect to the cathode emitting surface (V)
v_i	ion velocity (m/s)
V_i	ionization potential (eV)
V_M	modulation voltage (V)
V_{max}	maximum voltage in an I-V trace (V)
V_{min}	minimum voltage in an I-V trace (V)

V_{pk}	peak voltage (V)
V_s	voltage corresponding to energy threshold for sputtering (V)
V_t	ion temperature (eV)
x	position from the cathode surface (m)
x_o	term in B_{FN}
Y	sputter yield (atoms/ion)
α	term in sputter yield model
β_c	microtip cone angle (radians)
β_g	field enhancement factor
δ	term in B_{FN}
Δs	tip radius spread factor
ε	term in sputter yield model
ε_o	permittivity of free space (F/m)
η	normalized voltage
η_c	normalized potential of gate electrode below the potential at the sheath boundary
η_{eff}	thruster efficiency
η_g	normalized potential between the gate electrode and cathode potential
η_o	normalized ion accelerating potential of the pre-sheath
λ_D	electronic Debye length (cm)
σ	half cone emitting angle of a cathode tip (°)
Σ	distribution factor associated with a spread in tip radii in a field emission cathode array
ϕ	potential with respect to the potential at the sheath boundary (V)
ϕ_o	accelerating potential of the sheath (V)

ϕ_c potential of the gate electrode with respect to the potential at the sheath boundary (V)

ϕ_τ electron emission half cone angle on a microtip (radians)

ϕ_w work function (eV)

ξ normalized position

ξ_c normalized spherical or cylindrical cathode radius

ξ_{sh} normalized position of sheath boundary

APPENDIX B

CLAIR

A Cathode Lens and Ion Repeller (CLAIR) has been designed to significantly improve the compatibility of Hall thrusters and FEA cathodes. The performance of this structure as a lens and ion filter was demonstrated using a particle-in-cell (PIC) code. CLAIR is a series of electrodes, similar to a gate electrode in FEA cathodes, in an einzel lens configuration that accelerates or decelerates an electron beam and retards charge-exchange (CEX) ion flow. The CLAIR configuration is shown in Figure B.1. Three electrodes are used in addition to the gate electrode. Electrode V_2 is at a high potential, ~100 V, to retard the flow of CEX ions to the microtip structures. V_3 is approximately 20 V below plasma potential. The other electrodes are biased with respect to V_3, depending on the cathode operating voltage and the accelerating or decelerating function of CLAIR. The thickness of the electrodes and insulators determines the lens optics. It is more difficult to focus the electron beam when it is being decelerated by CLAIR than when it is being accelerated. One possible cathode configuration is represented by the parameters shown in Table B.1. The design and performance of CLAIR was evaluated using MAGIC, a PIC code, that determined equipotential configurations and electron trajectories. MAGIC was developed by Mission Research, Inc. MAGIC output is shown Figures B.2 and B.3. The cathode was assumed to be a planar surface with electrons emitted uniformly from it with a velocity vector directed along the axis of CLAIR only. This cathode configuration should be capable of filtering out 60 eV ions and focusing the electron beam through the electrodes, as verified using MAGIC.

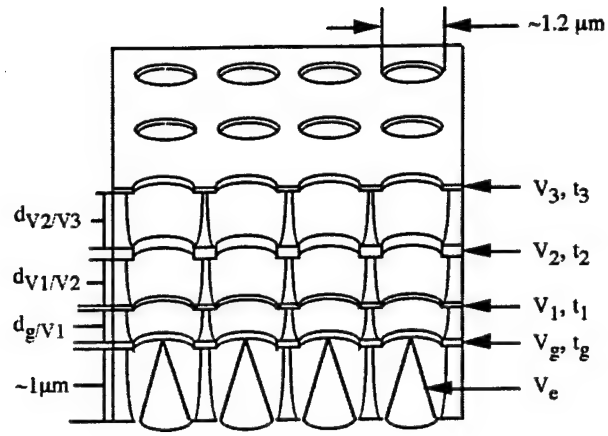

Figure B.1 Cathode Lens and Ion Repeller (CLAIR) congifuration.

Table B.1 Electrode potentials, thicknesses, and spacing for the CLAIR configuration simulated by MAGIC.

V_c (V)	V_g (V)	V_1 (V)	V_2 (V)	V_3 (V)	dg/v1 (μm)	dv1/v2 (μm)	dv2/v3 (μm)	$t_{1,3}$ μm)	t_2 (μm)	t_g (μm)
-40	10	-10	100	-20	0.4	0.8	0.8	0.1	0.3	0.25

CLAIR can be used to significantly increase the space-charge current limit on the cathode by increasing the energy of the electrons emitted from the cathode without increasing the potential of the gate electrode. CLAIR essentially decouples the electron energy from the gate electrode potential. It can significantly increase the lifetime of the cathode by filtering the CEX ions from the thruster out of the flux of particles bombarding the microtips. Without CLAIR, cathode gate electrode operating voltages are limited to values near 30 V. Ions generated between the gate electrodes and microtips and CEX ions, which sputter the microtip structures, are responsible for limiting the cathode lifetime. If CLAIR is used, operating voltages can be increased by approximately 20 V from the 30 V limit for Si cathodes. At this higher operating voltage, the current is increased by orders of magnitude from the same array of tips. With higher

voltage gate electrodes, space-charge current limits are increased for a specific current requirement, as shown in Figure 4.6.

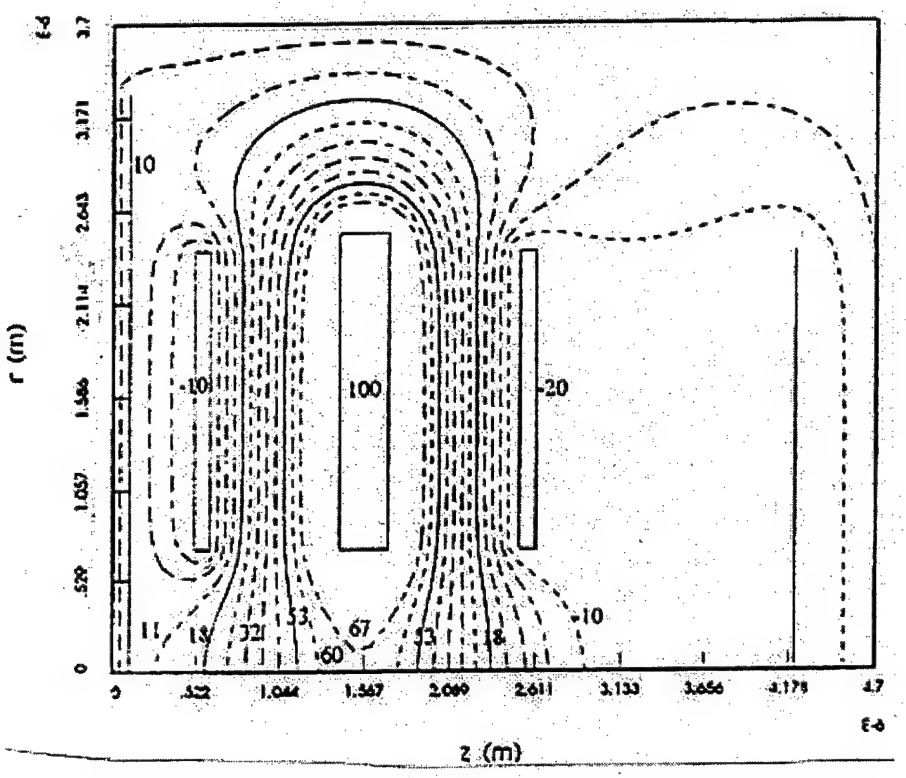

Figure B.2 Equipotentials predicted by MAGIC for the CLAIR configuration described in Figure B.1 and Table B.1.

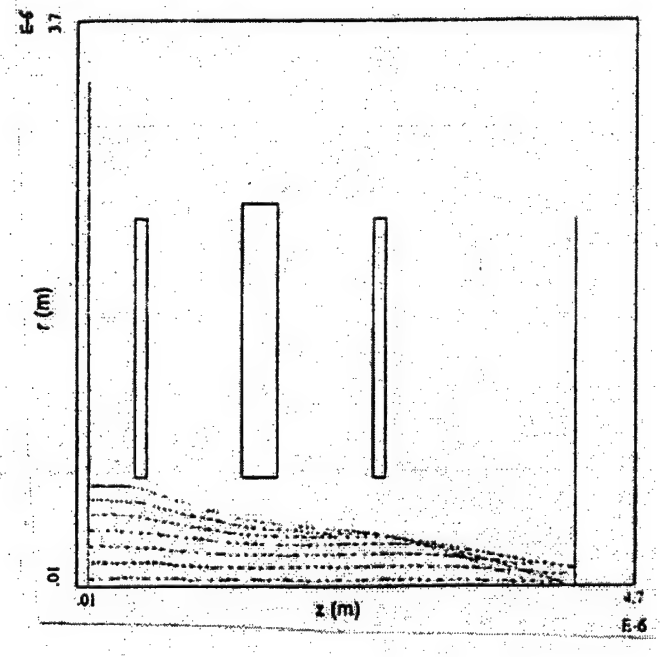

Figure B.3 Electron trajectories predicted by MAGIC for the CLAIR configuration described in Figure B.1 and Table B.1.

APPENDIX C

FEA Cathode Performance Degradation Model Macro

This macro is used in IGOR to calculate the performance degradation rate of FEA cathodes in xenon environments. The model uses pre-existing arrays for radius, Qiintxenon, and xenoneVi. The radius array has all of the radial positions (cm) used in the calculation of the ion flux to the microtips. Ionization cross-section data obtained from Brown are in the arrays Qiintxenon (cross-section) and xenoneVi (energy). The tim array is used to calculate the change in radius in time increments tim (hours). Those data arrays are given after the macro.

Macro calcIt ()

```
Silent 1
variable ag, phi, bc, Ntips, Vg, a, b, n, elect, vs, pressure, vt, d, yeti, rtmax
ag=10000        //(Å)
phi=3.5         //(eV)
bc=0.26         //(radians)
Ntips=16000
ds(0)=340
Vg =86          //(V)
YEti=.017       // sputter yield value for a Si target and xenon CEX ions
rt(0) =59.1     //initial effective tip radius (Å)
rtmax= (ds(0)+1)*rt(0)          //initial maximum tip radius
elect = 1.6022E-19              //(Coulombs)
pressure = 7E-6                 //(Torr)
vt= .03                 //(eV)
d = 3.13                //(Å)

variable Us, MI, MII, ZI, ZII, Que, eth, alpha, kay, lkay, i, ethmf
//duplicate/O rt Irtip, Irarray, Ftip, JFN, barea, bb, SIG, kc, bg, co, delr, ns, te
duplicate/O radius voltage, Quei, Sxesi,  epsilon, se, sn
duplicate/O radius dr, nsi, qydr
differentiate dr
n = 0
ns(n) =0
```

```
do
        ds(n) = rtmax/rt(n)-1
        kc(n)=1/54 *(86+ag/rt(n))*1/tan(bc)
        Ftip(n)=((pi/(ln(kc*ag/rt(n))))-(tan(bc))^2)*Vg/rt(n)
        a=(.008621/phi)*exp(9.246/phi^.5)          //Fowler-Nordheim a coefficient
        b=0.6421*phi^1.5              //Fowler-Nordheim b coefficient
        JFN(n)=a*Ftip(n)^2*exp(-b/Ftip(n))
        bg(n)= ((pi/(ln(kc(n)*ag/rt(n))))-(tan(bc))^2)/rt(n)
        barea(n)= 2*pi*rt(n)^2*(cos(bc))^2*(bg(n)*Vg)/(b+(sin(bc))^2*bg(n)*Vg)
        co(n)=(1/(pi*bg(n)*rt(n)))*((tan(bc))^2+bg(n)*rt(n))^2-1
        bb(n)=((co(n)*b+(3*co(n)+2)*bg(n)*Vg)/(bg(n)*Vg))-
        (co(n)*bg(n)*Vg/b)*(tan(bc))^2
        SIG(n)=(exp(ds(n)*bb(n))-1)/(ds(n)*bb(n))                    //=Σ
        Irtip(n) = barea(n)*JFN(n)*1.6E-4    //current from a single tip with r_t in Amperes
        Irarray(n) = Ntips*SIG(n)*barea(n)*JFN(n)*1.6E-4          //current in Amperes
        IrarrayuA = Irarray*1e6                //current in microamperes

        //calculate voltage as a function of radial distance from the tips (r in cm)
                rm(n) = rt(n)*1E-8*(vg/vt)^.3333
                vm(n) = vg*((rt(n)*1E-8/rm)-1)*((rt(n)/ag)-1)^-1
                voltage = vg*((rt(n)*1E-8/radius)-1)*((rt(n)/ag)-1)^-1

        //calculate sputter yield for the voltage corresponding to each radial position
        Us= 4.63
        MI=131.3
        MII=28.1
        Que= 0.78
        ZI= 54
        ZII= 14
        Ethmf = .53    //energy threshold multiplication factor
        Eth=(1.9 + 3.8*(MII/MI)^-1 + 0.134*(MII/MI)^1.24)*Us*Ethmf
        alpha = 0.08+0.164*(MII/MI)^0.4+0.0145*(MII/MI)^1.29
        Kay= 8.478*(ZI*ZII/((ZI^.66667 + ZII^.66667)^0.5))*(MI/(MI+MII))
        epsilon=(0.03255/(ZI*ZII*(ZI^.66667+ZII^.66667)^0.5))*
                (MII/(MI+MII))*voltage
        sn= 3.44*(epsilon^0.5)*ln(epsilon+2.718)/(1+6.355*(epsilon^0.5)+epsilon*
                (-1.708+6.882*(epsilon)^0.5))
        lkay= 0.79*(((MI+MII)^.66667)/(MI^.66667*MII^1.5))*
                (ZI^.66667*ZII^.5)/(ZI^.66667+ZII^.66667)^.75
        se = lkay*epsilon^1/2
        Sxesi = 0.42* alpha*Que*Kay*sn*(Us*(1+0.35*Us*se))^-1*
                (1-(eth/voltage)^0.5)^2.8

        //calculate te
        Interpolate/T=1/N=28/I=3/A=0/J=2/Y=Quei/X=voltage Qiintxenon /X=xenoneVi
```

```
        ns(n)=0
        i=0
                do
                        if (voltage(i) > vg )
                                voltage(i) = vg
                        endif
                        i=i+1
                while ( i < numpnts(nsi) )
        i=0
                do
                        if (voltage(i) > eth )
                                if (voltage(i) < vm(n))
                                qydr(i) =dr(i)*0.5*(Sxesi(i)*Quei(i)+Sxesi(i+1)*
                                        Quei(i+1))*8.79E-17
                                nsi(i) = (Irtip(n)/elect)*pinterp(n)*3.55E16*qydr(i)
                                ns(n)= ns(n) + nsi(i)
                                endif
                        endif
                        i=i+1
                while ( i < numpnts(nsi) )
//      nsti(n) = (2e-5/1.6e-19)*2*pi*rt(n)^2*1e-16*0.33*Yeti       //CEX ions
        nsti(n) = 0
        te(n) = pi/3600*2*cos(37*2*pi/360)*rt(n)^2/((d)^2*(ns(n)+nsti(n)))
        delr(n) = tim(n)*d/te(n)        //change in tip radius during time tim.
        rt(n+1) = rt(n) +delr(n)
n=n+1
while (n<numpnts(tim))
end macro
```

radius	xenonVi	Qiintxenon	tim
4.25e-07	12	0.118	0.1
4.5e-07	13	0.6	0.1
5e-07	14	1.12903	0.1
5.5e-07	15	1.45161	0.1
6e-07	16	1.77419	0.1
6.5e-07	17	2.05556	0.1
7e-07	18	2.24074	0.1
7.5e-07	19	2.42593	0.1
8e-07	20	2.64286	0.1
8.5e-07	30	4.45918	0.1
9e-07	40	5.10515	
9.5e-07	50	5.32886	
1e-06	60	5.55257	
1.1e-06	70	5.77629	

1.2e-06	80	6
1.3e-06	90	5.93333
1.4e-06	100	5.86667
1.5e-06	200	5.2
1.6e-06	300	4.8125
1.7e-06	500	4.0375
1.8e-06	700	3.2625
1.9e-06	900	2.4875
2e-06	1000	2.1
2.1e-06		
2.2e-06		
2.3e-06		
2.4e-06		
2.5e-06		
2.6e-06		
2.7e-06		
2.8e-06		
2.9e-06		
3e-06		
3.1e-06		
3.2e-06		
3.3e-06		
3.4e-06		
3.5e-06		
3.6e-06		
3.7e-06		
3.8e-06		
3.9e-06		
4e-06		
4.1e-06		
4.2e-06		
4.3e-06		
4.4e-06		
4.5e-06		
4.6e-06		
4.7e-06		
4.8e-06		
4.9e-06		
5e-06		
5.1e-06		
5.2e-06		
5.3e-06		
5.4e-06		
5.5e-06		
5.6e-06		

5.7e-06
5.8e-06
5.9e-06
6e-06
6.1e-06
6.2e-06
6.3e-06
6.4e-06
6.5e-06
6.6e-06
6.7e-06
6.8e-06
6.9e-06
7e-06
7.1e-06
7.2e-06
7.3e-06
7.4e-06
7.5e-06
7.6e-06
7.7e-06
7.8e-06
7.9e-06
8e-06
8.1e-06
8.2e-06
8.3e-06
8.4e-06
8.5e-06
8.6e-06
8.7e-06
8.8e-06
8.9e-06
9e-06
9.1e-06
9.2e-06
9.3e-06
9.4e-06
9.5e-06
9.6e-06
9.7e-06
9.8e-06
9.9e-06
1e-05
1.1e-05

1.2e-05
1.3e-05
1.4e-05
1.5e-05
1.6e-05
1.7e-05
1.8e-05
1.9e-05
2e-05
2.1e-05
2.2e-05
2.3e-05
2.4e-05
2.5e-05
2.6e-05
2.7e-05
2.8e-05
2.9e-05
3e-05
3.1e-05
3.2e-05
3.3e-05
3.4e-05
3.5e-05
3.6e-05
3.7e-05
3.8e-05
3.9e-05
4e-05
4.1e-05
4.2e-05
4.3e-05
4.4e-05
4.5e-05
4.6e-05
4.7e-05
4.8e-05
4.9e-05
5e-05
5.1e-05
5.2e-05
5.3e-05
5.4e-05
5.5e-05
5.6e-05

5.7e-05
5.8e-05
5.9e-05
6e-05
6.1e-05
6.2e-05
6.3e-05
6.4e-05
6.5e-05
6.6e-05
6.7e-05
6.8e-05
6.9e-05
7e-05
7.2e-05
7.3e-05
7.4e-05
7.5e-05
7.6e-05
7.7e-05
7.8e-05
7.9e-05
8e-05
8.1e-05
8.2e-05
8.3e-05
8.4e-05
8.5e-05
8.6e-05
8.7e-05
8.8e-05
8.9e-05
9e-05
9.1e-05
9.2e-05
9.3e-05
9.4e-05
9.5e-05
9.6e-05
9.7e-05
9.8e-05
9.9e-05
0.0001

APPENDIX D

Cathode Sheath Model Macro

This appendix presents IGOR macros used to calculate potential and electric field profiles in cathode sheaths assuming planar, cylindrical, or spherical cathode and sheath geometries. Poisson's equation is solved using a fourth order Runge-Kutta method.

Macro Planarsheath()

```
Silent 1
variable h, n, f, etav, Te,Vb, Vm, Vg, bk, mi, me, elec, neo, sqrtalf, je, ljip, ljee, Jip, Jee
variable etam, etag, etap, etab, etao, Vo, con1, con2, con3, con4, Vc, etac,ef, etabo
neo = 4E4
Te = 0.086
elec = 1.6E-19
bk = 1.38E-23
me = 9.11E-31
Vg = 5
ljee =1
Vc=30
llim=140
h=0.25          // step size in spatial position, ξ

je= neo*elec*100*(2*bk*Te*11600/me)^0.5

etag = Vg/Te
etac= Vc/Te
Jee = ljee/je
etao = (1+Jee*(etag+etac)^-0.5)/(2-Jee*(etag+etac)^-1.5)

exIII(0) = 0            // electric field at sheath boundary
etaIII(0)= etac         //potential at cathode surface


n=0
        do
                etav = etaIII(n)
                exIII(n) = exIII(0) +h*n
```

```
        ef = 4*Jee*((etag+etac-etav)^0.5 -(etag+etac)^0.5) +
                2*(exp(-etav)-1)+4*etao*(1+Jee*((etag+etac)^-0.5))*
                (((1+etav/etao)^0.5)-1)
        f = -(4*(Jee*((etag+etac-etav)^0.5 -(etag+etac)^0.5) +
                0.5*(exp(-etav)-1)+etao*(1+Jee*((etag+etac)^-0.5))*
                (((1+etav/etao)^0.5)-1)))^0.5
        kayIII1(n)= h*f
        etav = etaIII(n) + kayIII1(n)/2
        f =- (4*(Jee*((etag+etac-etav)^0.5 -(etag+etac)^0.5) +
                0.5*(exp(-etav)-1)+etab*(1+Jee*((etag+etac)^-0.5))*
                (((1+etav/etao)^0.5)-1)))^0.5
        kayIII2(n)= h*f
        etav = etaIII(n) + kayIII2(n)/2
        f = -(4*(Jee*((etag+etac-etav)^0.5 -(etag+etac)^0.5) +
                0.5*(exp(-etav)-1)+etao*(1+Jee*((etag+etac)^-0.5))*
                (((1+etav/etao)^0.5)-1)))^0.5
        kayIII3(n) = h*f
        etav = etaIII(n) + kayIII3(n)
        f = -(4*(Jee*((etag+etac-etav)^0.5 -(etag+etac)^0.5) +
                0.5*(exp(-etav)-1)+etao*(1+Jee*((etag+etac)^-0.5))*
                (((1+etav/etao)^0.5)-1)))^0.5
        kayIII4(n) = h*f

        etaIII(n+1) = etaIII(n) + 1/6*(kayIII1(n) + 2*kayIII2(n) + 2*kayIII3(n) +
                kayIII4(n))

        n= n+1
while (n<llim)
exIII(n) = exIII(0) +h*.i

//calculate charged particle number densities
ninoIII =(1+Jee*((etag+etac)^-0.5))*((1+etaIII/etao)^-0.5)
ni= (1+ljee*((Vg+Vc)^-.5)/(neo*elec*100*(2*elec/me)^.5))*(1+etaIII/etao)^-0.5
nenoIII= exp(-etaIII)
ne= exp(-etaIII)
neenoIII = Jee*(etag-etaIII+etac)^-0.5
nee= ljee/neo*((Vg+Vc-etaIII*Te)^-0.5)/(elec*100*(2*elec/me)^0.5)
netotIII= nenoIII+neenoIII
ntotIII = ninoIII - netotIII
ntot = ni-ne-nee

efieldIII = (4*(Jee*((etag+etac-etaIII)^0.5 -(etag+etac)^0.5) +
        0.5*(exp(-etaIII)-1)+etao*(1+Jee*((etag+etac)^-0.5))*
        (((1+etaIII/etab)^0.5)-1)))^0.5
efieldi= 4*etao*(1+Jee*(etag+etac)^-0.5)*(((1+etaIII/etao)^0.5)-1)
```

```
        efielde= 2*(exp(-etaIII)-1)
        efieldee= 4*Jee*((etag+etac-etaIII)^0.5 -(etag+etac)^0.5)

end macro
```

Macro Cylindricalsheath()

```
Silent 1
variable h, n, zrsh, llim, etac, etao, etag, ef, ef1, ef2, Jee, zrc, etav, efld, rad
h= 0.2          // step size in spatial position, ξ
zrsh=13         //normalized sheath radius,r_sh/λ_D
zrc=4           //normalized cathode radius, r_c/λ_D
llim=45
etac=4
etag=6
Jee=6.6
Make/N=46/D/O eta, efield, rr
eta(0) = 0
efield(0) = 0           //efield at sheath boundary
rr(0)= zrsh     //position of sheath boundary

etao=(1+Jee*(etag+etac)^-0.5*(zrc/zrsh))/(2-Jee*(etag+etac)^-1.5*(zrc/zrsh))
print "etao=", etao
n=0
        do
                etav= eta(n)
                efld=efield(n)
                rad= rr(n)
                ef= (1+Jee*(etag+etac)^-0.5*(zrc/zrsh))*(1+etav/etao)^-0.5*
                        (zrsh/rad)-Jee*(etag+etac-etav)^-0.5*(zrc/rad)-exp(-etav)
                ef1=efld
                ef2=ef-ef1/rad
                kay1(1)= h*ef1
                kay2(1)= h*ef2

                etav= eta(n)+0.5*kay1(1)
                efld=efield(n)+0.5*kay2(1)
                rad= rr(n)-h/2
                ef= (1+Jee*(etag+etac)^-0.5*(zrc/zrsh))*(1+etav/etao)^-0.5*
                        (zrsh/rad)-Jee*(etag+etac-etav)^-0.5*(zrc/rad)-exp(-etav)
                ef1=efld
                ef2=ef-ef1/rad
                kay1(2)= h*ef1
```

```
            kay2(2)= h*ef2

            etav= eta(n)+0.5*kay1(2)
            efld=efield(n)+0.5*kay2(2)
            rad= rr(n)-h/2
            ef= (1+Jee*(etag+etac)^-0.5*(zrc/zrsh))*(1+etav/etao)^-0.5*
                    (zrsh/rad)-Jee*(etag+etac-etav)^-0.5*(zrc/rad)-exp(-etav)
            ef1=efld
            ef2=ef-ef1/rad
            kay1(3)= h*ef1
            kay2(3)= h*ef2

            etav= eta(n)+0.5*kay1(3)
            efld=efield(n)+0.5*kay2(3)
            rad= rr(n)-h
            ef= (1+Jee*(etag+etac)^-0.5*(zrc/zrsh))*(1+etav/etao)^-0.5*
                    (zrsh/rad)-Jee*(etag+etac-etav)^-0.5*(zrc/rad)-exp(-etav)
            ef1=efld
            ef2=ef-ef1/rad
            kay1(4)= h*ef1
            kay2(4)= h*ef2

            n=n+1
            eta(n) = eta(n-1) +(1/6)*(kay1(1)+2*kay1(2)+2*kay1(3)+kay1(4))
            efield(n) = efield(n-1) +(1/6)*(kay2(1)+2*kay2(2)+2*kay2(3)+kay2(4))
            rr(n) = rr(n-1)-h

        while (n<llim)

        //calculate charged particle number densities in the sheath
        Duplicate/O efield ntot, nion,npelect,nbelect
        ntot = (1+Jee*(etag+etac)^-0.5*(zrc/zrsh))*(1+eta/etao)^-0.5*
                (zrsh/rr)-Jee*(etag+etac-eta)^-0.5*(zrc/rr)-exp(-eta)
        nion= (1+Jee*((etag+etac)^-0.5)*(zrc/zrsh))*(1+eta/etao)^-0.5*(zrsh/rr)
        npelect=Jee*(etag+etac-eta)^-0.5*(zrc/rr)
        nbelect=exp(-eta)
end macro
```

Macro Sphericalsheath()

```
Silent 1
variable h, n, zrsh, llim, etac, etao, etag, ef, ef1, ef2, Jee, zrc, etav, efld, rad
h= .2
```

```
zrsh=10.4
zrc=4
llim=32
etac=4
etag=6
Jee=17.6
Make/N=33/D/O eta, efield, rr

eta(0) = 0
efield(0) = 0
rr(0)= zrsh

etao=(1+Jee*(etag+etac)^-0.5*(zrc/zrsh)^2)/(2-Jee*(etag+etac)^-1.5*(zrc/zrsh)^2)

n=0
        do
                etav= eta(n)
                efld=efield(n)
                rad= rr(n)
                ef= (1+Jee*(etag+etac)^-0.5*(zrc/zrsh)^2)*(1+etav/etao)^-0.5*
                        (zrsh/rad)^2-Jee*(etag+etac-etav)^-0.5*(zrc/rad)^2-exp(-etav)
                ef1=efld
                ef2=ef-2*ef1/rad
                kay1(1)= h*ef1
                kay2(1)= h*ef2

                etav= eta(n)+0.5*kay1(1)
                efld=efield(n)+0.5*kay2(1)
                rad= rr(n)-h/2
                ef= (1+Jee*(etag+etac)^-0.5*(zrc/zrsh)^2)*(1+etav/etao)^-0.5*
                        (zrsh/rad)^2-Jee*(etag+etac-etav)^-0.5*(zrc/rad)^2-exp(-etav)
                ef1=efld
                ef2=ef-2*ef1/rad
                kay1(2)= h*ef1
                kay2(2)= h*ef2

                etav= eta(n)+0.5*kay1(2)
                efld=efield(n)+0.5*kay2(2)
                rad= rr(n)-h/2
                ef= (1+Jee*(etag+etac)^-0.5*(zrc/zrsh)^2)*(1+etav/etao)^-0.5*
                        (zrsh/rad)^2-Jee*(etag+etac-etav)^-0.5*(zrc/rad)^2-exp(-etav)
                ef1=efld
                ef2=ef-2*ef1/rad
                kay1(3)= h*ef1
                kay2(3)= h*ef2
```

```
            etav= eta(n)+0.5*kay1(3)
            efld=efield(n)+0.5*kay2(3)
            rad= rr(n)-h
            ef= (1+Jee*(etag+etac)^-0.5*(zrc/zrsh)^2)*(1+etav/etao)^-0.5*
                  (zrsh/rad)^2-Jee*(etag+etac-etav)^-0.5*(zrc/rad^2)-exp(-etav)
            ef1=efld
            ef2=ef-2*ef1/rad
            kay1(4)= h*ef1
            kay2(4)= h*ef2

            n=n+1
            eta(n) = eta(n-1) +(1/6)*(kay1(1)+2*kay1(2)+2*kay1(3)+kay1(4))
            efield(n) = efield(n-1) +(1/6)*(kay2(1)+2*kay2(2)+2*kay2(3)+kay2(4))
            rr(n) = rr(n-1)-h

        while (n<llim)

//calculate charged particle number densities
        Duplicate/O efield ntot, nion,npelect,nbelect
        ntot = (1+Jee*(etag+etac)^-0.5*(zrc/zrsh)^2)*(1+eta/etao)^-0.5*
                (zrsh/rr)^2-Jee*(etag+etac-eta)^-0.5*(zrc/rr)^2-exp(-eta)
        nion= (1+Jee*((etag+etac)^-0.5)*(zrc/zrsh)^2)*(1+eta/etao)^-0.5*(zrsh/rr)^2
        npelect=Jee*(etag+etac-eta)^-0.5*(zrc/rr)^2
        nbelect=exp(-eta)

end macro
```

BIBLIOGRAPHY

BIBLIOGRAPHY

[1] *Hydrazine Handbook* , technical handbook from the former Rocket Research Co.

[2] Marcucuccio, S., Giannelli, S., and Andrenucci, M., "Attitude and Orbit Control of Small Satellites and Constellations with FEEP Thrusters," IEPC 97-188, 25th International Electric Propulsion Conference, Aug. 24-28, Cleveland, OH.

[3] Garner, C. E., Brophy, J. R., Polk, J. E., and Pless, L. C., "A 5,739 Hour Cyclic Endurance Test of the SPT-100," AIAA-95-2667, 31st. AIAA/ASME/SAE/ASEE Joint Propulsion Conf., July 10-12, 1995, San Diego, CA.

[4] Patterson, M., Haag, T., Rawlin, V., and Kussmaul, M., "NASA 30-cm Ion Thruster Development Status," AIAA 94-2849, 30th AIAA/ASME/SAE/ASEE Joint Propulsion Conference, June 27-29, 1994, Indianapolis, IN.

[5] Zharinov, A. V., and Popov, Y. S., "Acceleration of Plasma by a Closed Hall Current," Soviet Physics-Technical Physics, vol.12, Aug. 1967.

[6] Guerra, L., and Joosten, K.,"Return to the Moon," Ad Astra, May/June 1994.

[7] Frisbee, R. H., Polk, J. E., Gallimore, A. D., Marrese, C. M., "Oxygen-Propellant Plasma Thrusters for Cis-Lunar Electric Propulsion Missions," AIAA 98-3994, 34th AIAA/ASME/SAE/ASEE Joint Propulsion Conference and Exhibit, July 13-15, 1998, Cleveland, OH.

[8] Mueller, J., "Thruster Options for Microspacecraft: A Review and Evaluation of Existing Hardware and Emerging Technologies," AIAA 97-3058, 33rd AIAA/ASME/SAE/ASEE Joint Propulsion Conference, July 6-9, Seattle, WA.

[9] Fleeter, R. "Microspacecraft," The Edge City Press, Reston, VA, 1995.

[10] LISA Pre-Phase A Report, JPL Tech. Report # MPQ 233, July 1998.

[11] Khayms, V., and Martinez-Sanchez, M., "Preliminary Experimental Evaluation of a Mineatureized Hall Thruster," IEPC 97-077, 25th International Electric Propulsion Conference, Aug. 24-28, 1997, Cleveland, OH.

[12] Personal communications, M. T. Domonkos, Nov. 1998.

[13] Blandino, J. J., and Cassady, R. J., "Propulsion Requirements and Options for the New Millennium Interferometer (DS-3) Mission," 34th AIAA/ASME/SAE/ASEE Joint Propulsion Conference, July 13-15, 1998, Cleveland, OH.

[14] Hoyt, R. P., "Tether System for Exchanging Payloads between LEO and the Lunar Surface," AIAA 97-2794, 33rd AIAA/ASME/SAE/ASEE Joint Propulsion Conference, July 1997, Lake Beuna Vista, FL.

[15] Oldson, J., and Carrol, J. A., "Potential Launch costs Savings of a Tether Transport Facility," AIAA 95-2895, 31st AIAA/ASME/SAE/ASEE Joint Propulsion Conference, July 1995, San Diego, CA.

[16] Sanmartin, J. R., Martinez-Sanchez, M., and Ahedo, E., "Bare Wire Anodes for Electrodynamic Tethers," J. Propulsion and Power 9(3), May-June 1993.

[17] Hoyt, R. P., and Forward, R., "The Terminator Tether De-orbit System," Proc. 9th Advanced Space Propulsion Workshop at JPL, March 11-13, 1998.

[18] Spindt, C. A., Holland, C. E. , Rosengreen, A., and Brodie, I., "Field-Emitter Arrays for Vacuum Microelectronics," IEEE Transactions on Electron Devices 38(10), Oct. 1991.

[19] Gomer, R., *Field Emission and Field Ionization*, Harvard University Press, Cambridge, Massachusetts, 1961.

[20] Modinos, A., *Field, Thermionic, and Seconday Electron Spectroscopy*, Plenum, New York, 1984.

[21] Jensen, K. L, "Field Emitter Arrays for Plasma and Microwave Source Applications," Physics of Plasmas **6**, 1999.

[22] Brodie, I., and Schwoebel, P., "Vacuum Microelectronics Devices," Proc. IEEE, 83(7), July 1994.

[23] Spindt, C. A., Holland, C. E., Schwoebel, P. R., and Brodie, I., "Field Emitter Array Development for Microwave Applications II," J. Vac. Sci. Technol. B 16(2), Mar/Apr 1998.

[24] Bozler, C. O., Harris, C. T., Rabe, S., Ratham, D. D., Hollis, M., and Smith, H. I., "Arrays of Gated Field-emitter Cones Having 0.32 μm Tip-to-Tip Spacing," J. Vac. Sci. Technol. B 12(2), 1994.

[25] Mackie, W. A., Xie, T., and Davis, P. R., "Field Emission from Carbide Thin Film Cathodes," J. Vac. Sci. and Technol. B 13(6), Nov/Dec 1995.

[26] Charbonnier, F., "Arcing and Voltage Breakdown in Vacuum Microelectronics Microwave Devices Using Field Emitter Arrays: Causes, Possible Solutions, and Recent Progress," J. Vac. Sci. Technol. B 16(2), Mar/Apr 1998.

[27] Rakhshandehroo, M. R., "Design, Fabrication, and Characterization of Self-aligned Gated Field Emission Devices," Dissertation for Ph.D at The University of Michigan, Tech. rep. no. SSEL-284, 1998.

[28] Tolt, Z. Li., Fink, R. L., and Yaniv, Z., "The Status and Future of Diamond Thin Film FED," Nikkei Microdevices' Flat Panel Display 1998 Yearbook, English translation published by InterLingua, 186, 1998.

[29] Spindt, C. A., Holland, C. E., Schwoebel, P. R., and Brodie, I., "Field Emitter Array Development for Microwave Applications," J. Vac. Sci. Technol. B 14(3), May/June 1996.

[30] Murphy, R. A., Harris, C. T., Matthews, R. H., Graves, C. A., Hollis, M. A., Kodis, M. A., Shaw, J., Garven, M., Ngo, M. T., and Jensen, K. L., IEEE International Conference on Plasma Science, San Diego, CA, May 19-22, 1997.

[31] Spindt, C. A., and Brodie, I., Technical Digest of the 1996 IEEE International Electron Devices Meeting (IEDM), 12.1.1 (1996); C. A. Spindt, C. E. Holland, P. R. Schwoebel, and I. Brodie, IEEE International Conference on Plasma Science, San Diego, CA, May 19-22, 1997.

[32] Schwoebel, P. R., and Spindt, C. A., "Field-Emitter Array Performance Enhancement Using Hydrogen Glow Discharges," Appl. Phys. Lett. 63(1), 5 July 1993.

[33] Schwoebel, P. R., and Spindt C. A., "Glow Discharge Processing to Enhance Field-Emitter Array Performance," J. Vac. Sci. Technol. B 12(4), Jul/Aug 1994.

[34] Rakhshandehroo, M. R., and Pang, S. W., "Sharpening Si Field Emitter Tips by Dry Etching and Low Temperature Plasma Oxidation," J. Vac. Sci. Technol. B 14(6), Nov/Dec 1996.

[35] Personnal communications, C. A. Spindt, Nov. 1998.

[36] Geiss, M. W., Twichell, J. C., and Lyszarz, T. M., "Diamond Emitters Fabrication and Theory," J. Vac. Sci. Tech. B 14(3), May/June 1996.

[37] Tolt, Z. L., Fink, R. L., and Yaniv, Z., "Electron Emission from Patterned Diamond Flat Cathodes," Tech. Digest International Vacuum Microelectronics Conference (IVMC), 1997, Korea.

[38] Fink, R. L., Thuesen, L. H., Tolt, Z. Li., and Yaniv, Z., "Lifetime and Stability of Diamond Field Emission Devices," Proceedings of the 2nd International Symposium on Diamond Electron Devices, March, 1998, Osaka, Japan, accepted for pubilication.

[39] Blyablin, A. A., Kandidov, A. V., Pilevskii, A. A., Rakhimov, A. T., Samorodov, V. A., Seleznev, B. V., Suetin, N.V., and Timofeev, M. A., "The Study of Electron Source with Flat Diamond Field Emission Cathode," Tech. Digest International Vacuum Microelectronics Conference (IVMC), 1998, Asheville, NC.

[40] Itoh, S., Niiyama, T., Taniguchi, M., and Watanbe, T., "A New Structure of Field Emitter Arrays," J. Vac. Sci. Technol. B 14(3), May/June 1996.

[41] Grossman, K., and Peckerar, M., "Active Current Limitation for Cold-Cathode Field Emitters," Nanotechnology **5**, 1994.

[42] Takemura, H., Tomihari, Y., Furutake, N., Matsuno, F., Yoshiki, M., Takada, N., Okamoto, A., and Miyano, S., "A Novel Vertical Current Limiter Fabricated with a Deep Trench Forming Technology for Highly Reliable Field Emitter Arrays," Tech. Digest IEEE-IEDM, 709, 1997.

[43] Lindberg, P. A. P., and Johansson, L. I., "Work Function and Reactivity of Some Crystal Faces of Substoichimetric Transition-Metal Carbides," Surface Sci., 194, 1988.

[44] Mackie, W. A., Xie, T., and Davis, P. R., "Field Emission from Carbide Film Cathodes," J. Vac. Sci. Technol. B 13(6), Nov/Dec 1995.

[45] Ishikawa, J., Tsuji, H., Yashuto, Sasaki, T., Kaneko, T., Nagao, M., and Inoue, K., "Influence of Cathode Material on Emission Characteristics of Field Emitters for Microelectronics Devices," J. Vac. Sci. Technol. B 11(2), Mar/Apr 1993.

[46] Palmer, W. D., Temple, D., Mancusi, J., Yadon, L., Vellenga, D., and McGuire, G. E., "Emission Current Measurements Under Flat Panel Display Conditions," 25th IEEE International Conference on Plasma Science, June 1998, Raleigh, NC.

[47] Temple, D., Palmer, W. D., Yadon, L. N., Mancusi, J. E., Vellenga, D., and McGuire, G. E., "Silicon Field Emitter Cathodes: Fabrication, Performance, and Applications," J. Vac. Sci. Tech. A 16(3), May/June 1998.

[48] Brodie, I., "Bombardment of Field-Emission Cathodes by Positive Ions Formed in the interelectrode Region," Int. J. Electronics 38(4), 1975.

[49] Langmuir, I., Physical Review 2, 450, 1913.

[50] Childs, C., Physical Review 32, 492, 1911.

[51] Fay , C. E., Samuel, A. L., and Shockley, W., "On the Theory of Space Charge Between Parallel Plane Electrodes," Bell System Technical Journal 17(9), 1938.

[52] Langmuir, I., "The Interaction of Electron and Positive Ion Space Charges in Cathode Sheaths," Phys. Rev. 33, June 1929.

[53] Bohm, D., *Characteristics of Electrical Discharges in Magnetic Fields*, ed. A. Guthrie and R. K. Wakerling, McGraw-Hill Book Co., Inc. 1949.

[54] Crawford, F. W., and Cannera, A. B., "Structure of the Double Sheath in a Hot Cathode Plasma," J. Appl. Phys. 36(10), Oct. 1965.

[55] Prewett, P. D., and , Allen, J. E. , "The Double Sheath Associated with a Hot Cathode," Proc. R. Soc. Lond. A. 348, 1976.

[56] Andrews, J. G., and Allen, J. E., "Theory of a Double Sheath Between Two Plasmas," Proc. Roy. Soc. Lond. A. 320, 1971.

[57] Goodfellow, K. D., "A Theoretical and Experimental Investigation of Cathode Processes in Electric Thrusters," Ph.D. dissertation USC 1996.

[58] Domonkos, M. T., Marrese, C. M., Haas, J. M., and Gallimore, A. D., "Very Near-Field Plume Investigation of the D-55 Anode Layer Thruster," AIAA-97-3062 33st. AIAA/ASME/SAE/ASEE Joint Propulsion Conference, Seattle, WA, July 1997.

[59] Haag, T. W., and Curran, F. M., "Arcjet Starting Reliability: A Multistart Test on Hydrogen/Nitrogen Mixtures," AIAA-87-1061, (NASA TM-898867), May 1987.

[60] King, L. B., and Gallimore, A. D., "Gridded Retarding Pressure Sensor for Ion and Neutral Particle Analysis in Flowing Plasmas," Rev. Sci. Instrum. 68(2), Feb. 1997.

[61] Mackie, W. A., and Hindrichs, C. H., "Preparation of ZrC_x Single Crystal by an Arc Melting Floating Zone Technique," J. Crystal Growth 87, 1988.

[62] Xie, T., Mackie, W. A., and Davis, P. R., "Field Emission from ZrC Films on Si and Mo Single Emitters and Emitter Arrays," J. Vac. Sci. Technol. B 14(3), May/Jun 1996.

[63] Mackie, W. A., Morrissey, J. L., Hinrichs, C. H., and P. R. Davis, "Field Emission from Hafnium Carbide," J.Vac. Sci. Technol. A 10(4), Jul/Aug 1992.

[64] Mackie, W. A., Hartman, R. L., Anderson, M. A., and Davis, P. R., "Transition Metal Carbides for Use as Field Emission Cathodes," J. Vac. Sci. Technol. B 12(2), Mar/Apr 1994.

[65] Mackie, W. A., Xie, T., and Davis, P. R., "Field Emission from Carbide Film Cathodes," J. Vac. Sci. Technol. B 13(6), Nov/Dec 1995.

[66] Temple, D., Palmer, W. D., Yadon, L. N., Mancusi, J. E., Vellenga, D., and McGuire, G. E., "Silicon Field Emitter Cathodes: Fabrication, Performance, and Applications," J. Vac. Sci. Technol. A 16(3), May/June 1998.

[67] Yamamura, Y., Matsunami, N., and Itoh, N., "Theoretical Studies on an Empirical Formula for Sputtering Yield at Normal Incidence," Radiat. Eff. 71, 1983.

[68] Urayama, M., Ise, T., Maruo, Y., Kishi, A., Imamoto, R., and Takase, T., "Silicon Field Emitter Capable of Low Voltage Emission," Jpn. J. Appl. Phys. 32 Pt. 1, No. 12B, 1993.

[69] Jensen, K. L., "An Analytical Model of an Emission-gated Twystrode Using a Field Emission Array," J. Appl. Phys. 83(12), June 1998.

[70] Charbonnier, F., "Arcing and Voltage Breakdown in Vacuum Microelectronics Microwave Devices Using Field Emitter Arrays: Causes, Possible Solutions, and Recent Progress," J. Vac. Sci. Technol. B 16(2), Mar/Apr 1998.

[71] Jensen, K.L., Mukhopadhyay, P., Zaidman, E.G., Nguyen, K., Kodis, M.A., Malsawma, L., and Hor, C., "Electron Emission from a Single Spindt-Type Field Emitter: Comparison of Theory with Experiment," Appl. Surf. Sci. 111, 1997.

[72] Brodie, I., "Bombardment of Field-Emission Cathodes by Positive Ions Formed on the Interelectrode Region," Int. J. Electronics, 38(4), 1975.

[73] Everhart, T. E., "Simplified Analysis of Point-Cathode Electron Sources," J. Appl. Phys. 38(113), 1967.

[74] Brown, S., *Basic Data of Plasma Physics*, M.I.T. Press 1966.

[75] Matsunami, N., Yamamura, Y., Itikawa, Y., Itoh, N., Kazmuta, Y., Miyagawa, S., Morita, K., Shimizu, R., Tawara, H., "Energy Dependance of the Ion-Induced Sputtering Yields of Monatomic Solids," Atomic Data and Nuclear Data Tables 31, 1984.

[76] Bohdansky, J., Roth, J., and Bay, H. L., "An Analytical Formula and Important Parameters for Low-Energy Ion Sputtering," J. Appl. Phys. 51(5), May 1980.

[77] Stuart, R. V. and Wehner, G. K., "Sputtering Yields at Low Bombarding Ion Energies," J. Appl. Phys. 33(7), July 1962.

[78] Rosenberg, D., and Wehner, G. K., "Sputtering Yields for Low Energy He^+-, Kr^+-, and Xe^+-Ion Bombardment," J. Appl. Phys. 33(5), 1962.

[79] Jensen, K. L, Kodis, M. A., Murphy, R. A., Zaidman, E. G., "Space-Charge Effects on the Current-Voltage Characteristics of Gated Field Emitter Arrays," J. Appl. Phys. 82(2), July 1997.

[80] True, R. B., Good, G. R., Hargreaves, T. A., Palmer, W. D., "Analysis of Isotropic and Anisotropic Etch Field Emitter Array Cathodes," IEEE International Conference on Plasma Science, 1997.

[81] Mackie, W. A, Morrissey, J. L., Hinrichs. C.H., Davis, P.R., "Field Emission from Hafnium Carbide," J. Vac. Sci. Technol. A 10(4), Jul/Aug 1992.

[82] Mackie, W. A., Hartman, R. L., Anderson, M. A., Davis, P. R., "Transition Metal Carbides for Use as Field Emission Cathodes," J. Vac. Sci. Technol

[83] Domonkos, M. T., Marrese, C. M., Haas, J. M., and Gallimore, A. D., "Very Near-Field Plume Investigation of the D-55 Anode Layer Thruster," AIAA-97-3062 Joint Propulsion Conference, July 1997, Seattle, WA.

[84] Hutchensen, I. H., *Principles of Plasma Diagnostics*, Cambridge University Press, 1987.

[85] Neubert, T., Mandell, M. J., Sasaki, S., Gilchrist, B. E. , Banks, P., Williamson, P. R., Raitt, W. J., Meyers, N. B., Oyama, K. I., and Katz, I., "The Sheath Structure Around a Negatively Charged Rocket Payload," J. Geophysical Research 95(A5), May 1, 1990.

[86] Personal communications, J. Wang, June 1999.

[87] Wang, J., and Lai, S. T., "Virtual Anode in Ion Beam Emission in Space: Numerical Simulations," J. Spacecraft and Rockets 34(6), Nov.-Dec. 1997.

[88] Grard, R., Gonfalone, A., and Pedersen, A., "Spacecraft Potential Control with Electron Emitters," Presented as Paper SM-127F at the Spring Annual Meeting of the American Geophysical Union, June 16-19, 1975, Washington, D.C.

[89] Lee, Hsien-Chung, and Huang, Ruey-Shing, "A Study on Field Emission Array Pressure Sensors," Sensors and Actuators A, 34, 1992.